LONG-TERM VARIATIONS IN THE HIGH-LATITUDE PLASMA FLOWS INFERRED FROM SUPERDARN RADAR DATA

A Thesis Submitted to the
College of Graduate Studies and Research
in Partial Fulfillment of the Requirements
for the Degree of Master of Science
in the Department of Physics and Engineering Physics
University of Saskatchewan
Saskatoon

By
Zahra Abooalizadeh

PERMISSION TO USE

In presenting this Thesis in partial fulfillment of the requirements for a Postgraduate degree from the University of Saskatchewan, I agree that the Libraries of this University may make it freely available for inspection. I further agree that permission for copying of this Thesis in any manner, in whole or in part, for scholarly purposes may be granted by the professor or professors who supervised my thesis work or, in their absence, by the Head of the Department or the Dean of the College in which my Thesis work was done. It is understood that any copying or publication or use of this Thesis or parts thereof for financial gain shall not be allowed without my written permission. It is also understood that due recognition shall be given to me and to the University of Saskatchewan in any scholarly use which may be made of any material in my Thesis.

Requests for permission to copy or to make other use of material in this thesis in whole or part should be addressed to:

Head of the Department of Physics and Engineering Physics
Physics Building
116 Science Place
University of Saskatchewan
Saskatoon, SK S7N 5E2
Canada

ABSTRACT

This Thesis investigates ionospheric plasma flows (commonly referred to as "convection") at high latitudes with the objectives to assess seasonal and solar cycle variations in the shape of the flow patterns and the flow intensity in terms of external drivers of the flow, first of all the magnitude and orientation of the interplanetary magnetic field (IMF). Multi-year (2001-1011) line-of-sight Doppler velocity data collected by the Super Dual Auroral Network (SuperDARN) HF radars are considered. Two approaches are used: 1) analysis of monthly-averaged 2-dimentional patterns inferred from data of all SuperDARN radars operated and 2) analysis of near magnetic noon data from only two SuperDARN radars, Rankin Inlet and Inuvik monitoring meridional component of the flow in the near North Pole areas (polar cap). We show and discuss seasonal and solar cycle variations of three characteristics of the flows: magnetic latitudes of the region where plasma flow direction changes from toward the noon to away from the noon (convection reversal boundary), the magnetic local time location of the near noon region with stagnated flow (throat region) and, finally, the magnitude of the flow. All three parameters show trends, although not strong and consistent all the time, which agrees with previous publications where different analysis approaches and more limited data sets were used. For two specific points, one at the magnetic latitude of 72 degrees, representing the auroral oval latitudes (region where optical arcs occur most frequently) and the other one at 82 degrees, representing the polar cap latitudes we demonstrate that the average flow magnitude increases with the IMF intensity, and the effect is much stronger for the negative vertical component of the IMF B_z. In our second approach we demonstrate that the flow velocity increases almost linearly with an increase of the reconnection electric fields characterizing processes of interaction between the solar wind/IMF and the Earth`s magnetic dipole. Saturation effect is seen for strongest electric field. More clear seasonal effects are noticeable in these data; the velocity response to the reconnection electric field enhancement is stronger summer (winter) time for positive (negative) IMF B_z. The data are consistent with previous reports, where highly smoothed velocity data were considered.

ACKNOWLEDGEMENTS

I would like to thank my supervisor Dr. Alexander Koustov for his guidance, help and patience with me throughout my Master's program. I am very grateful for the opportunity he has given to me to study under his supervision.

I would also like to thank Dr. Robyn Fiori for preprocessing all the data for this project.

I would also like to thank all the members in the institute of Space and Atmospheric Studies (ISAS) at the University of Saskatchewan.

TABLE OF CONTENTS

LIST OF FIGURE CAPTIONS

LIST OF ABBREVIATIONS

ACF	Autocorrelation Function
ACE	Advanced Composition Explorer
AMISR	Advance Modular Incoherent Scatter Radar
CADI	Canadian Advanced Digital Ionosonde
CLY	Clyde River
CPCP	Cross Polar Cap Potential
CRB	Convection Reversal Boundary
CUTLASS	Co-ordinated UK Twin-Located Auroral Sounding System
DMSP	Defense Meteorological Satellite Program
FACs	Field Aligned Currents
FAI	Field Aligned Irregularities
FoV	Filed of View
GS	Ground Scatter
GSM	Geocentric Solar Magnetospheric
HF	High Frequency
HM	Heppner Maynard
IEF	Interplanetary Electric Field
IMAGE	Image for Magnetopouse-to-Aurora Global Exploration
IMF	Interplanetary Magnetic Field
INV	Inuvik
ISR	Incoherent Scatter Radar
LOS	Line of Sight
MHD	Magnetohydrodynamic
MLAT	Magnetic Latitude
MLT	Magnetic Local Time
PCN	Polar Cap North
PolarRDARN	Polar Dual Auroral Radar Network
RB	Resolute Bay
RG96	Ruohoniemi and Greenwald 1996 convection model
RKN	Rankin Inlet
SCHA	Spherical Cap Harmonic Analysis
SN	Sunspot Number
Super DARN	Super Dual Auroral Radar Network
SYM-H	Magnetic index characterizing storm occurrence
SW	Solar Wind
UT	Universal Time

CHAPTER 1

INTRODUCTION

1.1 The solar wind and the Earth's magnetosphere

The Sun is continuously ejecting plasma, known as the solar wind (SW). The SW plasma consists of mostly electrons and positively charged ions of hydrogen. It is electrically quasi-neutral. The SW expands with increasing speed and reaches the Earth's location where it interacts with its magnetic dipole field forming a special cavity, called the magnetosphere. The interaction is facilitated by the process of slowing down of the incoming flow in the bow shock. Figure 1.1 shows approximate location, size and shape of the bow shock and the magnetosphere. The outer boundary of the magnetosphere, the magnetopause, is a special region in space; it bounds that part of space where particle dynamics is mostly controlled by the magnetic field rather than by pressure from the SW flow in the plasmasheath, Figure 1.1.

The solar wind carries with it not only particles but also the Sun's magnetic field, which is traditionally referred to as the Interplanetary Magnetic Field (IMF). The Sun's magnetic field near the Earth's orbit is weak; typical magnitudes are ~1-5 nT. Motion of the IMF flux lines together with the SW fluid implies existence of the interplanetary electric field (IEF) found from the relation

$$\vec{E} = -\vec{V}_{SW} \times \vec{B}, \tag{1.1}$$

where $\vec{V}_{SW}$ is the fluid velocity of the SW (Hargreaves, 1992).

The magnetopause (magnetic field lines) is stretched in the anti-sunward direction behind the Earth, forming the magnetotail, and somewhat compressed (as compared to the simple magnetic dipole configuration) in the sunward direction. The magnetosphere has a complex and dynamic structure because of a number of processes occurring here involving particle population redistribution under the influence of the continuously varying magnetic and electric fields. The fields act on both electrons and ions in the magnetosphere forcing them to move in bulk.

Figure 1.1 also shows a fundamentally important magnetospheric region, the plasma sheet, where the process of plasma motion towards the Earth begins ending up with some particles being accelerated and injected into the upper atmosphere. These particles produce beautiful northern

lights. It is important to realize that some magnetic flux lines at the near Pole regions may extend far away from the Earth and, for this reason, they are commonly referred to as the open flux lines. On the dayside, there are special regions of the Earth's magnetic dipole, the funnel-like cusps, where the magnetic flux lines are open and the solar wind plasma can penetrate into the upper atmosphere directly. The majority of particle inflow into the upper atmosphere, however, occurs through the processes in the magnetotail/plasma sheet, Figure 1.1. The plot also introduces the Geocentric Solar Magnetospheric (GSM) coordinate system, the traditionally used coordinate system, with X axis directed towards the Sun and Y axis oriented perpendicular to the Earth's dipole. The Z axis is chosen to be positive toward the northern magnetic pole.

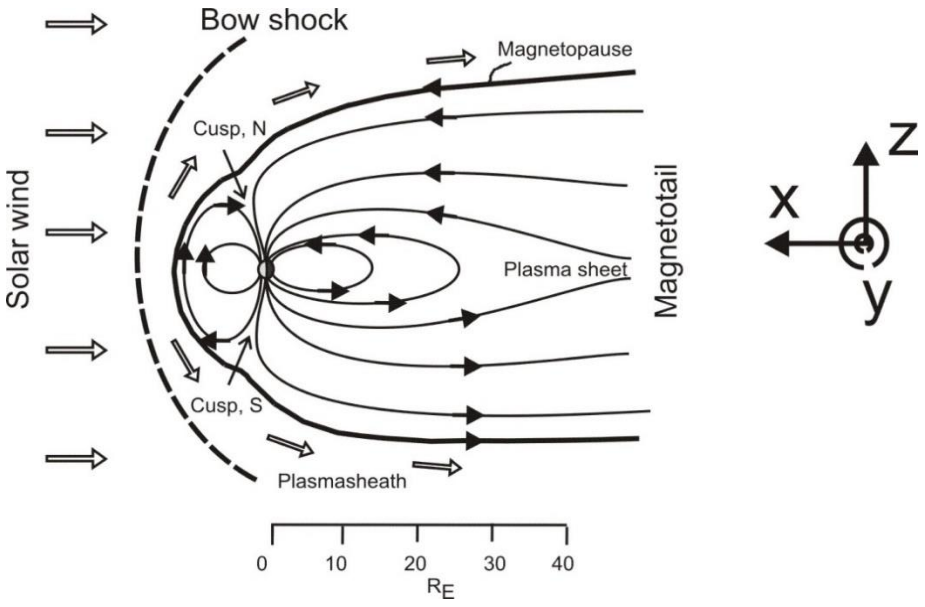

Figure 1.1: Major elements of the Earth's magnetosphere in the North-South plane. On the right, unit vectors of a widely used coordinate system (Geocentric Solar Magnetospheric, GSM) are shown.

Interaction between various magnetospheric regions is affected by a conducting layer of the upper atmosphere, called the ionosphere. The ionosphere is that part of the Earth's atmosphere where significant amount of charged particles, produced by the solar radiation and precipitating from the magnetosphere particles, coexist with neutrals so that the plasma is partially ionized. The ionosphere can be considered as a transition region between the fully ionized plasma in the magnetosphere and electrically neutral low-altitude atmosphere (Hargreaves, 1992).

1.2 The Earth's ionosphere and plasma motion in the ionosphere

The Earth's ionosphere extends from the altitude of about 90 km to 600-1000 km. It consists of three main layers based on the electron density distribution with altitude. Figure 1.2 gives an example of the electron density distribution in the ionosphere with three identifiable layers known as the D, E and F regions. The D region is the lowest region at altitudes from 70 to 95 km above the ground with the maximum electron density of ~10^4 cm^{-3}. The ionization at these heights happens due to solar radiation and, to less extent and at high latitudes only, particle precipitation from the magnetosphere. At night time, because there is no photoionization at these altitudes, the D region vanishes.

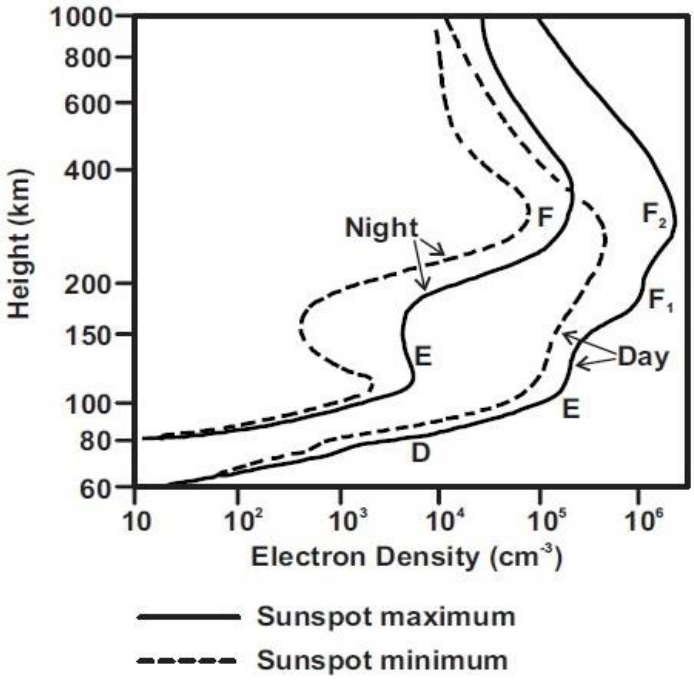

Figure 1.2: Typical electron density profiles in the ionosphere during day and night at the solar cycle maximum and minimum (Adapted from Hargreaves, 1992).

The E region is the middle region at altitudes from 95 to 150 km. The typical electron density here is about 10^5 cm^{-3}. The ion population in the E region consists of NO^+ and O_2^+ resulting from photoionization of N_2 and O_2 molecules. At night, the lack of photons leads to reduction of

electron-ion pair production, and recombination of ions and electrons leads to E region disappearance.

The F region is at the altitudes from 150 to ~600 km. Typical electron densities here are up to 10^6 cm^{-3} at the peak which occurs at altitude of ~270 km during night. During daylight, there are two peaks at 170 km (F1 layer) and at 300 km (F2 layer). In the F region there are ions such as NO^+, O_2^+ and O^+. Photoionization at the F region heights decreases at night as well, but the F region only weakens, in contrast to the D and E regions (Kivelson and Russell, 1995).

Plasma in the Earth's ionosphere is in constant motion. This happens for several reasons, but at high latitudes, the prime area of interest in this Thesis, the main factor is the electric field of the magnetospheric origin and the Earth's magnetic field. To estimate the velocity of the electron and ion motions in the ionosphere, the magnetic field is approximated by straight lines. The equations for particle motion (their guiding centers) are often considered in a simplified form

$$m_\alpha \frac{d\vec{V}_\alpha}{dt} = q_\alpha\left[\vec{E} + \vec{V}_\alpha \times \vec{B}\right] - m_\alpha \nu_\alpha \vec{V}_\alpha - \frac{\nabla(n_\alpha T_\alpha)}{n_\alpha}, \tag{1.2}$$

where the subscript α stands for *i* and *e* (indicating ions and electrons, respectively), $\vec{V}_\alpha$ is the plasma velocity, q_α is the particle charge, m_α is the particle mass, ν_α is the ion or electron collision frequency with neutral particles, T_α is the temperature, and *n* is the particle density (Kelley, 1989). Furthermore, one can consider cold plasma approximation of $T_{i,e} = 0$ eV as the thermal-related motions are slow in the ionosphere. Equation (1.2) becomes

$$m_\alpha \frac{d\vec{V}_\alpha}{dt} = q_\alpha\left[\vec{E} + \vec{V}_\alpha \times \vec{B}\right] - m_\alpha \nu_\alpha \vec{V}_\alpha. \tag{1.3}$$

For stationary state ($d/dt = 0$), the particles velocity $\vec{V}_\alpha$ can be expressed as

$$\vec{V}_\alpha = \frac{\Omega_\alpha \nu_\alpha}{\Omega_\alpha^2 + \nu_\alpha^2}\frac{\vec{E}}{\vec{B}} + \frac{\Omega_\alpha^2}{\Omega_\alpha^2 + \nu_\alpha^2}\frac{\vec{E} \times \vec{B}}{\left|\vec{B}\right|^2}, \tag{1.4}$$

where $\Omega_\alpha = q_\alpha\left|\vec{B}\right|/m_\alpha$ is the ion or electron gyrofrequency, and $\vec{E}$ is the electric field component perpendicular to the magnetic field $\vec{B}$. Equation (1.4) indicates that the velocity of particle motion is different along the electric field direction (Pedersen drift) and in the $\vec{E} \times \vec{B}$ drift direction (Hall drift). In the ionospheric top regions, collision frequencies for both electrons and ions are small,$\nu_\alpha \to 0$, and both species experience Hall drift with the velocity

$$\vec{V}_{E\times B} = \frac{\vec{E}\times\vec{B}}{\left|\vec{B}\right|^2}. \quad (1.5)$$

This common motion is often referred to as plasma "convection" or $\vec{E}\times\vec{B}$ drift. Collisionless plasma in the magnetosphere experiences convection or $\vec{E}\times\vec{B}$ drift as well.

In most of the F region, collisions are not frequent ($\nu_\alpha \ll \Omega_\alpha$) and expression (1.5) characterizes well the plasma motion as a whole, i.e. collisions are not affecting the plasma motion. However, collisions are not negligible when some processes are considered, for example plasma instability leading to formation of microstructures of the electron density. Equation (1.4) implies that the velocity of electrons and ions along the E field direction are slightly different. Indeed, since in the F region $\nu_i/\Omega_i \gg \nu_e/\Omega_e$ one gets from (1.4)

$$V_e\left(\text{along }\vec{E}\right) = \frac{\nu_e}{\Omega_e}\frac{E}{|B|};\quad V_i\left(\text{along }\vec{E}\right) = \frac{\nu_i}{\Omega_i}\frac{E}{|B|};\quad \frac{\left|\vec{V}_i\right|}{\left|\vec{V}_e\right|}\left(\text{along }\vec{E}\right) = \frac{\nu_i}{\Omega_i}\frac{\Omega_e}{\nu_e} \approx 100. \quad (1.6)$$

Thus, at the F region heights, there is a small relative drift between electrons and ions in the direction of the electric field (relative Pedersen drift) (Kelley, 1989). This effect will be referred to in Chapter 2.

Collisions are more important in the E region where ions become unmagnetized in a sense that their dynamics is not dependent on the magnetic and electric fields presence and dominated by collisions with neutrals. To a first approximation, one can consider them as not moving at all since neutrals move very slowly (speeds <50-100 m/s). Since electrons are still controlled by the electric and magnetic field at these heights, experiencing the $\vec{E}\times\vec{B}$ Hall drift, a strong relative drift between electrons and ions occurs resulting in the electric current flowing perpendicular to the magnetic field. This current, known as the auroral electrojet, is routinely sensed with magnetometers on the ground and in space (Kivelson and Russell, 1995). Such measurements allow space physicists to study various processes in the ionosphere and magnetosphere.

1.3 Magnetic reconnection and plasma circulation within the magnetosphere

It has been realized that plasma motions in the magnetosphere and ionosphere are synchronized through a common factor; electric field oriented perpendicular to the Earth's magnetic field. The field can "map" along the magnetic field lines from the magnetosphere to the

ionosphere with some amplification factor. Because plasma motions seen in the ionosphere reflect plasma motions in the magnetosphere, understanding of the ionospheric flows is key to undrestanding Sun-Earth connections. Here are several aspects of the problem that are relevant to the plasma convection phenomenon.

The most important processes of interaction between the IMF and the Earth's magnetic field are merging and reconnection of the magnetic field lines (Dungey, 1961), resulting in a special configuration of plasma circulation in the ionosphere. These processes dominate when the IMF is oriented in opposite direction with respect to the Earth's magnetic dipole.

Figure 1.3 explains the magnetic merging/reconnection process. When a southward IMF (notations to be used: B_z<0 or B_z^-) flux line approaches a closed northward geomagnetic field line at the magnetospheric front side, they merge and form two new "open" field lines, in the northern and southern hemispheres, Figure 1.3, lines 2 and $2^{/}$. These new field lines are carried downstream by the solar wind, for example lines 3 and $3^{/}$. Strongly stretched magnetic flux lines experience magnetic pressure in the direction toward the magnetotail plasma sheet, lines 4 and $4^{/}$. Eventually, the open magnetic field lines in the northern and southern parts of the magnetotail (lines 5 and $5^{/}$) reconnect, forming a new closed field lines (6 and $6^{/}$) that are pushed toward the Earth by magnetic pressure in the magnetotail, and "open" lines continue travelling into outer space. This continuously ongoing process is called the reconnection cycle. As the footprints of magnetic flux tubes, driven by the solar wind, cross the high latitudes, the plasma is driven in the anti-sunward direction over the North Pole area, as shown Figure 1.3, bottom diagram. The flows are then returned back toward the Sun at lower latitudes forming the morning and evening convection cells. In this way, the so called two-cell convection pattern is formed. The dusk and dawn cells are roughly symmetric with respect to the noon-midnight meridian when the IMF B_y is small. For strong positive (negative) B_y, the dusk (dawn) cell dominates in the northern hemisphere and opposite happens in the southern hemisphere.

One can understand what happens at the ionospheric level during the reconnection cycle under the IMF B_z<0 condition in a different way; one can take into consideration the fact that the solar wind carries electric field oriented in the dawn to dusk direction. While mapped down into the ionosphere via field-aligned currents (FACs), this electric field gives $\vec{E} \times \vec{B}$ motion of the plasma in the central polar cap in anti-sunward direction, Figure 1.3, bottom diagram. The polar

cap electric field has the strength of 20-30 mV/m and the corresponding cross polar cap potential (CPCP) is ~ 50 kV on average (Kivelson and Russell, 1995).

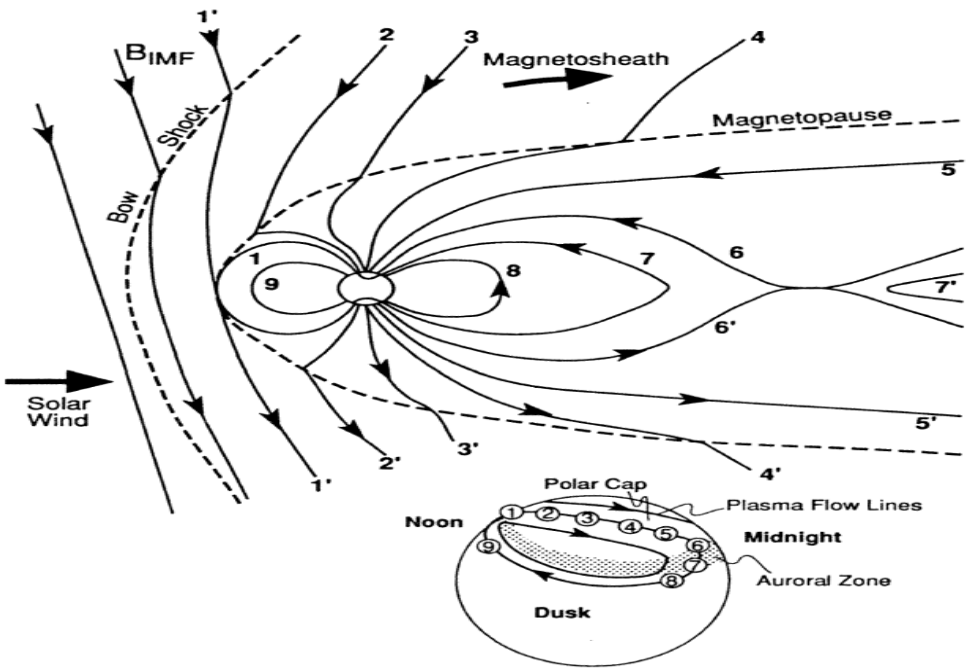

Figure 1.3: A scheme illustrating reconfiguration of magnetic field lines as the southward IMF passes the near-Earth environment, top diagram, and motion of the magnetic flux tubes projected onto the ionosphere, bottom diagram, (Adapted from Kivelson and Russel, 1995).

In a case of the northward IMF (notations to be used: $B_z>0$ or B_z^+), the merging/reconnection process can also occur but on the lobe magnetic field lines (e.g., Crooker and Rich, 1993). Example of lines involved in lobe reconnection are given in Figure 1.4a. These processes are added to the so-called quasi-viscous interaction between the SW and magnetosphere which is associated with "friction" of the magnetic flux tubes with the boundary of the magnetosphere, the magnetopause, as suggested by Axford and Hines (1961), Figure 1.4b. Quasi-viscous interaction implies that the magnetosphere is closed, as shown. Exact physics of energy and momentum transfer during these processes has not been established. Importantly, the quasi-viscous interaction also produces two-cell convection pattern with antisunward flows over the North Pole. The combination of the lobe merging and quasi-viscous interaction for $B_z>0$ leads to a complex structure of the plasma circulation on the dayside, often consisting of several cells. In a case of strong northward IMF B_z, a four cell convection pattern dominates (Heelis et al., 1986).

However, when the IMF B_y is not small, observations show rather two cells although they are strongly distorted (Heppner and Maynard, 1987).

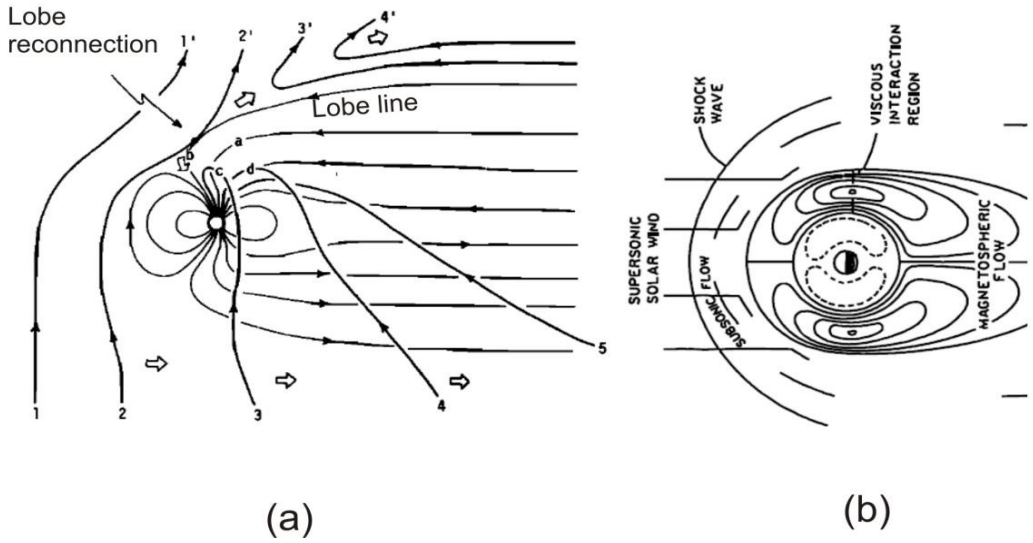

Figure 1.4: Cartoons illustrating interactions of the solar wind magnetic field lines as the northward IMF passes the near-Earth environment: (a) lobe reconnection (from Maezawa, 1976) and (b) magnetic field lines dragging along the magnetopause which produces quasi-viscous friction (from Kelley, 1989).

Examples of the ionospheric convection patterns are given in Figure 1.5. Here the approximate location of the auroral oval, where strong optical forms are most frequently occur, are shown by dark belts and contours of equal electric potential are depicted. The plasma flows along these contours. Differences between the patterns in Figures 1.5a and 1.5b are obvious. For B_z<0, there is a two-cell convection pattern with both cells being "round" and of about the same shape. One can think of the pattern is primarily driven by the dawn-to-dusk electric field shown by the red arrow in Figure 1.5a. Two regions of these patterns are widely discussed in literature, the throat region on the dayside and the convection reversal boundary (CRB), the line where the plasma reverses its motion from sunward at low latitudes to anti-sunward at high latitudes. (Rich and Hairston, 1994) The CRB is shown by the pink line in Figure 1.5a and only for the dusk sector. Generally, it is more obvious during dawn and dusk hours.

For B_z>0, two additional cells are seen in Figure 1.5b. The large-scale cells, originating from quasi-viscous interaction are "crescent-like"; they are squeezed to lower latitudes. The

"round" small cells are seen on the dayside. The flow here is in opposite direction as compared to the large-scale cells.

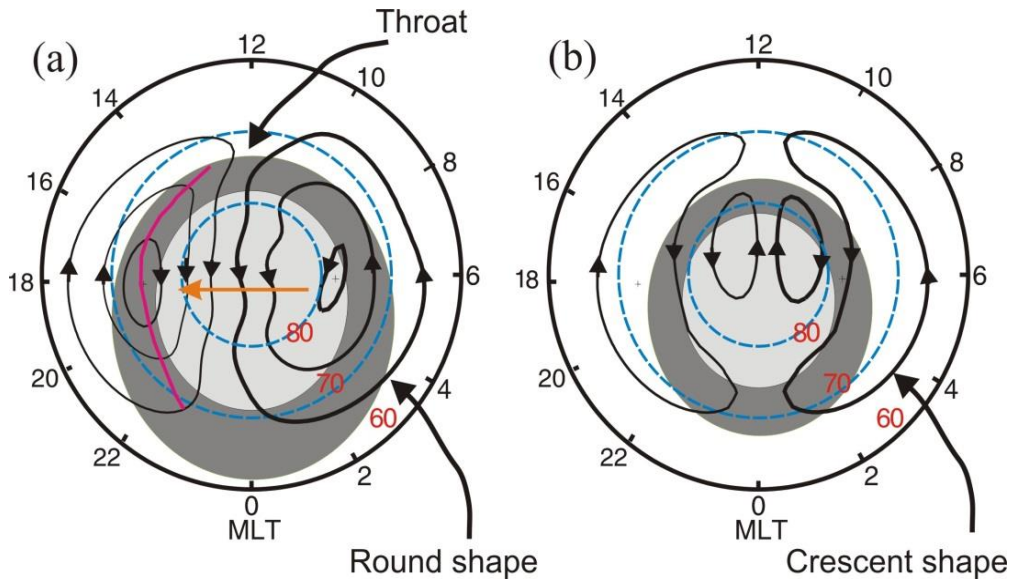

Figure 1.5: Examples of (a) two-cell convection pattern for IMF B_z<0, (b) four-cells convection pattern for IMF B_z>0. Darker belt is the auroral oval of most-frequent occurrence of aurora. Grey area is the polar cap where the Earth's magnetic field lines are open. Pink line in panel (a) is the dusk convection reversal boundary (Adapted from Drayton, 2006).

1.4 Convection pattern in the high-latitude ionosphere, seasonal effect

Since the orientation of the Earth's magnetic dipole with respect to the solar wind direction changes seasonally, one would generally expect some seasonal variations in the convection pattern or the electric field distribution. For example, the lobe reconnection should be more prominent in summer time because the lobe lines are more exposed to the SW (Crooker and Rich, 1993). Another potentially important factor is the high conductance of the sunlit (summer) ionosphere as compared to the low conductance of the dark (winter) ionosphere, affecting the interaction between the ionosphere and magnetosphere through FACs. Importantly, the day-night gradient of the conductance experiences seasonal shifts in the magnetic latitude that also might redistribute the overall convection pattern (e.g., Benkevich, 2006). Another complicating factor is presence of inter-hemispheric currents (e.g., Benkevich, 2006). Despite the fact that all these effects have been recognized and experimental work has been ongoing for years, winter-summer asymmetries in the convection patterns have not been firmly established.

1.4.1 Overall shape of the pattern

The first to describe seasonal effects in the high-latitude convection were Friis-Christensen and Wilhjelm (1975) who examined magnetic variations in the polar cap. They reported that B_y-related currents are significantly stronger in summer time. It was not clear weather this is due to seasonal changes in the electric field since magnetometers are sensitive to the conductance which is much larger during the summer time.

One of the first studies which show the seasonal effect in the electric field (convection pattern) was done by de la Beaujardiere et al. (1991). The authors considered 5 years of the Sondrestrom incoherent scatter radar (ISR) measurements for solar minimum conditions and showed that there was a change in overall shape of the convection pattern and the magnitude of the electric field and cross polar cap potential with season. The changes in the convection pattern included: 1) rotation of the overall near-noon convection pattern toward earlier local times with respect to the noon-midnight direction during summer, 2) ~5° shift toward midnight of the line connecting the dawn and dusk potential maxima/minima locations on MLT (Magnetic Local Time)-MLAT (Magnetic Latitude) plane during summer, and 3) the lowest location of the dawn (dusk) cell convection reversal during summer (winter).

Rich and Hairston (1994) presented statistically-averaged convection patterns measured by DMSP satellites for various IMF clock angles ($\theta = \cos^{-1}(B_z/\sqrt{B_z^2 + B_y^2})$) and different seasons. They confirmed that the patterns for any B_z are strongly controlled by the IMF B_y component and found that detection of more than two-celled patterns is not very common even for $B_z>0$. The plots presented showed the effect of the overall convection pattern rotation reported by de la Beaujardiere et al. (1991) and that the dusk convection cells are more round in summer time and for $B_y>0$. For $B_y<0$, the seasonal change in the shape of the convection pattern was hardly recognizable.

With the introduction of the Super Dual Auroral Radar Network (SuperDARN) HF radars (Greenwald et al., 1995; Chisham et al., 2007), capable of producing almost instantaneous maps of the plasma convection on a global scale, statistically more valid conclusions have been drawn by Ruohoniemi and Greenwald (1996; 2005). These authors reported that the combination of B_y^+/summer (B_y^-/winter) enhances the tendency of the B_y sign factor to make the dusk and dawn

cells into more round/crescent (crescent/round) shapes and to shift the crescent cell across the midnight MLT meridian. This is in partial agreement with Rich and Hairston (1994). Interestingly enough, in the convection model by Weimer (1996), based on satellite AEC data, the seasonal effect is much less dramatic and is greater for B_y^- case. Ruohoniemi and Greenwald (2005) discovered that the CPCP increases from winter to summer, contrary to previous conclusions based on DMSP data (e.g., Papitashvili and Rich, 2002) and consistent with the fact that ionospheric horizontal currents and FACs maximize in summer, when the ionospheric conductance is largest (Iijima and Potemra, 1976; Campbell, 1982).

The solar wind is known to vary in cycles with 11-year periodicity to be the most prominent feature. The solar cycle variations in the ionospheric plasma convection have been poorly studied because of the lack of data. Ruohoniemi and Greenwald (2005) did not find any significant effect while considering SuperDARN data collected around the solar cycle 23 maximum over the period 1998-2002.

1.4.2 Plasma flow in the polar cap

Seasonal effect in the high-latitude convection pattern can be characterized in terms of the plasma flow in the central polar cap where it experiences less twists and flow is mostly in the antisunward direction, see Figure 1.5. Koustov et al. (2013) studied plasma flows in the polar cap using the Rankin Inlet (RKN) SuperDRAN radar. The authors discovered that the near-noon flows are sunward-oriented for $B_z>0$ and the effect is more clearly recognizable during the spring equinox. The antisunward flows during pre-noon hours were observed as stronger during summer time. When the RKN radar velocities were compared with the PCN magnetic index, sensitive to the combined effect of plasma velocity and conductance variations, no seasonal effect was found in the response of the velocity on the PCN increase although summer velocities were found to be, on average, larger in magnitude (Fiori et al., 2009). One important model which predicts the plasma flow in in the polar cap is the current generator model. It claims the current density is steady for different season which means one should expect larger electric field during the winter as compared to summer. Larger electric field of winter is also predicted by computer modeling of plasma flows in the Earth's magnetosphere.

1.4.3 Convection reversal boundary

As was mentioned, one of the parameters characterizing the 2-celled plasma convection pattern is a boundary of the oppositely-directed flows, the convection reversal boundary (CRB). For the plot of Figure 1.5, the CRB (the pink line) is roughly at MLAT~72°. It has been long recognized that the CRB is sensitive to the IMF B_z and B_y components (Ridley and Clauer, 1996; Rash et al., 1999). It shifts toward lower MLATs for more negative B_z values (Ridley and Clauer, 1996). Together with the CRB, the dayside region with a stagnated flow, the dayside "throat" (see Figure 1.5), shifts equatorward. It is interesting that the throat is covering the locations of the dayside cusp (Figure 1.1) that vary in magnetic latitude with season by as much as 6° being at highest (lowest) latitude in summer (winter) (Burch, 1972; Newell and Meng, 1989).

Recent study by Bristow and Spaletta (2014) gives the most comprehensive view of the response of the CRB to drivers of the ionospheric convection. The authors used 10 years of SuperDARN measurements with the standard technique of the pattern derivation (to be discussed in Chapter 2). For strong negative B_z, the CRB is located at MLAT=75° on the dayside and at MLAT=70° on the nightside (their Figure 9) so that the distribution is somewhat skewed. The boundary on the nightside CRB moves equatorward as the IMF B_z becomes more and more negative. Noticeable were dawn to dusk shifts of the CRB in response to IMF B_y variations.

1.5 External drivers of the high-latitude convection

Although it has been accepted by the space science community that the plasma flows at high latitudes are mostly controlled by the merging processes, the theory of merging has not been developed to a stage where one can predict the resultant electric field in the magnetosphere and ionosphere. It is also accepted that processes in the magnetotail affect the electric field distribution, especially on the nightside. For this reason, a number of researchers attempted, empirically and with purely theoretical arguments, an expression for a generic parameter that would characterize the efficiency of the interaction between the IMF and the Earth's magnetic field and the energy input into the magnetosphere and, eventually, into the ionosphere. None of the proposed parameters that are traditionally termed "the coupling functions", describe ideally the temporal

variations of various electrodynamical parameters in the near-Earth space. Some of them show better correlation than others for specific phenomena. Here we introduce several of those that are relevant and frequently used in convection studies.

The IMF itself can be considered a simple coupling function. Without it, no merging processes would happen. The IMF B_z component has been considered as the most important parameter in multitude of publications (e.g., Burch, 1972; Maynard and Heppner, 1987) as it is involved in the front-side merging and transpolar plasma flows, as explained in Section 1.3. But the IMF B_y component can also be important by moving the reconnection site to the flanks of the magnetosphere. It is not a surprise that many of the coupling functions contain the IMF transverse component $B_t = \sqrt{B_z^2 + B_y^2}$ and the importance of this parameter has been acknowledged in many papers (e.g., Newell et al., 2007).

If one tries to characterize the reconnection processes in terms of electric fields, then one can think of the interplanetary electric field (IEF), directed roughly from dawn to dusk in the near-Earth environment, as "mapped" into the high-latitude ionosphere along the magnetic flux lines. The mapping happens to be with an amplification factor that is hard to establish; however, one can still introduce IEF as a parameter characterizing merging, or electric field in the ionosphere, according to the equation

$$IEF = V_{SW} \cdot B_t, \tag{1.7}$$

where V_{SW} is the antisunward component of the solar wind velocity. A number of authors used this parameter for work with convection data (e.g., Newell et al., 2007; Koustov et al., 2009; Cousins and Shepherd, 2010; Koustov et al., 2013).

A more detailed description of the IMF-magnetosphere interaction can be done by introducing more sophisticated expressions (Newell et al., 2007). Sonnerup (1979) and Kan and Lee (1979) proposed a geometric coupling function which could serve as a metric for the effective interplanetary electric field coupled into the magnetosphere during sub-solar magnetic merging, E_{KL}, given by equation

$$E_{KL} = V_{SW} B_t \cdot \sin^2 \frac{\theta}{2} = IEF \cdot \sin^2 \frac{\theta}{2}, \tag{1.8}$$

where $\theta = \cos^{-1}(B_Z/B_t)$ is the IMF clock angle (in the Y-Z) plane. Parameter E_{KL} is often referred to as the Kan-Lee electric field or simply the reconnection electric field. In equation (1.8), B_y and B_z are to be taken in the GSM coordinates. The sine term in equation (1.8) emphasizes

reconnection at the sub-solar magnetopause under southward IMF. Many studies have used this parameter to correlate the interplanetary medium conditions with the cross polar cap potential (e.g., Reiff and Luhmann, 1986; Weimer, 1996; Shepherd et al., 2002).

Another way to characterize the reconnection electric field is to use the Polar Cap North (PCN) magnetic index if one is to consider data for the northern hemisphere and PCS for the southern hemisphere. The PCN index is routinely derived from data of the Thule magnetometer (located in the central polar cap, at MLAT~84°) by recalculating the raw data with a transfer function that was established while correlating magnetic perturbations on the ground and the reconnection electric field E_{KL} (Troshichev et al., 2006). The PCN index is considered to be a good proxy for the reconnection electric field, and thus is applicable to observations with $B_z<0$. In the past, in absence of direct measurements in the solar wind, the PCN index has been used widely, including work with SuperDARN data (e.g., Fiori et al., 2009; Koustov et al., 2009). Recently, quality of the PCN index has been questioned (e.g., Lukianova et al., 2002; Troshichev et al., 2006) and its use subsided. Another major weakness of the PCN index is that it cannot be used for $B_z>0$ cases.

When the IMF is northward-dominated ($|B_z|>>B_y$), the IMF clock angle is close to zero, and E_{KL} is close to zero as well. Wilder et al. (2008) proposed a new convection coupling function for this situation, the so called reverse (sunward) convection electric field E_{RC}, given by equation

$$E_{RC} = V_{SW} B_t \cdot cos^n \theta . \quad (1.9)$$

Here the power index *n* is selected empirically, and Wilder et al. (2008, 2010) use n=4.

To give a sense as to how the ionospheric plasma flow velocity intensifies with an increase of the coupling coefficient/function or in other words, with intensification of the external driver of the convection, we present examples from Troshichev et al. (2002) and Wilder et al. (2010). Troshichev et al. (2002) plotted the average electric field along the DMSP satellite path crossing the entire polar cap in the dusk-dawn direction versus PCN magnetic index (this would be close to plotting electric field versus E_{KL}), Figure 1.6. We can see as the points assume larger and larger values with the PCN increase. The authors characterized the scatter plot of Figure 1.6 by a quadratic function because at large PCNs the rate of the polar cap electric field increase slows down. This is the so called saturation effect in the cross polar cap electric field at large reconnection fields. This effect was a subject of a number of publications (e.g., Fiori et al., 2009). For the linear part of the curve, a doubling in PCN increases the cross polar cap electric field by a factor of ~1.5.

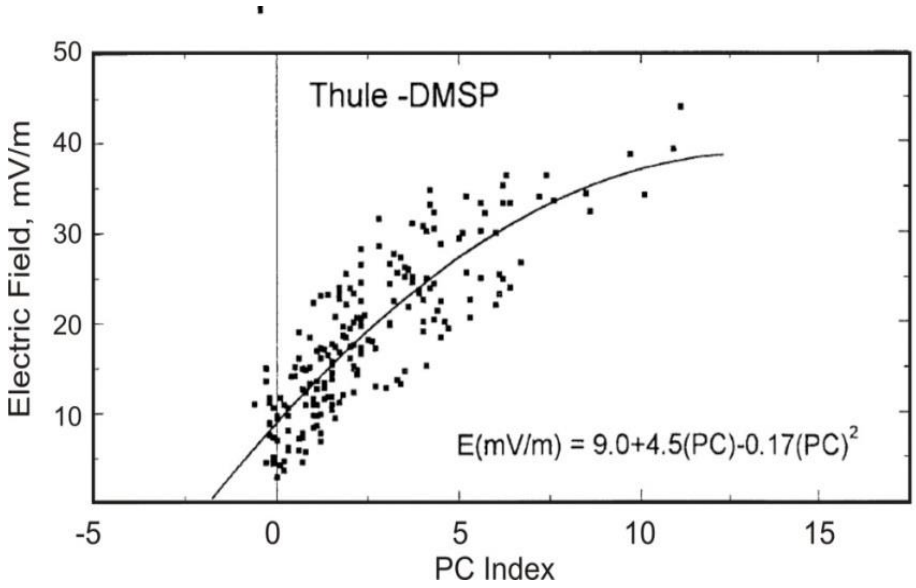

Figure 1.6: A scatter plot of the northern polar cap electric field (inferred from DMSP ion drift measurements) versus the PC index obtained from Thule magnetometer data. Given at the bottom is the expression of the polynomial fit to the data (Adapted from Troshichev et al., 2000, publisher permission of the use was obtained).

Wilder et al. (2010) investigated the transpolar plasma flow velocity inferred from SuperDARN data for B_z^+ and B_Z^- conditions. Figure 1.7 shows plots of the velocity binned by the E_{KL} as a coupling function for southward IMF (Figure 1.7a) and E_{RC} as the coupling function for northward IMF (Figure 1.7b) for the months of May through August. We note that both coupling functions are presented not in mV/m, which are natural units for the electric field, but in kV per Earth's radii, R_E. This is done to make a comparison with other publications in this area. Figure 1.7 shows that as the drivers of the convection increase, the velocity increases as well but up to a certain value. For the B_z<0 case, the increase seems to stop at E_{KL}=25 kV/ R_E while for the B_z>0 case, it stops at E_{RC}=20 kV/Re. This is again the transpolar velocity saturation effect but with respect to SuperDARN radar data. We can conclude from Figure 1.7 that the transpolar velocity increases by a factor of 1.5-3 for typical solar wind IMF conditions during summer time. Perhaps somewhat strangely, the flows are faster for B_z>0 reaching ~500 m/s (versus ~350 m/s for B_z<0).

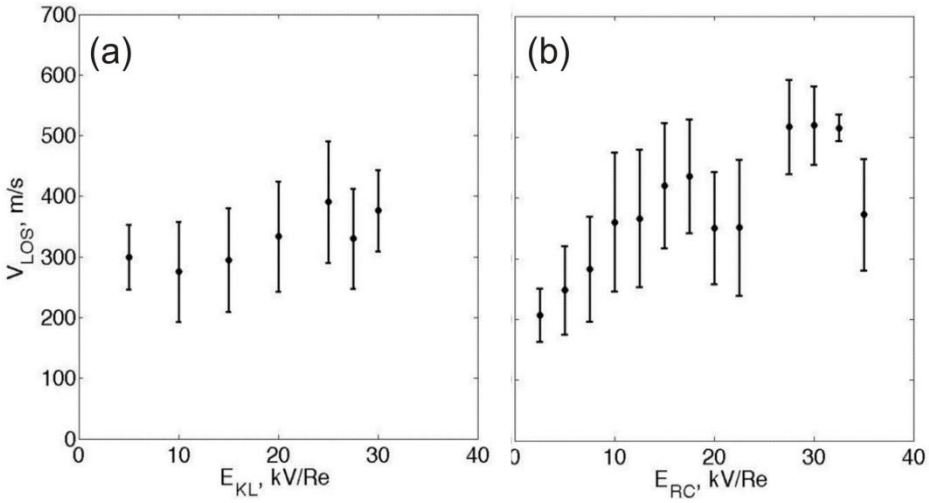

Figure 1.7: Inferred velocity of the transpolar plasma flow along the noon-midnight meridian (denoted as VLOS) for the months of May through August versus reconnection electric field. (a) VLOS for southward IMF against E_{KL}. (b) VLOS for northward IMF against E_{RC}. The dots represent the average VLOS for each bin of E_{KL} or E_{RC}, and the overall length of the error bars is the standard deviation of the VLOS in each bin (Publisher's permission for the use of the diagram was obtained).

1.6 Objectives of undertaken research

This thesis is aimed at investigation of the long-term and large-scale variability of the plasma flows in the high-latitude ionosphere and its relationship with variations of the solar wind parameters and the IMF, with the emphasis on the flows in the polar cap, at high magnetic latitudes of >70°. The goal is to take advantage of extensive SuperDARN data accumulated over many years of operation.

At the beginning of the research the targets were more specific; we wanted to investigate the seasonal and solar cycle variations of the electric field magnitude at latitudes of ~83°, in the vicinity of the Resolute Bay (RB) observatory. The topic was instigated by an effort to understand the reasons for occurrence/absence of the SuperDARN echoes over RB (Ghezelbash et al., 2014), more specifically whether strong electric fields are generally needed to detect SuperDARN F region echoes. The latitudes selected are of interest for other reasons as well: at Resolute Bay, two other convection–monitoring instruments are operational, the CADI ionosonde and the incoherent scatter radar AMISR-N, and it would be important to establish in which sense these instruments are complimentary. For example, the AMISR radar has superior spatial resolution but it is operated

just for a few days in a month. Knowing long-term variability of the convection over RB would allow one to better plan special coordinated experiments with this expensive instrument.

The project eventually evolved into a more general investigation of the plasma flows and relationship/correlation with the parameters of the solar wind and interplanetary magnetic field. One interesting question that we had in mind is whether the electric fields in the polar cap are, on average, larger in winter time as compared to summer time as predicted by computer modeling of plasma flows in the Earth's magnetosphere (e.g., Cnossen et al., 2012). Finally, electric field is one of the major electrodynamical parameters of the ionosphere, and knowing its seasonal and solar cycle trends would allow one to better specify and forecast Space Weather.

More specific targets of the Thesis are:

1. Investigate features of the monthly-averaged convection patterns inferred from the SuperDARN gridded velocity data by application of the technique by Fiori et al. (2010) to all measured velocities, without considering the IMF and solar wind conditions. The targets are locations of the convection reversal boundary and dayside throat, and identification of the velocity magnitude maxima (its magnetic local time) in the auroral zone and the polar cap.
2. Identify the relationship of the averaged flows in the polar cap with parameters of the solar wind and IMF by applying very coarse bins to all SuperDARN gridded velocity data processed with the same technique. The thrust of the investigation was on long-term changes in the patterns for IMF $B_z<0$ and $B_z>0$ cases, for example how the intensity of the flow changes within the solar cycle.
3. Investigate the relationship of the meridional component of the polar cap plasma flow and intensity of the reconnection electric fields for $B_z<0$ and $B_z>0$ and for observations at near-noon hours. To accomplish this, directly-measured velocity of the flow in the meridional direction by two high-latitude radars are to be compared with the reconnection electric field data from measurements in the solar wind.

The research undertaken addressed general questions on the nature of the interaction between the solar wind/IMF and the Earth's magnetic field. It does not have immediate impact on practical system operation. However, understanding general physical processes in the near-Earth environment would allow physicists to more precisely specify and predict the electrodynamical parameters in near space that are cumulatively referred to as Space Weather. It is well documented that when strong and dense solar wind clouds reach the near-Earth environment, a large number of phenomena occur. Among these, some are harmful for human operation in space and on the

ground. For example, a range of technologies on the ground, such as transformers, can be damaged. Navigation of satellites and operation of GPS systems might experience interference problems. In space human beings can be affected. That is why, studying the Sun-Earth connections are important and will continue in years to come.

1.7 Thesis outline

The remainder of this Thesis is organized as follows. Principle of the SuperDARN HF radar operation, method of the velocity determination and techniques for global convection pattern construction from velocity data of multiple SuperDARN radars are discussed in Chapter 2. Chapter 3 analyses features of the high-latitude convection for the case the averaged SuperDARN convection patterns are inferred without consideration of conditions in the solar wind while Chapter 4 analyses features of the convection pattern while the same data are split in some bins of the IMF. Chapter 5 considers dependence of the near noon plasma flows upon reconnection electric fields E_{KL} and E_{RC}. Finally, in Chapter 6, potential extensions of the performed work are discussed.

CHAPTER 2

SUPERDARN RADARS

Super Dual Auroral Radar Network (SuperDARN) is a multi-national network of HF radars continuously detecting echoes from the Earth's ionosphere (Greenwald et al., 1995; Chisham et al., 2007). There are currently 32 radars with 21 (11) radars operating in the northern (southern) hemisphere. The network is continuously expanding to achieve better echo coverage and thus to obtain more reliable maps of the ionospheric plasma circulation.

2.1 Principle of SuperDARN radar operation. Coherent backscatter

The SuperDRAN radars detect several types of echoes, Figure 2.1. These are echoes from the D or E region bottom-side (polar summer mesospheric echoes and meteor-related echoes), ionospheric echoes from the E and F regions (IS) and ground scatter echoes (GS). Details on each type of echoes can be found in Chisham et al. (2007). The scatterers responsible for the echoes are located at certain heights and to reach them, specific ray paths are required. Figure 2.1 illustrates various possible radio wave paths for echo detection with SuperDARN HF radar.

For the undertaken research, coherent echoes from the ionosphere are important. The SuperDARN radars operate at frequencies well above the critical frequency of the ionospheric layers so that one would not expect any directly-reflected echo signal from the ionosphere. This is shown by the path 1 in Figure 2.1. However, in the presence of ionospheric structures, which are often organized into wave-like formations, weak signals are detectable provided that the integration time of a signal is not very short. Such signals can come from either the E or F region.

The scattering process can be considered in analogy with the Bragg scattering of electromagnetic waves from a crystal. In a case of backscatter, for an electromagnetic wave with wavelength λ_r, the scattered fields (from various parts of the ionospheric quasi-periodic structure) would interfere constructively if the spatial scale of the structures λ_{irr} is 2 times shorter than the radar wavelength; $\lambda_{irr} = \lambda_r/2$ (Fejer and Kelley, 1980).

An important property of ionospheric irregularities, especially at high altitudes, is their strong alignment with the Earth's magnetic field because of much slower mobility along the magnetic field. For this reason, the ionospheric irregularities are often called field-aligned irregularities (FAI). To get significant backscatter from FAI, radio waves should propagate almost perpendicular to them, i.e. perpendicular to the Earth's magnetic field lines. This is not easy to achieve at high latitudes as the geometrical angles (radar look angle with respect to the normal to the magnetic field lines) are on the order of 10° or higher. Radar operation in the HF band allows one to overcome this difficulty. This is because radios waves in this frequency range can easily refract by 10° and more so that the orthogonality condition between the radar wave and the Earth's magnetic field would be satisfied.

The above points are illustrated in Figure 2.1. We assumed here that the FAIs exist everywhere in the ionosphere. The orthogonality condition is achieved through ionospheric refraction dependent on the electron density distribution in the ionosphere. For F region heights, it is satisfied at ranges of ~800-1200 km for typical high-latitude observational conditions (ray 2 in Figure 2.1). In this case, the echoes are said to be received by means of the ½-hop (direct) propagation path (e.g., Milan et al., 1997). Some radio waves, can propagate farther into the ionosphere, refract, bent to the Earth's surface and then reflected back into the ionosphere where they can meet the ionospheric irregularities and be backscattered. This can happen at large ranges of ~2500-3000 km. Such coherent echoes are called the 1½-hop (propagation mode) echoes (e.g., Milan et al., 1997). The ionospheric E region can also support both the ½-hop and 1½-hop echoes (ray 4 in Figure 2. 1). Clearly, a single HF radar can detect echoes from a band of range. This is why, to have good data coverage, many HF radars with spatial separation are needed to successfully monitor the high-latitude ionosphere by means of ionospheric scatter. It is also clear that the number of detected echoes, and success in monitoring of the ionosphere, depends strongly on the electron density distribution. As the Sun's illumination varies with time of the day and season, the quality of ionosphere monitoring with HF radars depends not only on the radar location but also upon time of the day. Additionally, long-term solar activity cycles affect the HF radar operation through changing the regular electron density distribution pattern due to particle precipitation from the magnetosphere.

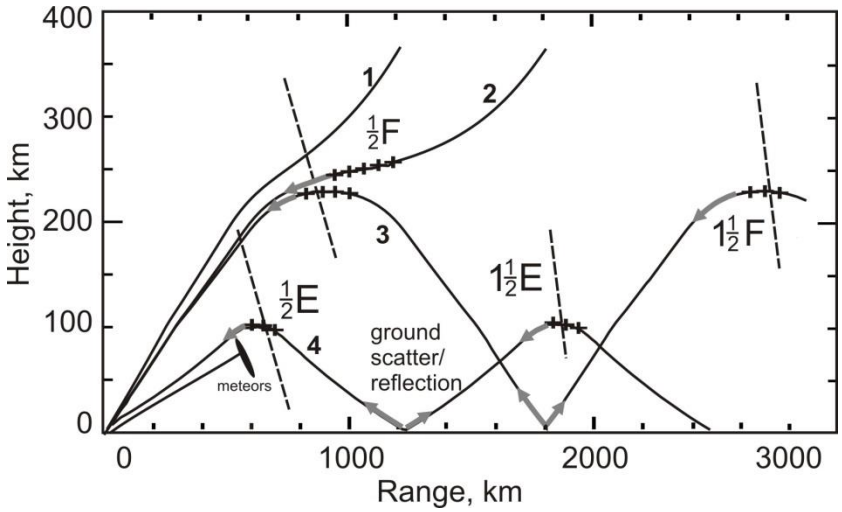

Figure 2.1: A plot illustrating possible propagation modes of HF signals in the Earth's ionosphere. Near noon spring observations with the Rankin Inlet radar (10 MHz) are assumed. Sloped dashed lines are the geomagnetic field lines. Black crosses correspond to those regions where the orthogonality condition is satisfied and the backscatter is possible. Several rays are shown: ray 1 penetrates through the ionosphere without any echo, ray 2 gives backscattered signal through ½-hop propagation mode (F region), ray 3 gives echo through 1½-hop propagation mode (F region), and ray 4 is similar to rays 2 and 3 but for the E region heights (Adapted from Ghezelbash et al., 2015).

An important aspect of SuperDARN work is identification of types of signals. While at shortest ranges, the ground scatter is practically impossible, at ranges above several hundred kilometers, such echoes occur very often simultaneously with ionospheric scatter (e.g., Milan et al., 1997). To identify GS a set of conditions is applied to the echo parameters (Blanchard et al., 2009): namely, the velocity magnitude of echoes is very low, roughly < ~ 20 m/s, and the echoes are narrow in spectral width, roughly < 30 m/s. The problem of echo identification is especially acute for the radars operating at middle latitudes. Here, the ionospheric echoes can have parameters comparable to those of the GS echoes and a special, more rigorous technique has been developed to distinguish ionospheric and ground scattered echoes (Ribeiro et al., 2011; 2013). Since this new technique has not been adopted by the SuperDARN community, in this Thesis the data were processed with the standard method of Blanchard et al. (2009).

Following is more detail about ionospheric irregularities. They are setup through structured particle precipitation (scales of >1 km) and plasma instabilities (100 - 1 m). For HF radars monitoring decameter irregularities, plasma instability processes are very important. This is because obtaining such short-scale structures directly from particle precipitation is very unlikely. One of the most important processes is the gradient-drift (GD) plasma instability that is excited

when there is a relative drift between electrons and ions in the direction perpendicular to the magnetic field and ambient plasma gradient across the magnetic field (Kelley, 1989). For F region altitudes, the plasma density gradient is preferably to be oriented in the direction of $\vec{E} \times \vec{B}$ bulk plasma drift. These conditions are easily met at high latitudes where plasma is strongly inhomogeneous and where there are electric fields of magnetospheric origin as discussed in Chapter 1. The relative drift at F region altitudes exists because of different ion and electron mobility in the direction of an electric field (Pedersen drift, Section 1.2).

The plasma instability means that spontaneous perturbations in the electron density at a thermal level can be amplified through micro-feedback processes in the plasma. In the case of the GD instability in the F region, the excitation of the plasma polarization electric field of a perturbation moves regions with electron density enhancements into the region of smaller ambient density thus increasing the contrast of the perturbed density as compared to the background. At a later stage of this process, nonlinear effects step in and stop the growth of the perturbation at a certain level; this level is on the order of several percent. Such amplitude of the electron density perturbations is sufficient to detect HF coherent backscatter. There is no detectable threshold on the drift for the instability to initiate except that the instability would be slow in the presence of slow drift and/or weak plasma gradient. More detailed information on the GD instability process can be found in Kelley (1989).

2.2 Radar fields of view and technical characteristics

Figure 2.2 shows the field-of-views (FoVs) of the currently-operating SuperDARN radars in the northern hemisphere; data from these radars will be used in this Thesis. We are not presenting here detailed information on the radar location and field-of-view (FoV) orientation as it is readily available at the main SuperDARN website at Virginia Tech - http://vt.superdarn.org/tiki-index.php. We also need to note that we will consider data collected for various years, including the beginning of the SuperDARN experiment when only several radars were available.

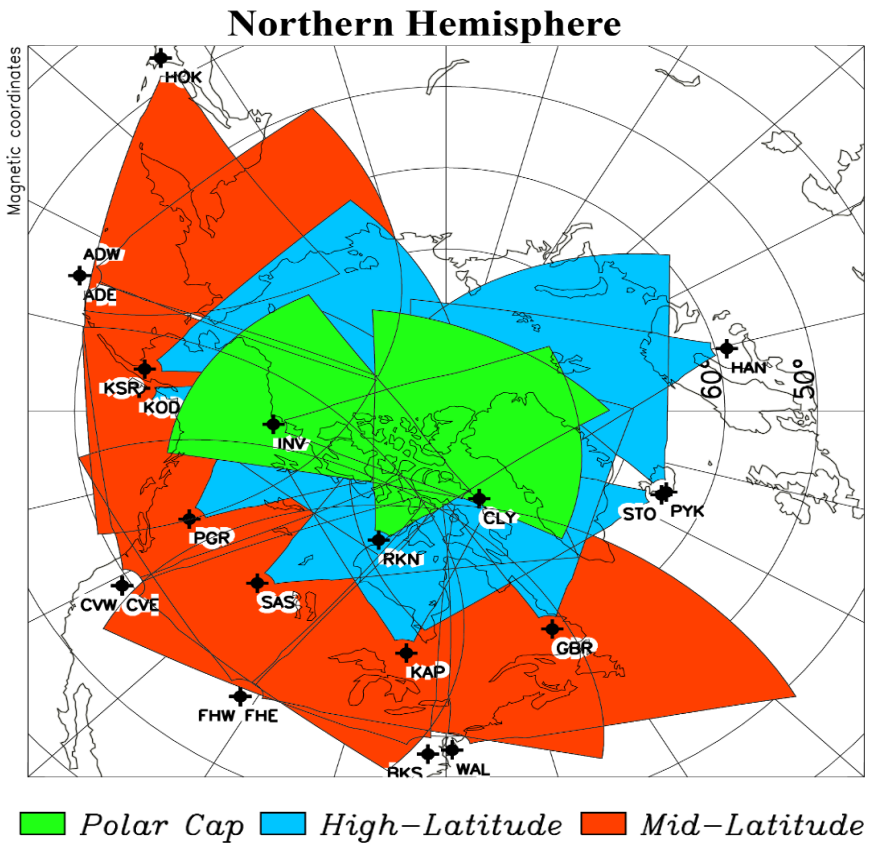

Figure 2.2: Fields-of-view of the currently-operating Super Dual Auroral Radar Network radars in the northern hemisphere (http://vt.superdarn.org/tiki-index.php). Coloring reflects typical latitudes mainly targeted by the individual radars.

The SuperDARN radars operate by transmitting radio pulses at fixed frequencies (ranging from 8 to 20 MHz) and analyzing parameters of echo signals arriving back due to backscatter from the ionospheric FAI with the wavelengths between 7 and 18 m, as given by the Bragg scatter condition. For a number of years, most of the SuperDARN radars had been operating in the "sounding" mode for which scanning for best frequencies for echo detection had been done a fixed period of time (often 15 min or shorter) so that the radar transmission frequency could be adjusted. Over the last two years, the Canadian SuperDARN radars typically use 2 alternating, more or less fixed, frequencies so that the scans alternate between ~10 and 12 MHz.

Although the hardware is not the same for all the radars, the mode of operation is similar. Each radar scans over 16 beam positions, separated by ~3.24° in azimuth. Currently, the scan lasts one minute so that beam dwelling time in any position is ~3 s. The data are collected, for each beam, in 75 (and more for some radars) range gates of 45-km length, starting from the range of 180 km. The radars thus have range coverage from 180 to 3555 km. The radars currently use a

special 8-pulse sequence, with basic pulse lag time of 2.4 ms and the length of each pulse of 0.3 ms.

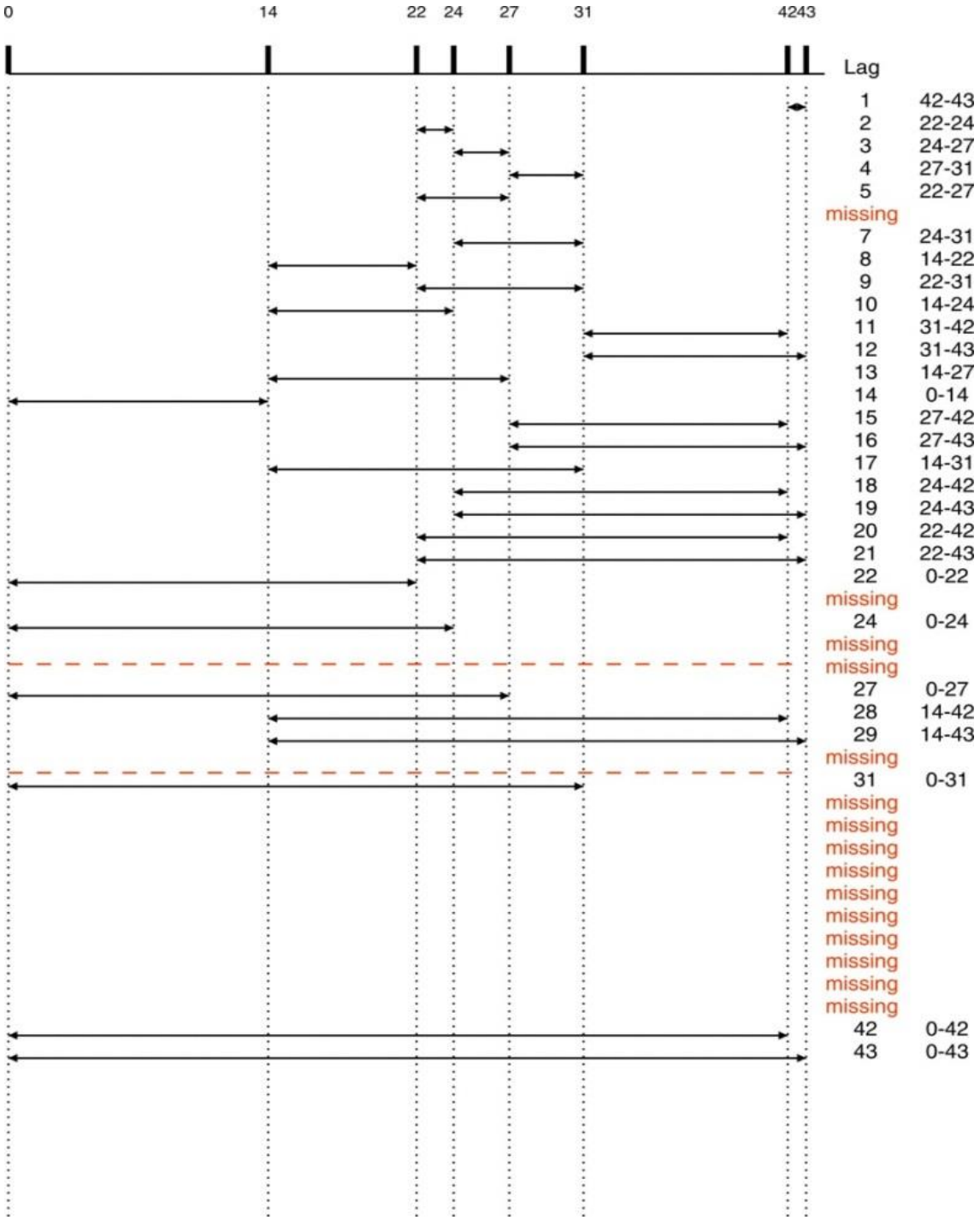

Figure 2.3: Scheme of the 8-pulse sequence ("katscan") currently used by the majority of the SuperDARN radars (Courtesy A. S. Reimer).

Figure 2.3 shows the scheme of pulse sequence currently employed by the majority of the SuperDARN radars. The horizontal bars in Figure 2.3 indicate pairs of pulses that are correlated in the analysis. The length of the bars reflects the time separation between the pulses; the separation is counted in units of main lag time of 2.4 ms. One can notice that some pairs are indicated as missing. These are sometimes called the systematic badlags. They occur because the correlation computation between the pulses is impossible due to the need to shut down the receiver during multipulse transmissions as the SuperDARN radars use the same antennas to transmit and receive signals. The position of systematic badlags depends on the pulse length/sequence, lag to the first range and the lag separation; they are predictable. Details of how to identify the systematic badlags can be found in Huber (1999).

Multi-pulse sequence of transmission allows one to compute the auto-correlation function (ACF). Analysis of the ACF provides an opportunity to determine parameters of radio echo such as the power, Doppler velocity, and spectral width, as discussed below.

2.3 Essence of the ACF approach for echo analysis

In SuperDARN measurements the Doppler velocity of ionospheric echoes is the most important parameter. We explain here details of how this parameter is inferred from raw data within the ACF approach.

To start and for simplicity, let us consider a 2-pulse sequence with the pulse lag time τ as shown in Figure 2.4. To get the velocity, we want to measure by how much the scattering region (irregularities) at a desired distance d_0 would move over the time τ. If the first (second) pulse is transmitted at time $t_0 (t_0 + \tau)$, then it will be received from the distance d_0 with the amplitude of $A_1(d_0)$ and at time $t_1 = t_0 + 2d_0/C$ (C is the speed of light). At the same time t_1, part of pulse 2 can be received back from the distance d_- with the amplitude of $A_2(d_-)$. So, at time t_1 the total measured echo amplitude can be written as

$$A(t_1) = A_1(d_0) + A_2(d_-). \quad (2.1)$$

At the time $t_1 + \tau$, pulse 1 arrives from a distance d_+ with the amplitude of $A_1(d_+)$ and pulse 2 arrives from a distance d_0 with amplitude of $A_2(d_0)$. Then the amplitude of total received signal at $t_1 + \tau$ is

$$A(t_1 + \tau) = A_1(d_+) + A_2(d_0), \tag{2.2}$$

we can construct the mean ACF of the received signals at lag τ as

$$\langle A(t_1) \cdot A(t_1 + \tau) \rangle = \langle A_1(d_0) \cdot A_2(d_0) \rangle + \langle A_1(d_0) \cdot A_1(d_+) \rangle + \langle A_2(d_-) \cdot A_1(d_+) \rangle + \langle A_2(d_-) \cdot A_2(d_0) \rangle, \tag{2.3}$$

equation (2.3) shows that the ACF contains four terms for lag time τ, but the desired distance d_0 in both signals stays only in the first term, so only these signals originated from the same point. Other terms 2, 3 and 4 contain signals that came back from unwanted distances; these signals do not correlate while many pulse sequences repeated and averaged. The average of the last three terms in equation (2.3) would be zero. If we ignore terms 2, 3 and 4 in the mean ACF for simplicity, equation (2.3) reduces to

$$\langle A(t_1) \cdot A(t_1 + \tau) \rangle \approx \langle A_1(d_0) \cdot A_2(d_0) \rangle, \tag{2.4}$$

the last equation (2.4) can be rewritten in terms of its amplitude Am and phase φ as follows

$$\langle A(t_1) \cdot A(t_1 + \tau) \rangle \approx A_m e^{i\varphi}. \tag{2.5}$$

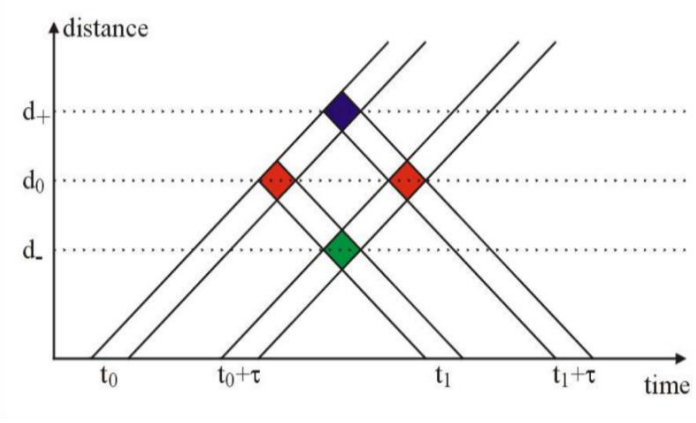

Figure 2.4: Range-time diagram for a 2-pulse sequence (Courtesy M. Ghezelbash).

Although we discussed the ACF determination procedure for 2 pulses, the multi-pulse SuperDARN transmissions are dealt in similar way except of the number of possible lags can be as large as 18-20. In this way, the measurement of the amplitude and the phase can be combined at various time lags.

Figure 2.5a gives an example of the backscattered signal phase measurements and calculated ACF of good quality. Both real and imaginary parts of the ACF show smooth variations. Data for all expected lag numbers are available. Missed data for lags 6 and 23 are also identifiable. Figure 2.5b shows variation of the ACF phase inferred from the data shown in Figure 2.5a. Figure

2.5b shows one peculiar feature of the ACF behavior; we see that the phase of the ACF experiences jump at lag number 15. The radar software automatically "shifts" the phase as shown in Figure 2.5c and analyzes the adjusted data.

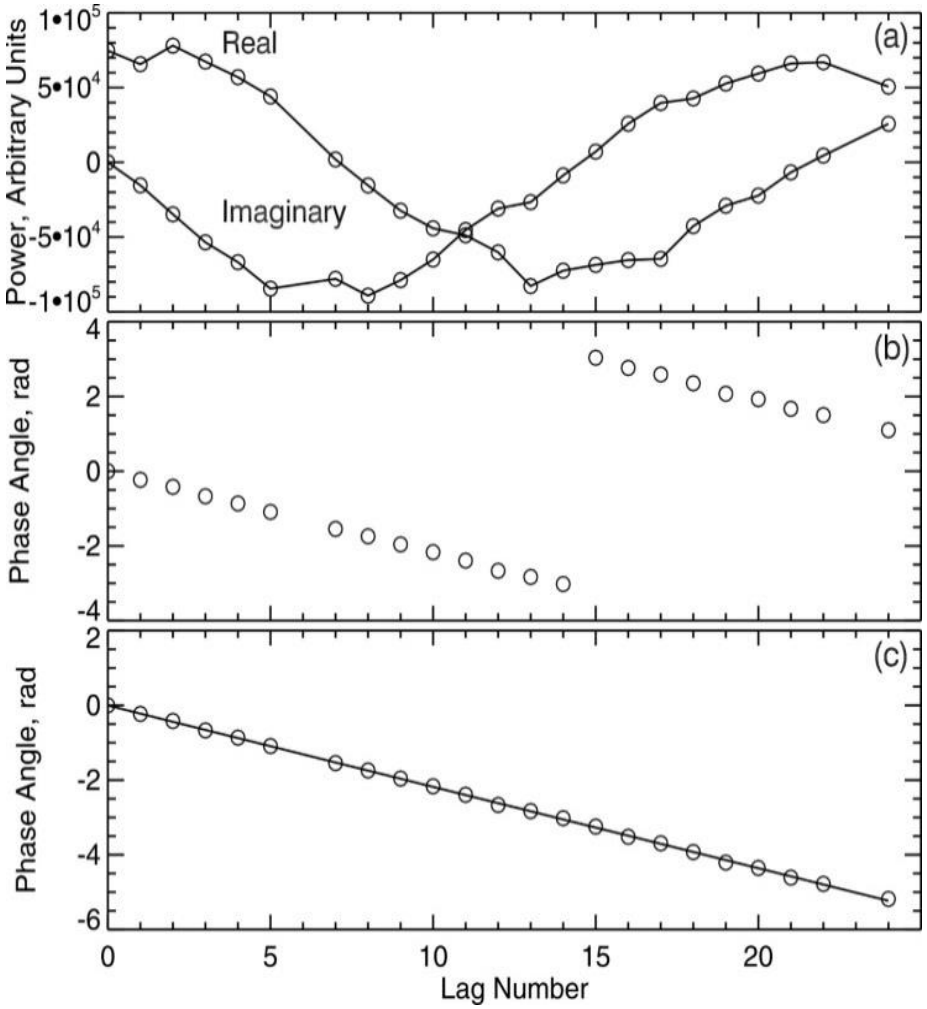

Figure 2.5: Example of the phase measured by the Clyde River SuperDARN radar on 5 January 2014. (a) The real and imaginary parts of the ACF versus time lag number (b) The phase of the ACF versus time lag number (c) The unwrapped phase of the ACF versus time lag number and the linear fit line. The slope of the line is 90.28 rad/s.

While correlating real pulses, the data are not as good as those of Figure 2.5. Additional lags also get "missed", but not because of the hardware limitations. This happens due to the fact that strong signals from unwanted ranges contribute to the ACF values (making the noise level very large in a specific lag and the data "outlie" the expected "decay" of the ACF with lag number) and thus the obtained value of the ACF cannot be trusted. Cancellation of the ACF phase due to the contribution from "unwanted" ranges may not occur as well for these lags. These lags are

termed the range interference badlags. It is very important to identify such situation and exclude corresponding lag data from the analysis. Currently, SuperDARN uses an ad hoc method to determine the bad lags caused by range interference. If the signal from the unwanted range is larger than the signal from the wanted range, then the lag is not considered.

2.4 Line-of-sight velocity determination in SuperDARN measurements

Here we give a brief description of the velocity measurement procedure. The Doppler velocity of echoes, often referred to as the line-of-sight (LOS) velocity, can be obtained by performing a least square fit to the phases obtained at the respective lags of the ACF. Mean Doppler shift frequency $\langle \omega_D \rangle$ is

$$\varphi_k = \langle \omega_D \rangle k\tau, \tag{2.6}$$

in Equation (2.6) τ is the time length of one lag and k is the set of integers. The Doppler frequency $\langle \omega_D \rangle$ can then be converted into the Doppler velocity as

$$V_I = \frac{C\langle \omega_D \rangle}{4\pi f_T}, \tag{2.7}$$

where C is the speed of light and f_T is the frequency of transmission. Following is the derivation of (2.6) and (2.7). The observed Doppler velocity corresponds to the line of sight velocity of the irregularity from which backscatter occurs. The Doppler velocity, f_D, consists of two shifts. First, the frequency f_I measured in an inertial system moving with the velocity of the irregularity V_I is

$$f_I = f_T \left(1 + \frac{V_I}{C}\right), \tag{2.8}$$

in second shift, the receiver would receive the frequency f_R from a moving source as

$$f_R = f_I \left(1 + \frac{V_I}{C}\right), \tag{2.9}$$

combining these two equations results in

$$f_R = f_T \left(1 + \frac{2V_I}{C} + \frac{V_I^2}{C^2}\right), \tag{2.10}$$

neglecting the quadratic term, V_I can be expressed as

$$V_I = \frac{C}{2} \cdot \frac{f_R - f_T}{f_T} = \frac{C}{2} \cdot \frac{f_D}{f_T}, \tag{2.11}$$

where $f_D = f_R - f_T$. Since the Doppler frequency is $f_D = \omega_D/2\pi$, the LOS velocity can be obtained by Eq. (2.7). For the example considered in Figure 2.5, the velocity is 200.4 m/s.

2.5 Convection map derivation from LOS data of multiple SuperDARN radars

Ruohoniemi and Baker (1998) introduced a map potential approach which is currently used for making convection maps. In this approach the observed LOS velocities by all available SuperDARN radars are fit into a statistical convection pattern, based on the IMF. The method works as follows.

First, the observed LOS velocities are "median filtered" which means that the observation in cells which are classified as ground scatter and those with velocity error more than 200 m/s would be discarded. Then for each cell, c_i, at scan time t_i, a data set is generated including observations from a 3×3 region of cells centered on c_i for the three scans centered at t_i. Then the median value of the data set is assigned to cell c_i. The standard deviation would be calculated for the data set of median filtering, and any points > 2 standard deviations from the mean of the data set would be discarded. Finally, data from all the radars are averaged into a grid of equal area cells, with averaged gridded velocities at the centers of the gridded cells. These grid cells are separated by a distance equivalent to 1° of MLAT to have a more even distribution of points. For the time of the pattern determination, the IMF B_z and B_y are determined from Advanced Composition Explorer (ACE) satellite measurements with appropriate time delays implemented.

For an estimated IMF condition, the so called Heppner-Maynard (HM) boundary location is determined, i.e. the boundary where the ionospheric potential is set to 0 thus not allowing for the ionospheric currents to flow equatorward of the boundary. In reality, the coordinates of the input gridded LOS velocities are confined to the high latitude convection zone of θ_{FIT}. In the gridded velocity space, all points void of real measurements, are filled with the values from the convection model. The data are "spread" over the entire sphere so that a spherical harmonic analysis can be performed to generate a convection map which would be reassigned to the high latitude region.

To map an ionosphere convection pattern, gridded velocities are first related to electrostatic potential which is the solution of Laplace equation, the solution is series of polynomials which satisfies boundary condition and orthogonality .The input velocities are introduced according to

the co-latitude θ and longitude φ. The redistribution of data points to the entire sphere is performed by multiplying a stretching factor to co-latitude θ. So, θ' is a new co-latitude of the input vector. The input velocities are related to the electrostatic potential which is represented as a series of Legendre polynomials as follows

$$\Phi_E(\theta', \varphi) = \sum_{k=0}^{K_{max}} \sum_{m=0}^{k} [A_{km}\, cos(m\varphi) + B_{km}\, sin(m\varphi)]\, P_k^m(cos\, \theta'). \tag{2.12}$$

In Equation (2.12) which is a solution of Laplace equation, the $P_k^m(cos\, \theta')$ represents the Associated Legendre Function of the first kind of integer degree k and order m, K_{max} is the maximum degree, and A_{km}, B_{km} are the constant coefficients. Electrostatic potential equation and velocity equation

$$\vec{E} = -\nabla\Phi_E, \tag{2.13}$$

$$\vec{V} = \frac{\vec{E} \times \vec{B}}{B^2}, \tag{2.14}$$

are used to find the velocity. In (2.13), (2.14) $\vec{E}$ is the electric field and $\vec{V}$ is the velocity on a spherical shell and $\vec{B}$ is the Earth's magnetic field. The coefficients are selected through a minimization procedure that seeks minimum standard deviation of the measured and estimated LOS velocity for all points on the sphere. It means that the fitting coefficients are determined by minimizing the quantity

$$\chi^2 = \sum_{i=0}^{N} \frac{1}{\sigma_i^2} (\vec{V}_i \cdot \hat{k}_i - V_{los_i})^2, \tag{2.15}$$

where σ_i is the error in V_{los} and $\hat{k}_i$ is the unit vector along the specific radar beam. Figure 2.6 gives an example of the SuperDARN convection pattern based on the FIT technique. It is a 2-min map obtained on 15 March 2001 between 18:00 and 18:02 UT.

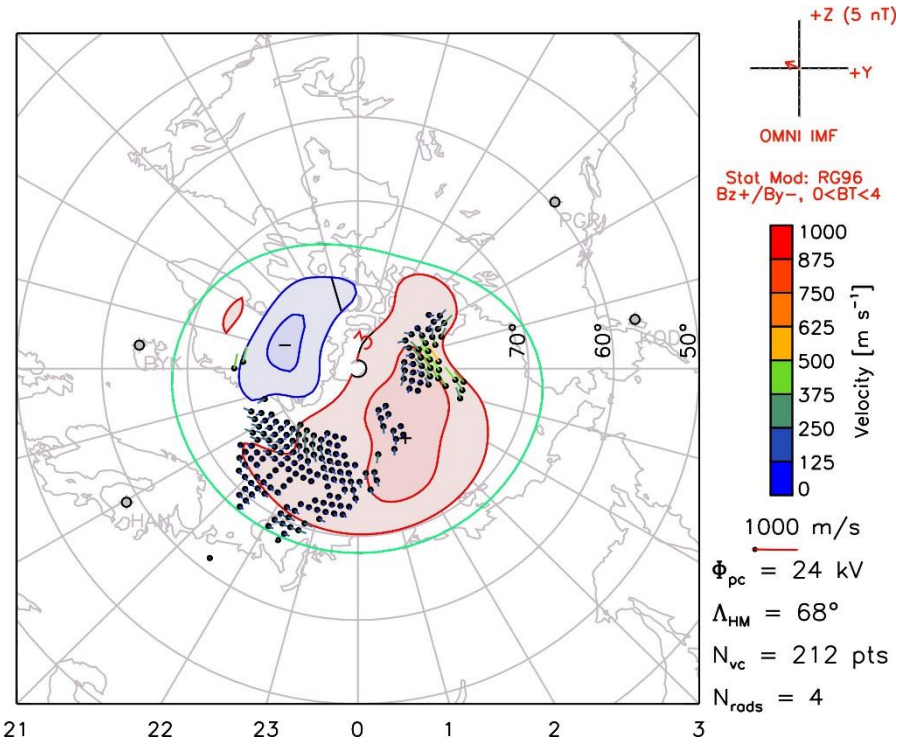

Figure 2.6: A standard 2-min convection pattern inferred from all available SuperDARN LOS velocity data on 15 March 2001 between 18:00 and 18:02 UT. The plot was taken from the SuperDARN main website (http://vt.superdarn.org/tiki-index.php); it is based on the FIT technique. On the right, the following information is presented (from top to bottom): the IMF conditions, statistical model used for fitting (RG96), cross polar cap potential, latitude of the Heppner-Maynard boundary, the number of vectors available and the number of radars contributing to the map.

2.6 Spherical Cap Harmonic Analysis of SuperDARN data

In the standard Potential Fit SuperDRAN technique, as described above, the solution is selected as a series of Legendre polynomials with integer index because this is the solution of the Laplace equation in spherical coordinates. In this Thesis, we consider alternative approach, the spherical cap harmonic analysis (SCHA) method, developed by Fiori et al. (2010). In this method, a set of observations of the ionospheric plasma drift, confined to an arbitrary located cap of half-angle θ_c (cap-size), is considered, and a new coordinate system of (θ, φ) is used, which is spherical polar coordinate system. The method is based on the same procedure of separation of variables in the Laplace equation in the spherical polar coordinates, but there is a difference.

The electric potential is represented here by a series of Associated Legendre Function of non-integer degree $n_k(m)$

$$\Phi_E(\theta,\varphi) = \sum_{k=0}^{K_{max}} \sum_{m=0}^{k} [A_{km}\, cos(m\varphi) + B_{km}\, sin(m\varphi)]\, P^m_{n_k(m)}(cos\,\theta). \quad (2.26)$$

Expression for the potential (2.26) is similar to the potential used in the FIT technique, except for the non-integer degree of P. The non-integer degree of the potential equation has been introduced to satisfy the boundary conditions (Haines, 1985). The first boundary condition requires continuity of the potential and its derivative in longitude. It means the potential and its derivative have equal values at φ and $\varphi + 2\pi$ for an arbitrary θ. This will restrict index m to be both real and integer. The second boundary condition requires regularity of the potential at the spherical cap pole and the cap edge. Equations (2.27) and (2.28) are boundary condition at the spherical cap pole

$$\Phi_E(0,\varphi') = 0, \quad m \neq 0, \quad (2.27)$$

$$\frac{\partial \Phi_E(0,\varphi')}{\partial \theta'} = 0, \quad m = 0, \quad (2.28)$$

while equations (2.29) and (2.30) are boundary conditions at the edge of the spherical cap (Haines, 1985)

$$\Phi_E(\theta_C,\varphi') = f(\varphi'), \quad (2.29)$$

$$\frac{\partial \Phi_E(\theta_C,\varphi')}{\partial \theta'} = g(\varphi'). \quad (2.30)$$

Haines (1985) shows that the second boundary conditions is met by choosing $n_k(m)$ at pole and edge of the cap in a way that $n_k(m)$ is not necessarily an integer. This is instead of setting the potential to zero at the HM boundary in the Potential Fit approach. To satisfy the condition at pole, the Associated Legendre Function of the first kind is needed. Fiori et al. (2010) and Haines (1985) presented details as to how to handle the equation for $n_k(m)$ and select the Legendre functions. Finally, after the non-integer index is determined, the series can be used to solve for the electrostatic potential, velocity, and electric field at any point within the spherical cap. Fitting coefficients can be determined as in previous Section, by using the new spherical cap coordinate system. In a case of placing a spherical cap center over the North Pole and the edge of the spherical cap coinciding with the boundary of the high-latitude convection zone, the potential can be set to zero at this boundary and, in this case, the approaches are similar.

In summary, the steps to generate a SuperDARN convection map with the SCHA mapping technique are as follows: (1) collect and pre-process LOS velocities as explained in Section 2.5, (2) select the central coordinates of the spherical cap, (3) create new redefined coordinate system

if the central coordinates are not located at North Pole, (4) select θ_c, (5) determine non-integer degree for application of the SCHA fitting and (6) calculate the fitting coefficients similarly to the procedure described in pervious Section 2.5.

Figure 2.7 shows a convection pattern obtained by applying the SCHA technique to March 2001 data. Here each dot corresponds to the grid point at which velocity value was available. At each grid/dot, the velocity vector has been plotted. The velocity vectors are not seen because of their close location, and only color, reflecting velocity magnitude, is recognizable. The black contours are the lines of equal potential 6 kV apart with the difference between the maximum and minimum values of the potential (CPCP) of 42.1 kV. One obvious advantage of the plot as compared to that of Figure 2.6 is that the data coverage here is significantly better which guarantees a more reliable numerical solution for the pattern. The similarity between the plots is their 2-cell shaped circulation pattern. We will come back to this plot in Chapter 3.

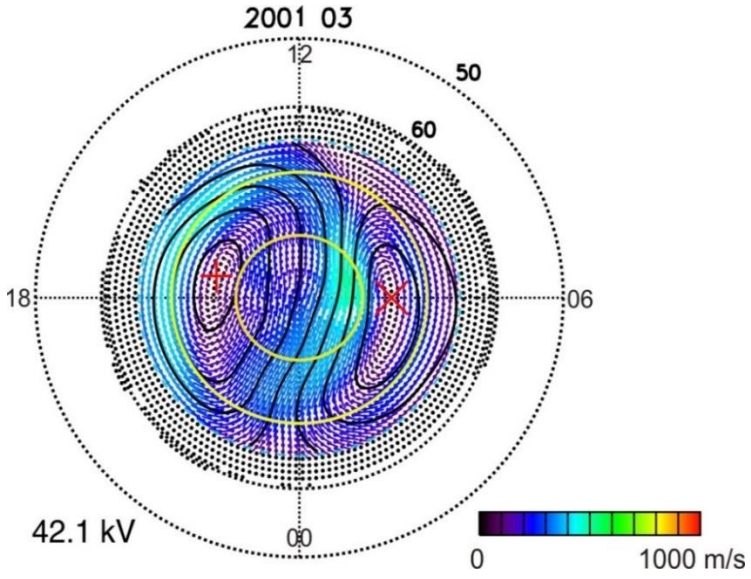

Figure 2.7: Convection pattern obtained by the SCHA technique applied to the March 2001 data, as described in the text. Contours of the potential are 6 kV apart.

In the work presented in this Thesis, monthly-averaging of the grid velocity data has been done in a specific way, consistent with recent approach by Cousins and Shepherd (2010), although they considered averaging over short intervals. The procedure for creating the monthly averages was as follows:

Step 1. SuperDARN data were gridded over 2-minute intervals using the standard techniques and codes by Ruohoniemi and Baker (1998).

Step 2. Only "typical" measurements were selected, i.e. only those with the velocity magnitude in between 50 and 5000 m/s and the "error" in measurement (ACF fit uncertainty in a plot like that of Figure 2.5) of less than 150 m/s.

Step 3. All data were organized into an MLAT-MLT grid with grid size equivalent to 1° of magnetic latitude.

Step 4. At each grid point, the data were placed into bins according to the azimuth of the radar beams/direction of LOS velocity measurement. Azimuth bins were 10° wide spanning from -180° to 180° (following the descriptions of Pettigrew et al., 2010).

Step 5. The average velocity for each azimuthal bin was determined. Each grid point therefore had up to 36 velocities assigned to it.

Step 6. SCHA fit was performed to create a map from selected data.

CHAPTER 3

AVERAGED PLASMA FLOWS IN THE HIGH LATITUDE IONOSPHERE, NO IMF CONSIDERATION

In this Chapter, monthly-averaged SuperDARN convection patterns are investigated. The convection pattern "averaging" has been done in an unexpectedly simple way: we computed monthly average of the standard SuperDARN grid velocity at every grid point on the MLAT-MLT plane and then applied the SCHA technique by Fiori et al. (2010). To get an "averaged" convection pattern over long period of time, one can "average" the 2-min maps over the desired duration, for example over a day or a month. We think that simple "superposition" of individual SuperDARN 2-min maps is not the only way to infer the realistic averaged convection patterns. Here are our thoughts on why another approach needs to be tried.

The SuperDARN mapping of the high-latitude convection is traditionally performed by employing statistical models of the convection pattern parametrized by the IMF B_z and B_y components, as we described in Section 2.6. Technically, the fit of the SuperDARN gridded velocity data can be done without any preliminary model/input but the danger has always been in getting unphysical solutions that are difficult to monitor in a case of an automated mass data processing. Although the startup convection pattern in the SuperDARN potential fit technique alleviates the problem, it does not eliminate it entirely. Only significant data coverage can guarantee a reliable convection mapping. Mori and Koustov (2013) demonstrated that at least 200 points per map are required to notice that the inferred cross polar cap potential (CPCP), one of the main quantitative parameters characterizing the high-latitude convection pattern, does not show values close to the startup values given by the model. For a doubled number of available points (to 400-500) the pattern estimate is expected to be reasonably good although no real testing of the SuperDARN convection maps has been done so far. Unfortunately, having more than 400 points per SuperDARN map is not a frequent occasion, even with all currently operating SuperDARN radars in either of the hemispheres (Ghezelbash et al., 2014). The other weakness of the Potential Fit approach is setting zero potential at the Maynard-Heppner boundary whose location determination is often hardly justifiable. Thus, any alternative way of averaging SuperDARN data has an interest, at least as a first look at long-term trends in the data.

The SCHA approach by Fiori et al. (2010) does not rely on the statistical model and does not force the potential to be zero at the Maynard-Heppner boundary, as we described in Section 2.6. However, the method requires good data coverage over the solution grid considered; unphysical solutions of the numerical fit are often seen at the edges of the considered data grid. The unphysical solution of the fit in this approach is usually identified by visual inspection of the obtained maps, and poor maps are simply rejected. Some preliminary assessment of the maps can be automated (Fiori et al., 2014). Clearly, such an approach is cumbersome for a massive, statistical analysis of the patterns. However, in a case of dense SuperDARN coverage (in MLAT and MLT) which can be achieved by considering data over long periods of time, the success of the fit is more certain. The approach, proposed by us, thus has merit although it also has some weaknesses, first of all because it mixes up data for various IMF conditions, although the hope has always been that having extended data set would eliminate any specific bias.

Keeping in mind the above strong and weak sides of the SCHA analysis, a decision has been made to consider velocities averaged over one month of SuperDARN data. The time period of one month was selected because the SuperDARN data are traditionally stored as monthly data sets. In addition, as it turned out later, the monthly data sets have more or less uniform representations of the solar wind and IMF conditions, from one month to another and within one year, so that conclusions based on monthly-averaged data sets do not have a serious bias in terms of the external drivers of the ionospheric convection.

To create a data base for fitting, monthly-median gridded velocities were computed for every grid point of observations, 1° of MLAT and equivalent (spatially) region of MLT. Because of the long periods (28-30 days) considered, the grid velocity was available in most of grid points between 65° and 90° of magnetic latitude and in most of MLT sectors (some points were available even at lower latitudes so that the cap size was actually set to 60°). With good data coverage, SCHA fits are reliable over the entire map with exception of the lowest latitudes. For this reason, obtained convection velocities at latitudes below 70° will not be discussed here. Certainly, such highly-averaged data are only suitable for investigation of large-scale and long-term trends in variations of the convection pattern as microstructures in flows and effects of fast changes due to varying external conditions are smoothed out.

As have been discussed in Section 1.3, the high-latitude convection pattern depends on the IMF magnitude and direction (e.g., statistical models by Heppner and Maynard, 1987; Rich and

Hairston, 1994; Papitashvili and Rich, 2002; Haalland et al., 2007 to name a few beyond the SuperDARN-based models). Unfortunately, it has not been established yet which parameter (or combination of parameters) characterizes the convection pattern completely although various studies converge to the notion that the IMF (magnitude and orientation) is one the major factor. Before undertaking massive data processing, we evaluated variability of the IMF conditions from one month to another to be certain that the data are more or less uniform in terms of background conditions. An example of such analysis is given in the next section.

Some results reported in this Chapter, in their very preliminary form, were presented by the author at the International SuperDARN workshop (Koustov et al., 2013). The standard SCHA convection maps were created by Dr. R. Fiori, NRCAN, Ottawa. The author performed assessment and analysis of the inferred convection maps.

3.1 Typical IMF conditions for month-long SuperDARN data sets

In this Section, data for 11 consecutive years (2001-2011, 132 months) of SuperDARN operation in the northern hemisphere are considered. The data cover periods of the solar maximum (2000-2002, solar cycle 23) and minimum (2007-2009, solar cycle 24) in the solar activity. One would expect that, over such a long period, the IMF components and intensity as well as solar wind parameters would vary significantly, and the external drivers of the high-latitude convection would vary strongly as well. This is certainly the case, but it turns out that when one compares data for consecutive months, even for many months within one year, the differences in the magnitude of external drivers of the ionospheric flows are not very drastic.

Figure 3.1 gives examples of the IMF B_z-B_y components distributions for 3 months of 2001 (a year during the solar cycle maximum) and 2007 (a year during the solar cycle minimum). The plots correspond to three seasons. One common feature for all the plots is a "round", almost circular/isotropic, shape of the distributions. For 2007 (2001), most of the data are within +/- 5 nT (+/- 10 nT). The difference in the "spread" of the distributions is expected; the interesting and important fact is the sizes of the point clouds differ by less than 2 times. Certainly, each month has some preferential combinations of the IMF components identifiable as red-colored areas ("islands") of enhanced occurrence. For all the plots, the B_z^- and B_z^+ conditions occur with roughly

the same probability. In terms of the B_y, there is more of a bias for some months. For example, for March of 2001 and 2007, the B_y^+ conditions were more frequent.

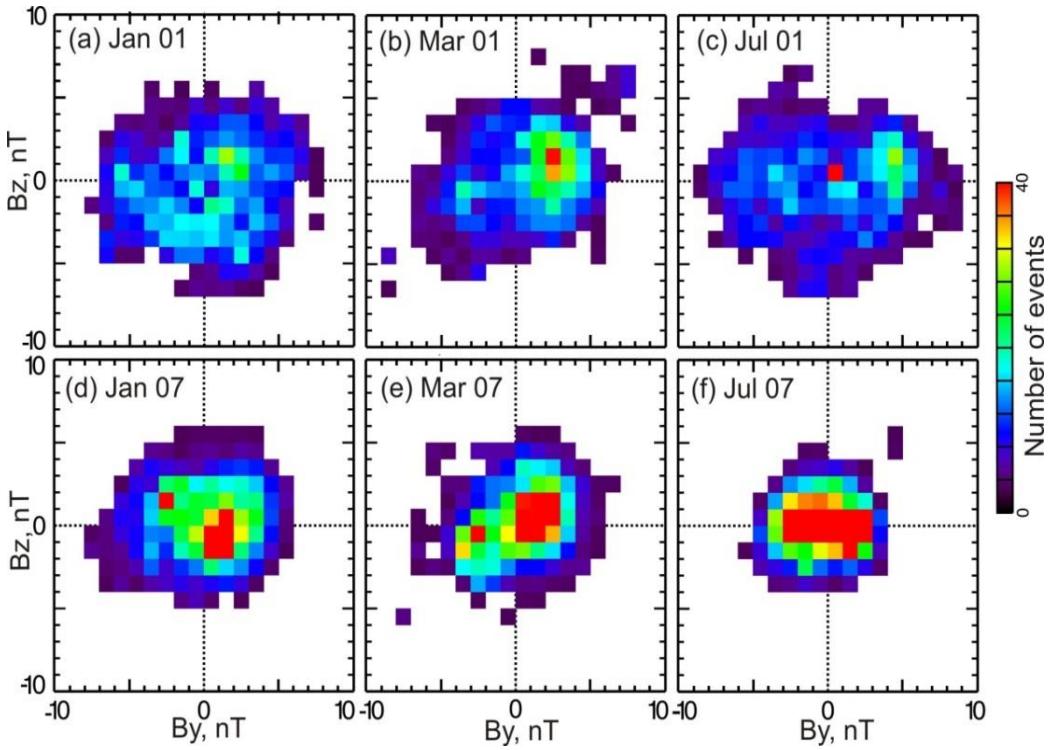

Figure 3.1: Contour plots for monthly occurrence of the IMF B_z and B_y components in 2001 (period of high solar activity) and 2007 (period of low solar activity). January, March and July plots represent winter, equinox and summer conditions, respectively. The scale is the same for all the plots.

We can conclude that although there are some differences between IMF component distributions for individual months, the monthly sets are not drastically different. These differences should be considered as minor ones as the goal of our investigation is the long-term trends based on many months and years of the data so that minor biases for specific months would not repeat again and again, from one year to another. In addition, later on (Chapter 4), we perform analysis by considering SuperDARN data sets constrained to certain bins of the IMF B_z and B_y. As expected, results obtained with our two ways of treating the data, with and without the IMF consideration, did not show fundamental qualitative difference, and this gives us additional confidence in the merit of our approach.

3.2 Shape of monthly-averaged convection patterns

For the reader's convenience, Figure 3.2 repeats the convection pattern obtained by applying the SCHA technique to the March 2001 SuperDARN gridded data and given in Figure 2.7. One can notice a "ragged" edge of the data coverage at MLAT~ 65°. This is because of often missed data at lowest ranges of SuperDARN observations.

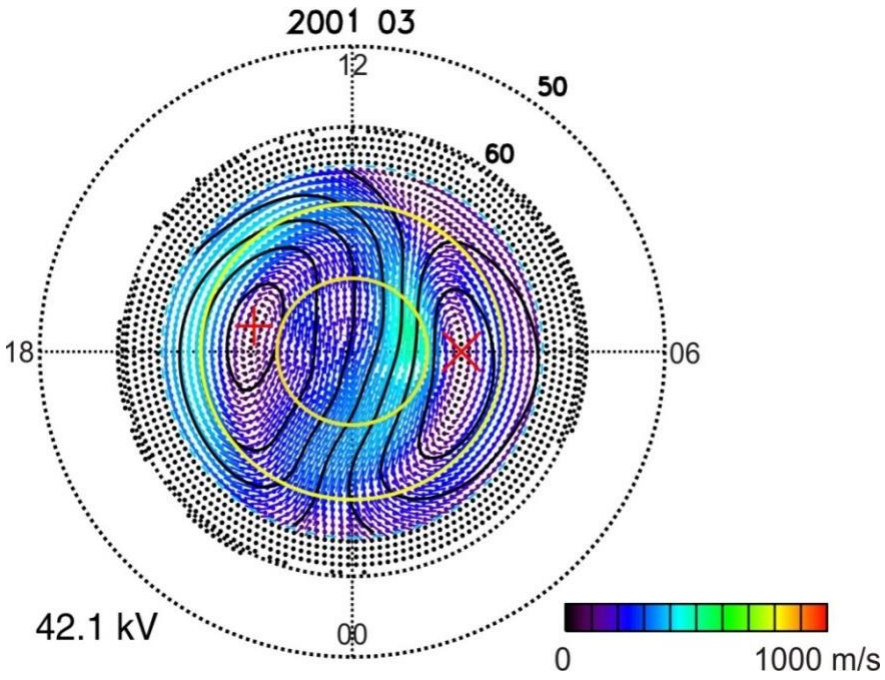

Figure 3.2: Example of the convection map obtained by considering one full month of Super-DARN grid velocity data (March 2001). The SCHA technique of Fiori et al. (2010) was used.

The contours of equal potential indicate that the pattern has a 2-cell shape with centers of the cell located at MLAT~ 77° and MLT=06 and 17. The plasma flows are anti-sunward within the central polar cap (roughly, along the non-midnight meridian). We note that a 2-celled pattern is highly expected for conditions with not frequent occurrence of the B_z^+ dominated periods. Here we have it when all the IMF conditions are considered. Two major areas of enhanced flows are evident: one for the return plasma flow toward noon during the afternoon hours at MLAT=70° and the other one is the flow over the North Pole at near noon hours and MLAT>80°. The other feature

to report is clearly identifiable, by the very low magnitude of the flow velocity, the convection reversal boundary at MLAT=77° and MLT =16-20 and MLT=05-08.

Plots similar to Figure 3.2 have been produced for all 132 months of SuperDARN operation (2001-2011). Some of them did not look as good as that of Figure 3.2 because the data coverage, especially summer time, was not as even and widespread. This is expected. Ghezelbash et al. (2014) argued that absence of the radar data in the Russian sector of the Arctic does not allow achieving truly global coverage, even on a monthly basis. In the following three sections we present our assessment of the patterns obtained.

3.3 Convection reversal boundary of monthly-averaged patterns

Convection reversal boundary (CRB) is an important parameter of the convection pattern, see Section 1.4.3. Here we investigate statistically the location of the CRB in various MLT sectors and discuss its seasonal and solar cycle trends for the dawn and dusk sectors. The CRB location was determined by considering velocity data at various latitudes (with the step of 1°) binned over one hour periods.

To derive the CRB location, the azimuthal (duskward) component of the velocity component was considered. It will be referred to as the V_φ component. The idea here is that V_φ changes its sign as one considers a specific MLT line, say 18:00 MLT, and look at the velocities starting from lowest latitudes all the way to the Pole, Figure 3.3. For a 2-celled convection pattern and, for example, for 18:00 MLT, the flow would be toward the noon at low latitudes (negative V_φ) and away from noon (positive V_φ) at high latitudes of >80°. This is exactly what is seen in Figure 3.3. In the following, the CRB location was found by finding the MLAT of the intersection of the curve and X axis (i.e., where V_φ is zero). The CRB location for the plot of Figure 3.3 is at about MLAT=77°. We note that for the MLT sectors away from the dusk and dawn line, the curve often assumes low values in a broad range of MLATs so that, although the crossing is identifiable, it is not very valuable as a parameter because of a large uncertainty in a possible location.

One interesting and important characteristic of the CRB is its latitudinal location in various MLT sectors. In our first effort, we attempted to assess the CRB locations versus MLT for some specific months. The months with good SCHA fits, covering all three seasons and periods of the

solar cycle maximum and minimum, were selected. The analysis for several months, representing winter, summer and equinox, are presented in Figure 3.4.

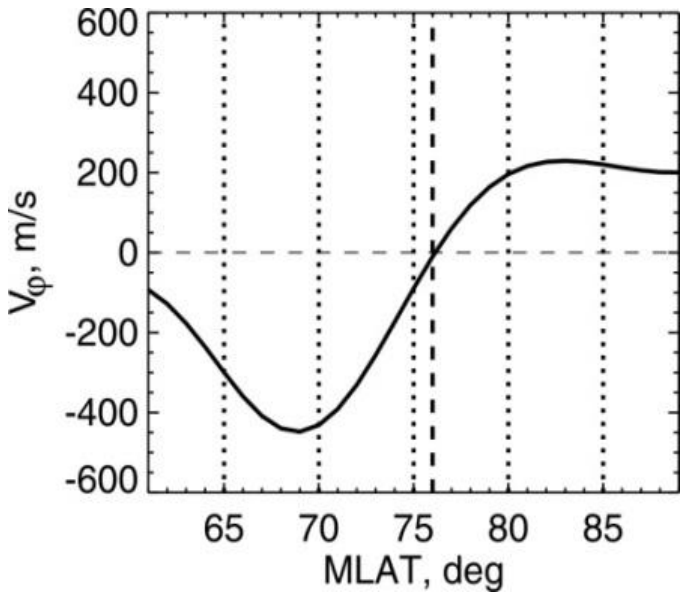

Figure 3.3: Velocity V_φ component versus MLAT at 18 MLT for December 2001.

The three plots in the top row are for 2001, the year of high solar activity. The equinoctial data in Figure 3.4a show fairly symmetric location of the CRB at MLAT=75° -76°. The CRB latitude is lower in the midnight sector, during early morning hours. For summer conditions, Figure 3.4b, the typical latitudes are clearly larger, 77°-79°. In the early afternoon, MLATs are even above 80°. Overall, the curve on the duskside seems to be located closer to the line of MLAT=80° as compared to the curve in the dawn sector. Again, latitudes of the CRB location decreases towards midnight during early morning hours. For winter conditions, Figure 3.4c, the CRB seems to be located in between its equinox and summer positions.

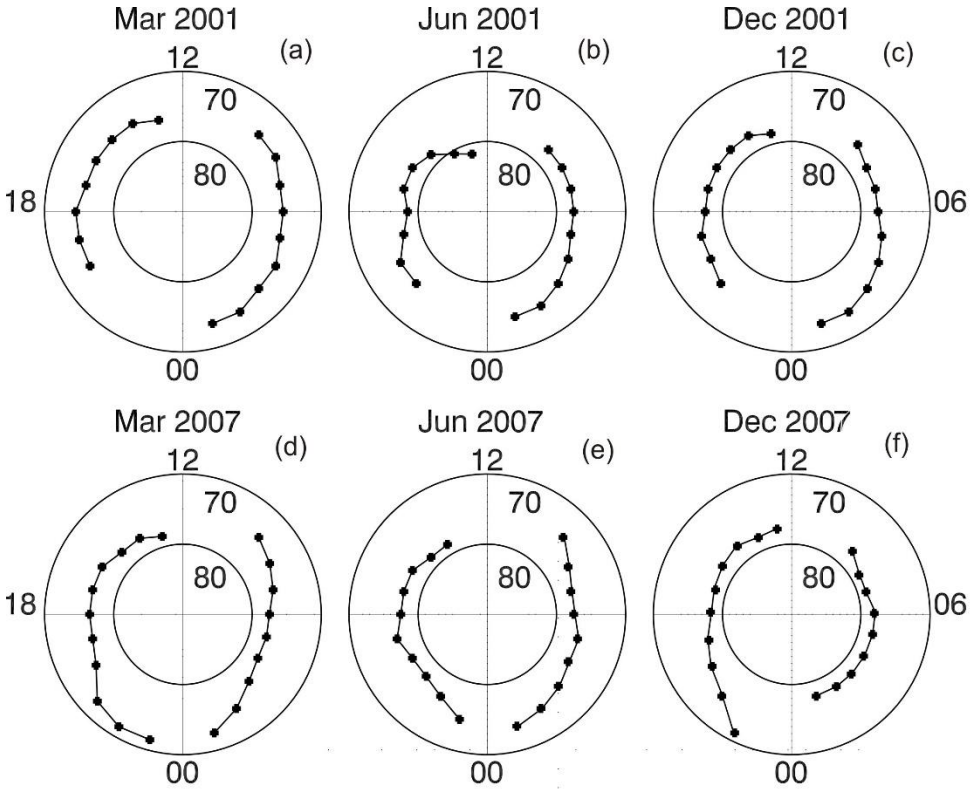

Figure 3.4: Convection reversal boundary location for March, June and December 2001 (top row) and 2007 (bottom row).

The three plots in the bottom row are for 2007, the year of low solar activity. The plots look similar to those at the top row with one clear feature – they are located at higher magnetic latitudes for almost all time sectors. For example, for the equinoctial data of Figure 3.4d, the typical latitudes are 77° -79° versus 75° -76° for Figure 3.4a. The other feature of the 2007 data is a stronger shrinking of the CRB "belt" toward higher latitudes on the dawnside as compared to the duskside, Figure 3.4d,f.

Data of Figure 3.4 illustrate only some variability in the CRB location. Considering the entire data set, it was difficult to infer a clear pattern of this variability by simply looking at the data for individual months. To establish the seasonal and solar cycle variations in the location of the CRB in a more systematic way, we investigated all the monthly maps available for 2001-2011, i.e. by considering the period from the solar maximum (2001) to the solar minimum (2007-2008) and going back toward the next solar maximum (~2011). The CRB location was characterized by finding the CRB latitudes for 05, 06, 07 MLT and averaging them to represent the dawn sector

data and 17, 18, 19 MLT and averaging them to represent the dusk sector data. Every month of the year was considered.

Figure 3.5 presents results of this analysis. Figure 3.5a shows variation of the Sunspot Number (SN) over the period considered to illustrate, in a more quantitative way, how the solar activity progressed. We show here the raw data (noise-like thin lines connecting actual points) taken from NASA website (http://www.ngdc.noaa.gov/stp/solar/solardataservices.html) and smoothed values obtained by averaging raw data for each month (red dots connected by thick line).

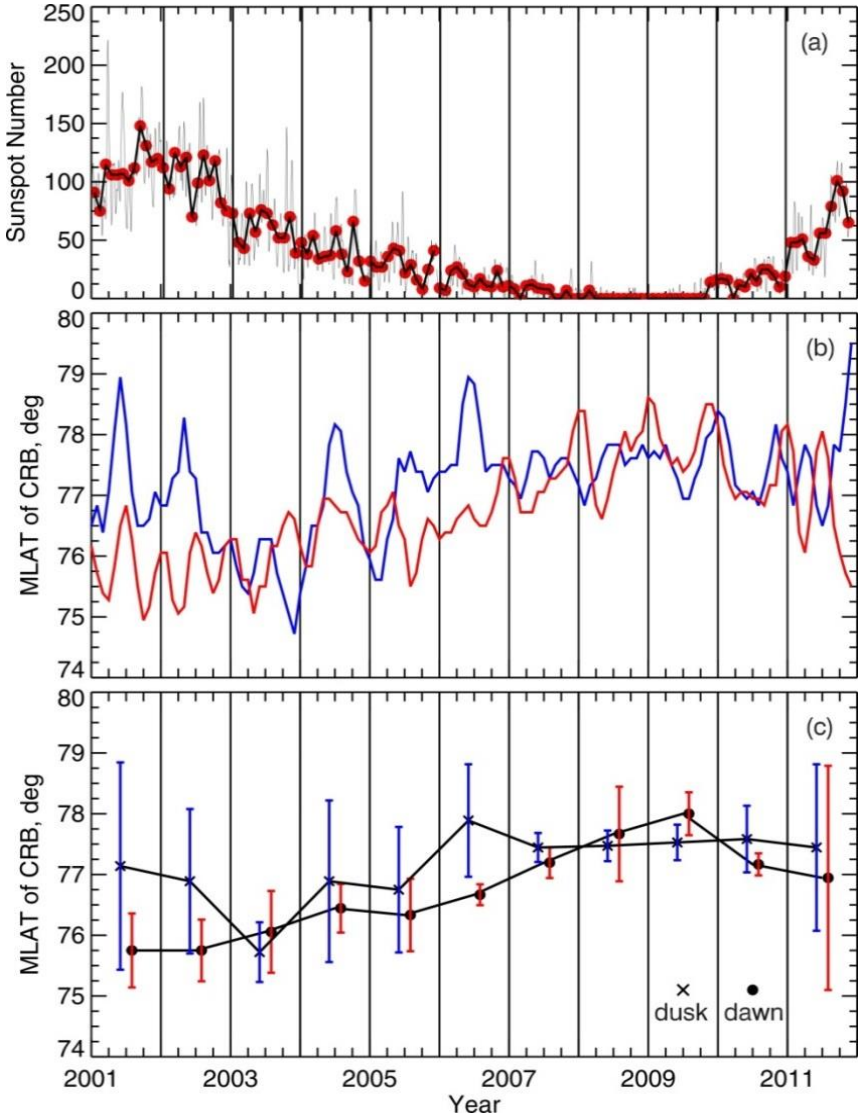

Figure 3.5: Plot of (a) the Sunspot Number versus time, (b) CRB latitude for the dawn (red line) and dusk (blue line) sectors versus time, and (c) CRB location, averaged over one year periods, for the dawn (red line) and dusk (blue line) sectors as a function of time.

One can see that the SN went down from typical values of ~ 150 to almost zero in 2008-2009. The true "recovery" of the SN has not actually happened until now (early 2015). The expected time for the SN maximum is 2012 (2001+11=2012) but we see that the SN during 2012 did not actually exceed its values for 2011.

Figure 3.5b shows the CRB latitude as a function of time for the dawn and dusk sectors, red and blue lines respectively. One can notice that for the first half of the period (high solar activity), the blue line is typically located above the red line indicating that the CRB is at higher latitudes in the dusk sector. During the second half of the period considered, low solar activity, there is no systematic difference between the red and blue lines.

Perhaps a better way of judging long-term trends is to consider Figure 3.5c where the data on the CRB latitude from Figure 3.5b were averaged over each year of measurement. Vertical bars in this panel indicate the standard deviation of the data within each year. One can see that the blue curve is above the red curve for 2001, 2002 and 2007. For other years, the differences are less obvious, especially as the curves are within the range of the standard deviations.

In terms of the season, the plot does not indicate a clear tendency for the shifts in the CRB location. The 2001 data show that the latitudes are higher during summer time as compared to winter, both at dawn and dusk. However, just two years later, in 2003, no shift is noticeable. Higher latitudes for the summer CRB location are seen for the next year data, 2004, and for 2007. This is not a stable feature, however; moreover, for 2009/2010, the highest latitudes were for the winter time.

The data of Figure 3.5c indicate that the latitudes of the CRB location are highest during solar cycle minimum and lowest during the solar cycle maximum. The effect of the solar cycle is more obvious for the dawn data.

3.4 "Throat" location inferred from analysis of the zonal velocity data

The "throat" is a region of sharp reversal of the plasma flow in dayside and it is another prominent feature of the high-latitude convection patterns. This feature is easily identifiable on most convection maps, especially when contours of equal potential are placed on a top of vectors of the plasma flow, see for example the map in Figure 3.2. Although the throat location depends strongly on the IMF B_y component (e.g., Birch, 1972; Haaland et al., 2007), one can expect that

averaging over a long period of observations, corresponding to both positive and negative IMF B_y, would cancel the expected shifts and the pattern would be "symmetric" with respect to the noon-midnight line. In this Section we attempt to investigate this issue by considering the maps for 2001-2011.

Figure 3.6 shows the zonal component of the plasma flow V_φ at latitudes of 72° (auroral zone) and 82° (polar cap) in a form of a contour plot. The straight vertical line corresponds to the noon-midnight meridian, the expected location of the throat as explained above. The MLT time location of the throat's center is enhanced by the ragged black line; it separates two greenish colors of the contours.

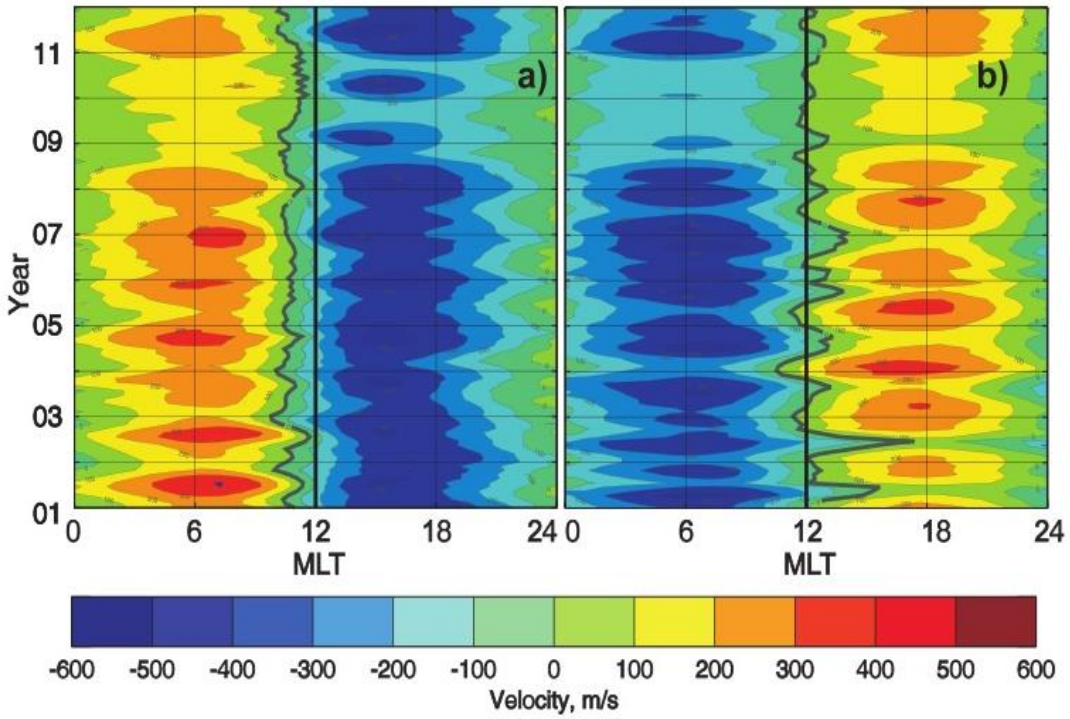

Figure 3.6: Contour plot of the zonal component of the convection velocity V_φ at (a) MLAT=72° and (b) MLAT=82°. Black line is a border line between positive and negative zonal velocities.

One clear effect is that the throat is observed 1-2 hours prior to the noon for the auroral zone data while much closer to the noon and even ~1-2 hours in the afternoon for some months of the polar cap data. This effect means that the center line of the throat is rotated off the non-midnight meridian. The effect is also recognizable by simple eye inspection of patterns for a specific month, for example in Figure 3.2. The MLT location of the throat varies slightly over a season (within each year) but the systematic variations are only recognizable for the years of the

solar cycle maximum when it is getting closer to (away from) noon during summer (winter). Visual inspection of the Figure 3.6 also indicates that the throat location does not change much over the solar cycle if averaged over the year data are considered.

3.5 Magnitude of the flow in the polar cap and in the auroral zone

Data presented in Figure 3.6 show some regularity in occurrence of regions with enhanced positive (red) and negative (blue) velocity, both in the auroral zone and in the polar cap. The effect disappears toward the end of the period considered. In this section we investigate these features with a focus on the magnitudes of the plasma flow, not only on its zonal component.

Before proceeding to the main topic of this section, a comment on the data presented in Figure 3.6. For the auroral zone observations, Figure 3.6a, at the beginning, 2001-2004, summer enhancements of the positive velocity are evident but later on the maxima shifted to winter. For the polar cap latitudes, Figure 3.6b, the positive velocity maxima occur during winter (in contrast to summer maxima in the auroral zone) in 2001-2004 and they shift toward summer periods later on (again, in contrast with the auroral zone data). Another interesting aspect of the data is that velocities at dawn and dusk are not quite the same in magnitude. For example, consider 2011 data for MLAT=72°. Maximum velocities at dawn are about 200 m/s while they are about 300 m/s at dusk. This dawn-dusk asymmetry can be seen during other periods as well. For the polar cap latitudes of MLAT=82°, the dawn-dusk contrast is in opposite way, i.e. dawn velocities are larger in magnitude than the dusk velocities. Figure 3.6 thus indicates that the velocities vary strongly with both MLAT and MLT.

Figure 3.7 presents the plasma flow magnitude versus magnetic latitude for the entire considered period. The four plots correspond to different MLT sectors: (a) noon (MLT=12), (b) midnight (MLT=00), (c) dawn (MLT=06) and (d) dusk (MLT=18). The plots show existence of regions with strongly enhanced flows, by a factor of 2. Maximum values are ~ 400 m/s and achieved in very limited areas. There are some similarities and some differences between the locations of the fastest flows on the plots. Comparing noon and midnight data of Figure 3.7a, b, the fastest flows with velocities above 400 m/s are seen for latitudes 75°-80° in both sectors, but

300-m/s contours are shifted toward smaller latitudes (auroral zone) near noon and to larger latitudes (polar cap) near midnight.

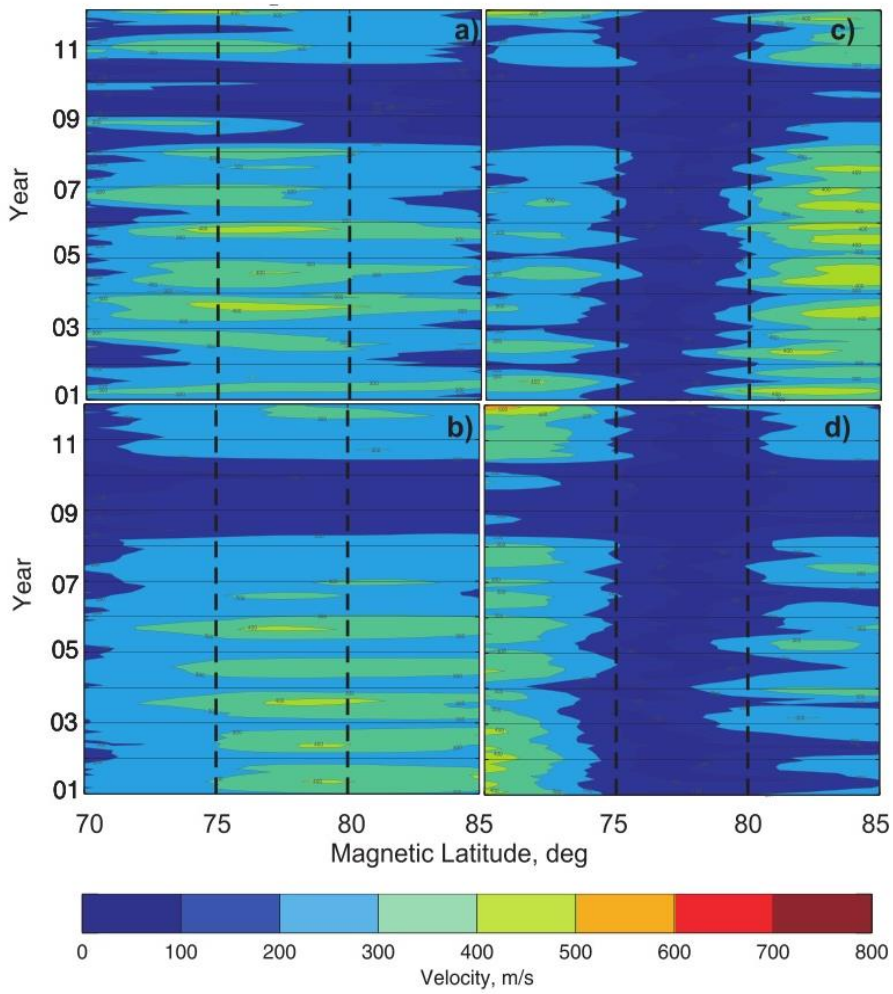

Figure 3.7: Contour plots for the plasma velocity magnitude on "month-MLAT" plane for SuperDARN observations in 2001-2011. The SCHA technique has been applied to monthly-averaged grid velocity data as described in Section 2.6. Four MLT sectors are considered. The dark blue areas of slow flow in panels (b) and (d) correspond roughly to the CRB location (MLAT~77°).

We note that the above shifts are inconsistent with the more poleward location of the auroral oval on the dayside as compared to the nightside. The 2008-2009 data show smaller velocities all across the plots although relative variations of the velocity versus MLAT (diurnal variation) is consistent with the data for other years. We were not able to identify the reason for such a velocity decrease for these specific years.

In the midnight sector, Figure 3.7b, enhanced velocities clearly occur during summer time for 2001-2005. A Similar, but less consistent, effect is seen for near noon data of Figure 3.7a although for this sector, the maxima eventually shift toward winter time in 2008-2011.

The dawn-dusk data of Figures 3.7c and 3.7d also show some similarities and differences. One obvious conclusion from a comparison of the data is that regions of the lowest velocities (dark blue) are consistently observed at MLAT~77°. These are the latitudes where convection reverses its sign which leads to low magnitude of the total vector. These data are thus (expectedly) consistent with the analysis of the convection reversal boundary location performed in Section 3.3 where the reversal was determined by analysing the zonal component of the convection velocity vector. We can even notice by eye as the low velocity regions shift toward larger latitudes at the solar cycle minimum period (compare with Figure 3.5).

Peculiar difference between the dawn and dusk data is that while the dawn velocities maximise in the polar cap, MLAT>80°, the dusk velocities maximise in the auroral zone, MLAT <75°. In addition, dawnside velocities seem to be larger than the duskside velocities. We have to note, however, that the dusk velocities are even larger at lower MLATs of <70° but these data are not shown here as there is no confidence to what extent the velocity increase at these latitudes is affected by the numerical solution of the SCHA fits.

3.6 Discussion of obtained results

Many of the reported above features in the convection patterns are consistent with what has been known for years on a basis of convection data investigated either for specific events or merged into a single block that was afterward sorted according to the IMF B_z and B_y. The goal of the undertaken effort was to reveal any long-term trends in the high-latitude convection by making monthly blocks of the data and assuming that all possible external driving conditions occur roughly with the same frequency over a month and that the driving conditions change only little, if any, from month to month. We showed that, over an entire solar cycle, these little changes accumulate and end up with statistically larger possible IMFs during the solar cycle maximum. One would generally expect that the “typical” flow velocities (electric fields) would be stronger at the solar cycle maximum.

One of the surprising conclusions one can make from the data presented is that the anticipated effect of a strong increase in the high-latitude plasma velocities/electric fields magnitude toward the solar cycle maximum does exist but it is not very pronounced. Nightside data of Figure 3.7b are perhaps the only plot where we clearly see that maximum velocities do go down after 2005, i.e. toward the solar cycle minimum. Data for the noon sector are less convincing. The dawn and dusk data have some evidence for the effect at the auroral zone latitudes and none at the polar cap latitudes.

Reasons for the not strong increase in the plasma flow velocity at the solar cycle maximum are not clear. Previous SuperDARN publications did show that the LOS velocity increases with enhancement of the external drivers characterized, for example, by the PCN magnetic index, IMF reconnection field etc., as reviewed in Section 1.5. These clear responses, however, were found for observations on the dayside where the effects of the merging rate variations are expected to be stronger. It is not clear whether this is true for observations in other time sectors. It is well established that the effects of the IMF B_z transitions in the high latitude convection is hard to recognize on the nightside (e.g., Fiori et al., 2013). Since the SuperDARN convection pattern is determined by involving vectors in as many as possible time sectors and magnetic latitudes, the effect of the external driver change might be washed out in a statistical analysis such as ours.

Being puzzled by this uncertainty, we decided to find out whether the LOS velocity of an individual SuperDARN radar shows long-terms trends. For a test, we selected the RKN radar that is capable of detecting F region echoes through ½-hop mode at latitudes > 80°. We computed the hourly medians of the observed velocity in specific beams and specific range gates (more details on the method of calculations one can find in Chapter 5). To be consistent with the paper by Koustov et al. (2013), and on a practical side to extend the period of their study, we selected central beams of the radar 6, 7 and 8 and two sets of range gates, 15-19 and 27-29. The first set of ranges corresponds to minimum ranges where echoes are still coming from the F region (we want to avoid any E region echoes whose velocity might not be reflecting the $\vec{E} \times \vec{B}$ plasma drifts). The second set of ranges is at the far edge of the echo detection zone by the RKN radar.

Figure 3.8 shows the results of our analysis. The left panel clearly shows that the RKN median velocity magnitude increases steady from 2007 to 2013, i.e. from the years of the solar cycle minimum to the years of the solar cycle maximum. This is in full agreement with the above expectation.

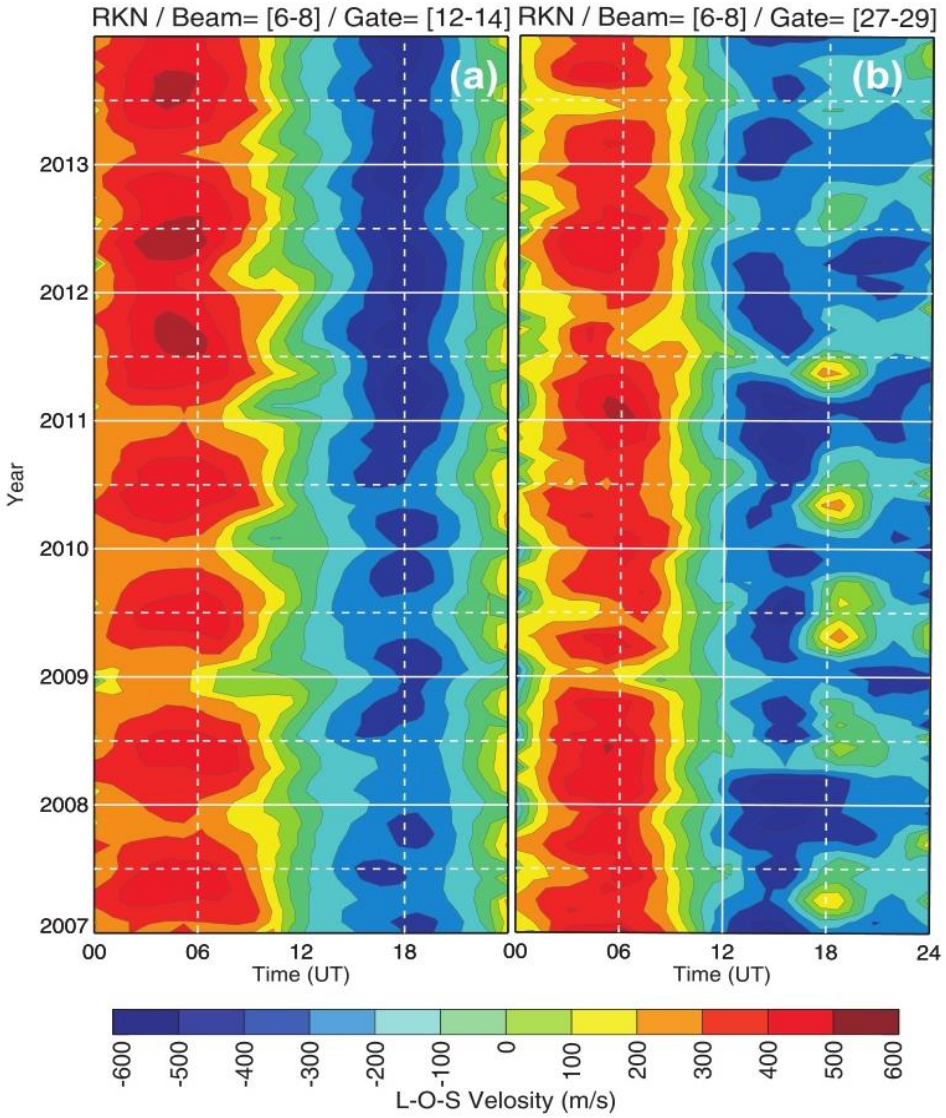

Figure 3.8: Variation of the RKN velocity (hourly medians) with UT time in beams 6-8 and radar gates (a) 12-15 and (b) 27-29.

The data of the right panel, however, do not show the effect. Here the maximum velocity magnitudes are smaller for observations in the midnight sector (for the RKN radar, midnight is roughly at 06:00 UT) and they do not show a consistent pattern of a change. For near noon (~18:00 UT), the velocity magnitude is not only small but even changes the sign during summer periods. This change in the velocity polarity closer to summer time was associated by Koustov et al. (2013) with the effect of the sunward flows for IMFB_z^+.

The results of this analysis do not allow us to make a definitive conclusion whether the SuperDARN LOS velocity "responds" to the external driver/solar activity increase. In this view, it would be interesting to perform more comprehensive investigation of how strong is the correlation between SuperDARN LOS velocity for a specific radar and external drivers in various time sectors. An attempt to investigate some aspects of this issue with the RKN SuperDARN radar has been undertaken in the next Chapters 4 and 5, but more comprehensive study is needed.

Data presented in Figure 3.8 point at potential concern with respect to the approach undertaken in this Chapter. We see that near noon high-latitude plasma flows can be actually sunward, presumably for conditions with the IMF B_z^+-dominating component. The effect seems to be stronger during the solar cycle minimum. Conclusion on the existence of the effect for other SuperDARN radars requires further work. Saskatoon radar data would be interesting to try since this radar has been in operation since 1994. This is a new project that will be listed later in Chapter 6. The other option to alleviate the B_z^+ effect is to consider only periods with B_z^- conditions. This work has been partially done with the author's participation and the results will be reported in the next Chapter.

The other research target of this Chapter is the seasonal variations of the convection pattern. The computer modeling predicts steady currents for different seasons, as the conductivity changes with season one would expect seasonal variation in the electric field, as the current density can be represented in a simplified form known as Ohm's law

$$\vec{J} = \sigma \vec{E}, \tag{3.1}$$

where $\vec{E}$ is the electric field and σ is the conductivity. In other words, high-latitude velocities are expected to be stronger winter time if the FACs are not changing drastically with season because of a much larger conductance of the summer, sunlit ionosphere. In this respect, our results are in total disagreement with the expectation. Data of Figures 3.6-3.8 consistently show that during high solar activity periods, summer velocities are larger, at least at MLAT>75°. The effect is very well seen in LOS nighttime data of the RKN radar, Figure 3.8a. Preliminary indication of the effect has been given by Fiori et al. (2009).

Although we cannot explain the above effect in simple terms, we would like to make one comment, from the observational point of view. While comparing SuperDARN velocities during winter and summer time, we tacitly assume that the observational conditions are the same and the radars continuously monitor the ionosphere irrespective of its characteristics. The reality is that it

is much more difficult to detect HF coherent echoes in summer time, see for example recent papers by Ghezelbash et al. (2014, 2015) where it was reported that occurrence of RKN echoes drops by a factor of 2 toward summer time. One of the major reasons for this is believed to be the effect of smoothing out the ionospheric electron density gradients by sunlight and making difficult launching the GD plasma instability. Another possible effect is enhanced radio wave attenuation in the D region during summer. These two factors imply that to detect an echo with an instrument of a fixed sensitivity, stronger electron density perturbations are required. This can be achieved through enhanced electric fields. Indeed, Ghezelbash et al. (2014) reported a clear correlation of RKN echo occurrence during near noon summer hours. Thus one might expect that HF echoes detected by coherent radar during summer would correspond to regions with enhanced electric field (as compared to winter conditions) so that the radars would report statistically larger average velocities that would be translated into faster overall flows within a global convection pattern. Certainly, it is hard to prove how widespread the effect is, but it might be real.

Another interesting result of this Chapter is that the throat was located at pre-noon hours at latitudes of the auroral zone and almost at noon in the polar cap. While averaging convection patterns over a month, one would think that afternoon excursions of the throat for negative B_y would be entirely compensated with its pre-noon locations for positive B_y so that the resultant location would be around noon. This is not the case for the 11 years of observations considered. This probably means that one cannot interpret the B_y effect in the convection pattern by simply considering a dawn-dusk shift of the merging region at the magnetopause. On a micro-scale, we reported a possibility of stronger displacement of the throat region toward (away) the noon-midnight meridian, and even shift to the afternoon hours, at large magnetic latitudes (polar cap), Figure 3.6b. On the other hand, at the auroral zone latitudes, the throat region is consistently located at 1-2 hours prior to the magnetic noon. No obvious trend is seen here in terms of season. De la Beujardiere et al. (1991) reported that their Sondrestrom incoherent scatter radar data showed stronger throat deviation from the noon location for summer.

Our results on the CRB location agree, roughly, with the ones reported by Bristow and Spaleta (2013) who considered the Potential FIT output of the SuperDARN measurements for multiple events and only B_z^- conditions. They made an extensive investigation of the CRB location depending on the solar wind and IMF parameters, as well as magnetic index SYM-H, characterizing occurrence of magnetic storms in the near-Earth's environment. They also presented

a diagram of the CRB location versus MLT, obtained by combining all the data they selected into one data set, their Figure 7. We compare their data with our plot of Figure 3.4a in Figure 3.9.

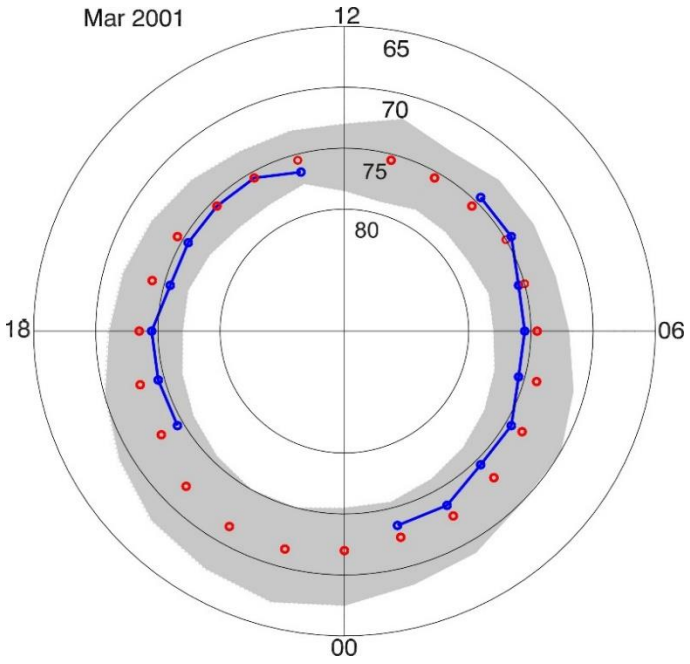

Figure 3.9: Convection reversal boundary location for March 2001 as reported in Figure 3.4 and the average boundary location according to Bristow and Spaleta (2013), red circles and grey belt reflecting +/- one standard deviation from the average location.

The agreement is remarkably good, especially in view that the approaches to the analysis are completely different. Certainly, the agreement with the other plots of our Figure 3.4 is not as good, but still the CRB locations are not very far off. This suggests that the analysis we undertook does give reasonable estimates of the CRB locations, and the inferred trends are very likely real.

Our data of Figure 3.9 show one interesting trend: the dawn CRB is usually located at lower magnetic latitude as compared to the dusk CRB. This is consistent with the report by de la Beaujardiere et al. (1991) who considered data of the Sondrestrom incoherent scatter radar. These authors also reported on seasonal changes in the CRB location that were different for the dawn and dusk cells. The dusk (dawn) cell CRB is located at lower latitude winter (summer) time. Our data are confusing. For the solar cycle maximum period, our dusk data are consistent with their result, but not the dawn data. On the other hand, for the low solar activity period, the summer CRB is

usually located at smaller magnetic latitude, consistent with their result. Our dusk data for this period are inconsistent with their result.

3.7 Summary

In this Chapter we analyzed SuperDARN velocity data collected in 2001-2011 and processed with the SCHA approach into maps of the high-latitude convection. Monthly-averaged data sets for gridded velocity have been considered. Inferred convection patterns have been assessed and three features of the patterns, the CRB, the dayside throat and MLT/MLATs for the occurrence of maximum flow velocity were investigated in detail. We found several interesting features.

1) For the dusk and dawn of winter time, the CRB is typically located at MLATs =76° -77°. The latitudes are smaller (larger) by ~1° - 2° on the dayside (nightside).

2) The latitude of the dawn/dusk CRB location changes within the solar cycle being ~1° higher during the solar minimum period.

3) The dayside throat is located 1-2 hours prior to the magnetic noon at latitudes of the auroral oval but much closer to the noon at the polar cap latitudes. No clear seasonal and solar cycle effect for the throat MLT time has been identified although displacements to the afternoon sector can occur at the polar cap latitudes summer time.

4) For flows in the midnight and noon sectors and during the years of high solar activity, the flows are faster (slower) in summer (winter) time. The effect is clearer on the nightside. For the solar cycle minimum, no clear seasonal variation in the velocity magnitude was identified.

5) The flows along the midnight-noon meridian are stronger at lower magnetic latitudes on the dayside as compared to nightside.

6) For the flows in the dusk and dawn sectors, there is a strong asymmetry in the velocity magnitudes for the polar cap latitudes with the dawn flows being consistently faster by ~100-200 m/s than the dusk flows.

7) The velocity of plasma flow in the noon and dusk sectors is faster during high solar activity.

CHAPTER 4

AVERAGED PLASMA FLOWS IN THE HIGH-LATITUDE IONOSPHERE. IMF INTENSITY CONSIDERATION

As discussed in Chapter 3, a concern can be raised that merging SuperDARN data over monthly periods might introduce a bias toward a specific configuration of the IMF. We have done analysis of the monthly-averaged convection patterns for some specific IMF bins. In this Chapter we report on features of the convection patterns for six bins of the IMF. The bins were established according to the IMF transverse component $B_t^{\pm} = B_z/|B_Z|\sqrt{B_z^2 + B_y^2}$ with B_z sign taken into consideration. The IMF bins selected were as follows: $B_t^- = (-12 \text{ to } -6)$ nT with the center value of -9 nT; $B_t^- = (-6 \text{ to } -4)$ nT with the center value of -5 nT, $B_t^- = (-4 \text{ to } 0)$ nT with the center value of -2 nT and similar 3 bins for positive IMF B_t^+. These six IMF bins were selected for three reasons. First of all, these bins would allow us to include almost all the SuperDARN data available. Secondly, regarding the specific values chosen, these bins are the limits of the statistical convection model by Ruohoniemi and Greenwald (1996), often referred to as the RG96 model. The RG96 model has been traditionally (at least for 15 years) used for SuperDARN data processing and resulted in multitude of publications. Finally, while deriving the maps, we had always a chance to assess by how much the SCHA maps are different from the Potential FIT-based maps. We note that comprehensive analysis of differences between the RG96 model and our data does not make much of a sense because a new, more elaborate statistical convection model has been suggested for future use (Cousins and Shepherd, 2010). This new model has only been implemented recently

so we have not had chance to use it. We should note that splitting the SuperDARN data according to B_z and B_t sign reduces the amount of measurements available for each convection map. This is especially critical for the bins with large B_t. The consequence of having these shortened data sets is, not surprisingly, that the quality of the fit was not always good, especially at the lowest latitudes.

In this Chapter we first compare velocities derived for some B_t bins with those of Chapter 3 where data were processed without IMF consideration. We then focus on salient features of the convection patterns with special focus on two magnetic latitudes, 72° and 82°, corresponding to the auroral zone and polar cap, respectively. We explored magnetic local time, seasonal and solar cycle dependencies.

Some data reported in this Chapter, in their very preliminary form, were presented by the author at the International SuperDARN workshop (Koustov et al., 2013). The standard SCHA convection maps were created by Dr. R. Fiori, NRCAN, Ottawa. The author participated in assessment and analysis of the inferred convection maps.

4.1 Overall shape of the patterns, B_z^- and B_z^+ cases

Before proceeding to details, we would like to make a general statement on the shape of inferred convection maps for various IMFs. In agreement with a number of statistical models of the high-latitude convection (e.g., Heppner and Maynard, 1987; Ruohoniemi and Greenwald, 1996; Rich and Hairston, 1994; Haaland et al., 2007), the patterns were two-celled for negative IMF B_z and positive B_z with $B_t < 4$ nT. Additional, near noon, cells were visible for $B_t > 4$ nT. For some such maps, a clear 4-cell convection pattern was present while for others the pattern was a rather twisted 2-cell patterns as reported by Heppner and Maynard (1987) and Smith et al. (1998). We also would like to note that patterns for weak positive B_z of 0 - 4 nT were also two-celled.

We support our conclusion on the shape of B_z^+ convection maps by presenting two "sample" maps, Figure 4.1.

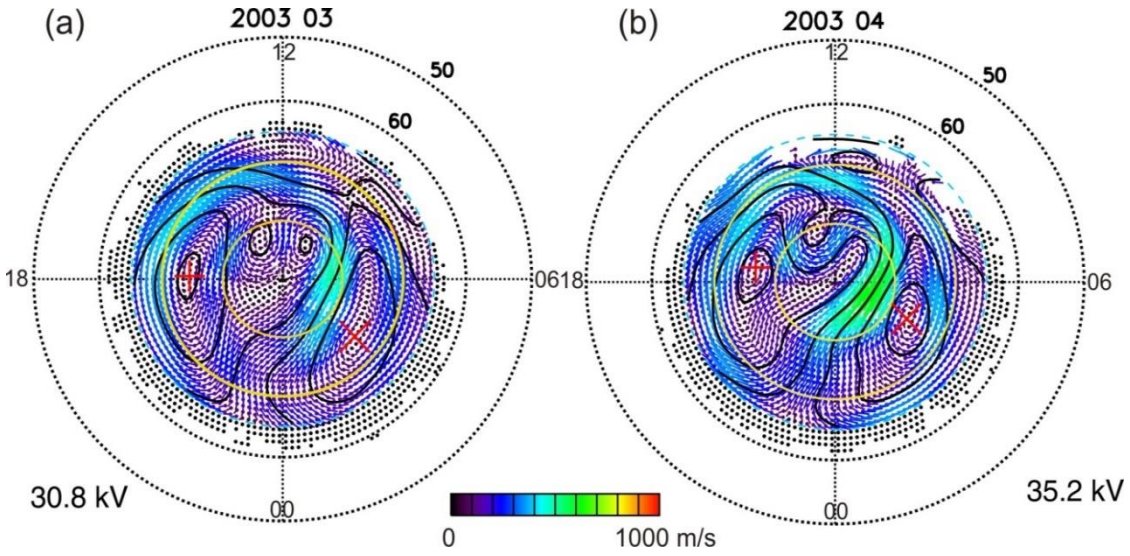

Figure 4.1: Convection patterns derived from monthly-averaged SuperDARN grid velocity data for IMF$B_t^+ = (6\ \text{to}12)$ and two consecutive months, March and April of 2003. Solid black lines are contours of electrostatic potential 6 kV apart. Convection vector length is denoted by color, in accordance with the shown color bar. Cross (plus sign) is the center of the counter-clock-wise circulation (clock-wise circulation) dawn (dusk) convection cell.

Data for March 2003 in Figure 4.1a show clear signatures of two reverse convection cells at near noon hours. Their centers are in the middle of the small contours. Figure 4.1b for April 2003 shows a rather twisted near-noon 2-cell pattern with velocity sunward flow portion at ~ 12:00 MLT being a part of the dusk convection cell. A similar pattern was presented by Heppner and Maynard (1987), their Figure 12. Two other prominent features on the plots of Figure 4.1, recognizable by color, are overall enhanced velocities during afternoon-dusk hours for the auroral zone (MLAT=65° -75°) and during early morning – dawn hours for the polar cap (MLAT > 80°). One can also notice a stronger flow in the dusk polar cap for April as compared to March. In the following sections, we will be considering two latitudes, MLAT=72° and MLAT=82°, to characterize plasma flows in the auroral zone and in the polar cap, respectively. Both points are positioned away from the CRB location so that minor shifts in the CRB location do not affect the trends.

4.2 Velocity magnitudes with and without IMF consideration

Our first step is evaluation of the impact of the IMF polarity consideration on the convection pattern. As reviewed in Section 1.5, the flow is expected to be faster for stronger negative IMF B_z. The fact that the IMF assumes positive and negative values roughly equal amount of time for each month has an implication for the convection intensity at a specific point in the ionosphere: namely, the intensity of the flow would be somewhat larger for cases of negative B_z as compared to cases of positive B_z. This is exactly what has been observed while data in various time sectors were compared. As an example, in Figure 4.2 we compare data for the convection velocity vector

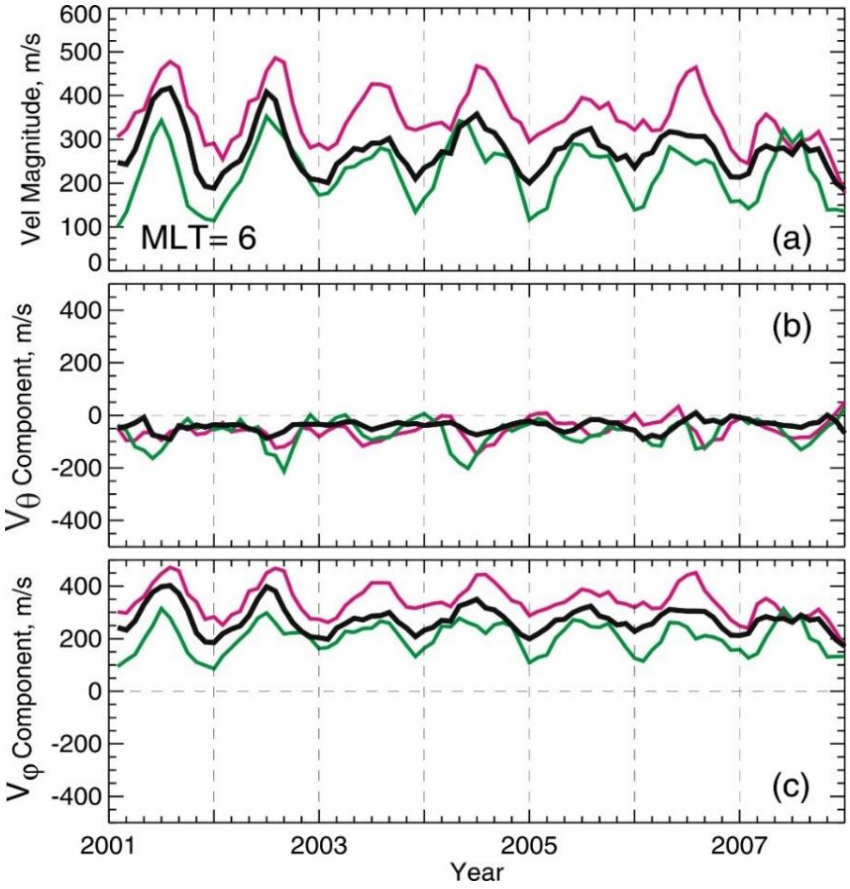

Figure 4.2: Variations of the (a) velocity magnitude, (b) V_θ velocity component and (c) V_φ velocity component for MLAT= 72° and at 06:00 MLT of each month. Monthly-averaged SuperDARN data during 2001-2008 were used for making the plot. Pink (green) curve represent the inferred velocity for B_z in between -4 nT and 0 nT (0 and 4 nT) conditions. Black line represents the velocity inferred from the entire SuperDARN data set for all available IMF values.

at MLAT=72° (magnitude and azimuthal V_φ and zonal V_θ components) obtained for the cases of B_t^+= (0-4) nT and IMF B_t^-= (-4 – 0) nT, i.e. for the cases of a weakly driven flow with positive and negative B_z, pink and green curves respectively. Estimates at 06 MLT of each month between 2001 and 2008 were considered. We also show here velocity data from maps that were produced without IMF consideration (as in Chapter 3), black line.

We see in Figure 4.2 that the V_φ component and magnitude are as expected: the values for B_z^- and B_z^+ cases are extremes for the black line which is located somewhere in between the pink and green curves. The V_θ components are comparable to each other for all three cases and stay at low absolute levels. We note such a clear-cut expected location of the black curve does not happen for all MLT sectors; sometimes it is close to extremes and on some rare occasions it goes beyond those extremes.

4.3 Velocity magnitude for various B_t bins. Approach to the analysis

The convection maps presented in Figure 4.1 (and other similar maps) show strong velocity magnitude variations with magnetic local time and magnetic latitude, as mentioned. A quick search through the maps also shows variability of the velocity at a specific point with season and, certainly, with the IMF conditions.

To give a general assessment of the data trends we computed median values of the velocity for specific bins of the IMF and specific latitudes. Figure 4.3 illustrates our approach. Here each grey line spanning from -9 nT to +9 nT (no individual line can be traced in its entirety) connects values of the velocity magnitude (at MLAT=72° and 22 MLT) for central values of the six IMF B_t bins. For the plot of Figure 4.3, data for 180 months of observations have been considered (1995-2011). The median values of the magnitude for each B_t bin are shown by red dots. The vertical bars are the standard deviations within each B_t bin. Both the velocity medians and the band of all possible curves show clear velocity magnitude increase with increase in the magnitude of the B_t for B_t^- conditions. For B_t^+ conditions, there is only a minor tendency for an increase.

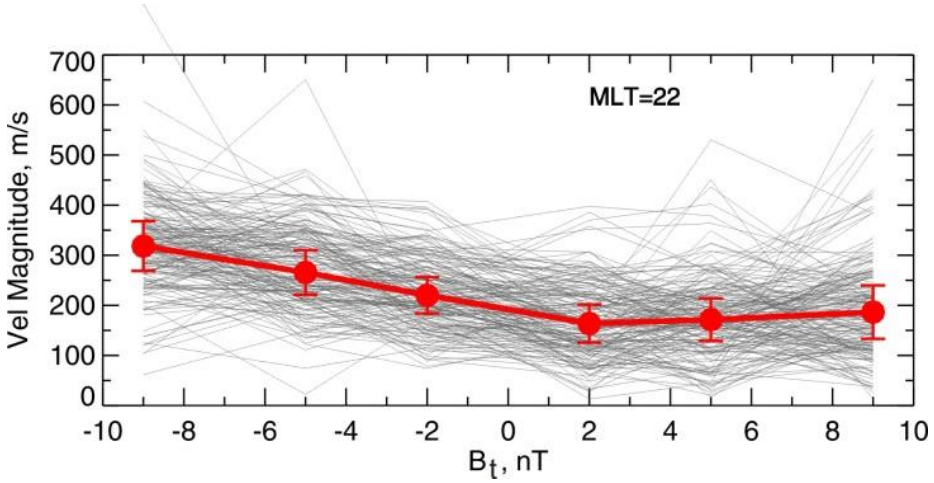

Figure 4.3: Velocity magnitudes at MLAT=72° and 22-23 MLT inferred from SuperDARN data that were sorted according to six IMF B_t bins as describe in the text. The groups are centered at -9, -5, -2, +2, +5, and +9 nT. Monthly-averaged SuperDARN maps between 1995 and 2011 were considered. The grey lines connect the raw data on the velocity (one vector on the maps for each month) for specific month, MLAT and MLT of observations but for six groups of the IMF B_t. The red line connects the dots representing the median value for all inferred velocities (i.e., out of 180 points) for a specific value of the IMF B_t. Vertical bars are the standard deviation of the velocity magnitude within each bin of the IMF B_t.

4.4 Velocity magnitude in the auroral zone and polar cap

Now we compare the dependence of the plasma velocity magnitude upon B_t in the auroal zone and in the polar cap by considering data at MLAT=72° and 82°, Figure 4.4. In Figure 4.4 the near noon and midnight are denoted by blue and red line, respectively, and the format of presentation is as described in the previous section except of the raw data for all 180 months have been removed. The obvious difference between the noon and midnight data is that the blue and red lines are close to one another in the entire range of B_t for midnight while the velocity magnitude in the polar cap is much larger than in the auroral zone for negative B_t for noon period. The differences here are by a factor of 2. For positive B_t, the velocity magnitudes are about the same for all three B_t bins. For the noon, noticeable are large standard deviations indicating strong variability of the velocity at lower latitude. One conclusion from this plot is that the velocity "responds" to changes in B_t differently at various latitudes and in different MLT sectors.

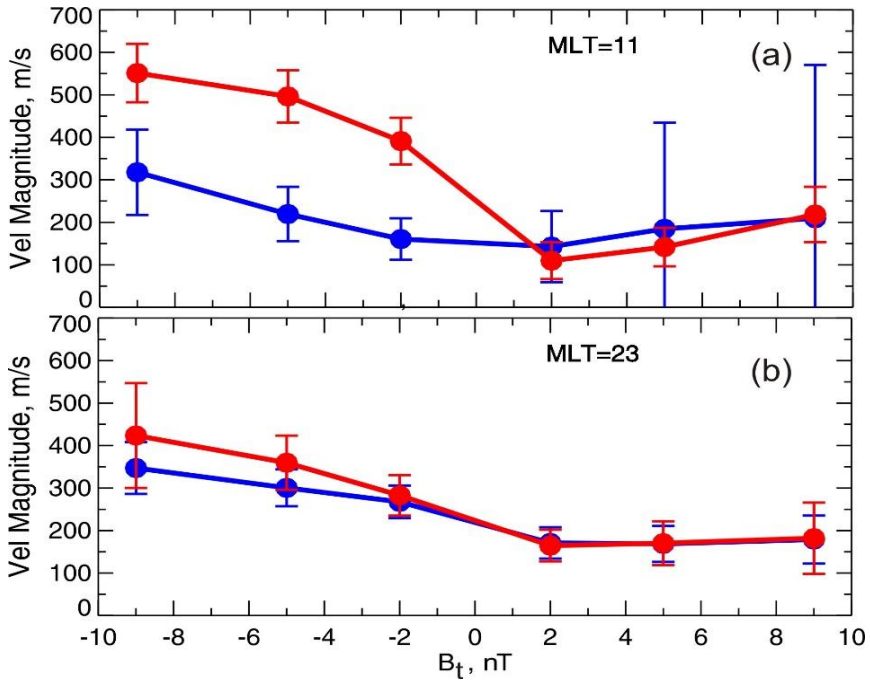

Figure 4.4: Median values for the convection velocity magnitude at MLAT=82° (red line) and MLAT=72° (blue line) inferred from SuperDARN monthly-averaged maps for 6 bins of the IMF B_t bins centered at +/-9, +/-5 and +/- 2 nT. Data for 1995-2011 were considered. Panel (a) is for 11-12 MLT (noon) while panel (b) is for 23-24 MLT (midnight).

4.5 Seasonal effect in the velocity magnitude, polar cap case

Now we consider seasonal changes in the velocity magnitude for the polar cap point of MLAT=82°. In Figure 4.5a,b we show, by black diamonds and black line, the same velocity magnitudes as in Figure 4.4a,b for the noon and midnight sectors. Overlaid red and blue circles are the velocity magnitude medians inferred by considering only July (summer) and December (winter) data in each year between 1995 and 2011. For the noon sector, winter values are consistently smaller than summer values, up to ~150 m/s. The effect is much smaller for positive B_t. Also for this sector, the combined data velocity values are in between extremes of separately-computed summer and winter values. Such a relationship holds in other time sectors and some B_t values, presented in Figure 4.5, although not for all.

In Figure 4.5b the seasonal effect is not clear. For example, summer velocities are larger for B_t=-9 nT while they are smaller by about the same amount for B_t=-5 nT. As in other time sectors, the summer/winter differences are smaller for small B_t magnitudes.

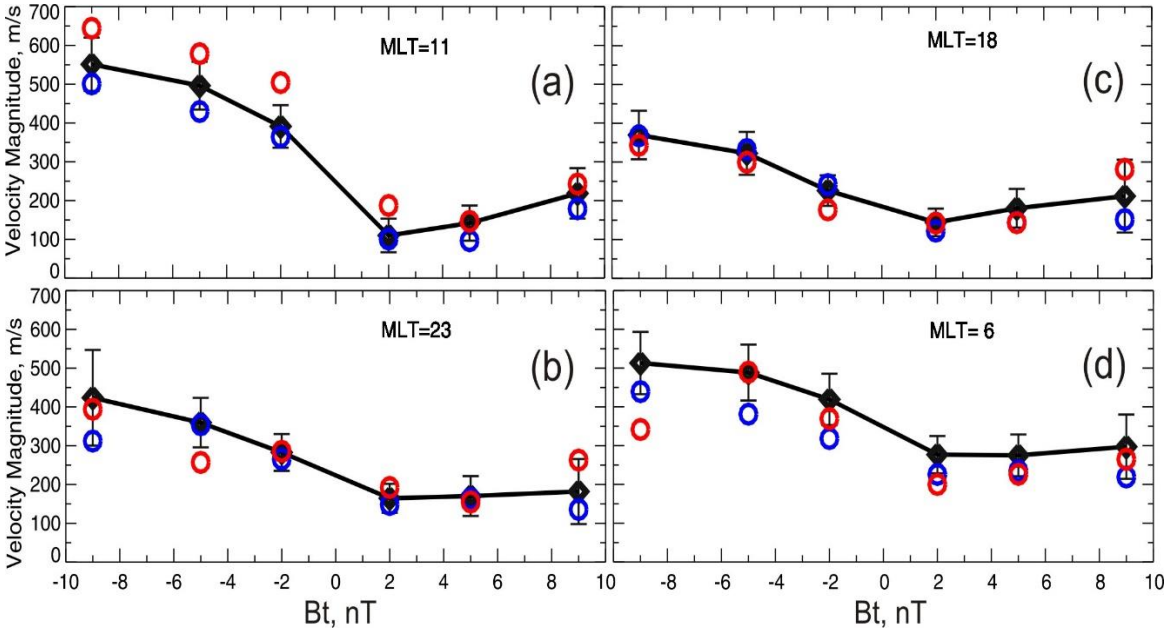

Figure 4.5: Median values of the convection velocity magnitude at MLAT=82° inferred from monthly-averaged SuperDARN maps for 6 bins of the IMF B_t centered at +/-9, +/-5 and +/12 nT. Data for 1995-2011 were considered. Panels (a)-(d) correspond to MLT=11 (noon), 18 (dusk), 06 (dawn) and 23 (midnight), respectively. Red and blue circles are the velocity magnitudes for summer, July and winter, December, respectively. Black diamonds connected by the black line are velocity magnitude median values for a data set with all months being considered.

Figures 4.5c and 4.5d show data for the dusk and dawn, respectively. The combined (winter plus summer) data set shows smaller velocity values than those for the noon sector for negative B_t and larger values for positive B_t. In this time sector, velocity magnitudes are smaller summer time (red circles) as compared to winter ones for same B_t but the differences are not large (<50 m/s). Finally, the dawn velocities are larger for all B_t, consistent with the convection maps of Figure 4.1.

4.6 Solar cycle effect in the polar cap convection velocity

We showed in Section 3.1 that the IMF can achieve larger B_t values for the solar cycle maximum months. In addition, Figures 4.4-4.5 show a clear effect of the velocity increase with B_t. One then would expect a general increase of the velocity toward the solar cycle maximum. Figure 4.7 illustrates this expectation for noon and dusk sectors for the polar cap latitude of 82°. Here solid dots and thick (open circles and thin lines) lines represent solar cycle maximum (solar cycle minimum) velocities. The effect is very strong for noon where differences are as large as 250 m/s,

for negative B_t. It is less evident for B_t>0 and in the dusk sector. This is rather a general conclusion from the data in other time sectors – the solar cycle effect is strongest for the near noon sector.

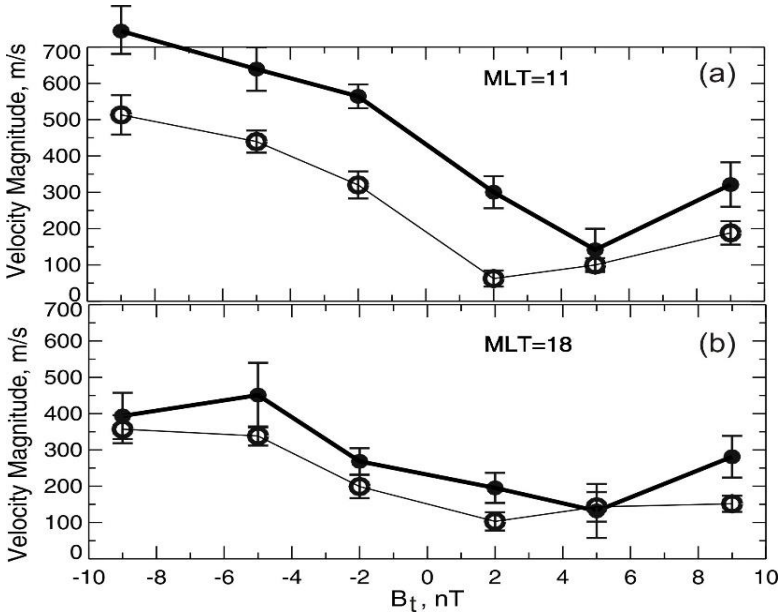

Figure 4.6: Median values of the convection velocity magnitude at MLAT=82° inferred from monthly-averaged SuperDARN maps for 6 bins of the IMF B_t centered at +/-9, +/-5 and +/- 2 nT. Solid dots and thick line are for observations during high solar activity (2000-2005) and open circles and thin line are for observations during low solar activity (1995-1999; 2006-2011). Vertical bars are the standard deviation of the velocity within each IMF B_t bin. Panel (a) is for 11-12 MLT (noon), panel (b) is for 18-19 MLT (dusk).

4.7 Discussion

Data presented in this Chapter showed several features of the high-latitude convection known from previous publications. These are all related to the velocity dependence on the IMF B_t or B_z component.

The most obvious effect, seen on all plots, is an overall increase of the anti-sunward convection velocity in the polar cap (as well as in the auroral zone, although only one plot was given for the auroral zone flows, Figure 4.2) with IMF B_t in a case of B_z<0. To a first approximation, the dependence of the velocity upon B_t is linear. The data of Figure 4.3 and similar plots for close MLT sectors can be roughly represented by

$$\text{Velocity} = a \cdot (|B_t| - 2) + b, \quad B_t < 0, \qquad a < 0, \tag{4.1}$$

where the coefficients a and b are on the order of 30-40 m/s/nT and 100-150 m/s, respectively. We cannot claim specific number for the dependence (4.1) because we have just 3 velocity values for $B_t<0$ (similarly for $B_t>0$). On the basis of trends seen in Figure 4.5, we expect, however, that the SuperDARN data being processed into finer bins of B_t would show an increasing trend. Mori (2012) reported that the SuperDARN CPCP, that characterises the plasma velocity intensity within the polar cap, correlates better with the $\sqrt{B_t}$. Wilder et al. (2010) explored similar idea by looking at AMIE modeling of the polar cap electric field.

We have to note that the relationship of the velocity and B_t is less prominent in other time sectors, away from the noon. The contrast is strongest between the noon and midnight velocities. This is a surprise because the flows on the dayside must be roughly matched in magnitude by flows on the nightside for the flow to be continuous. One explanation is that we considered here only one area while we have to consider the entire anti-sunward stream to make a judgement. We leave investigation of this issue for future work. As a first step, we analyzed data presented in Figure 3.2. We computed average velocity of the flows toward the noon (at latitudes of the auroral oval, 60° -75°) and the flows away from the noon (in the polar cap, 75°-90°) and found the difference to be of the order 19 m/s (257.3 m/s for the speed of the flow from the noon and 238.7 m/s toward the noon). This difference is not significant taking into account the fact that data considered here are over significant spatial and temporal scales.

The second, less exciting but prominent feature from the data presented in this Chapter, is slow, if any, increase of the anti-sunward convection velocity in the polar cap with IMF B_t in a case of $B_z>0$. This is in contrast with expectation that polar cap electric field should increase proportionally to B_t (Wilder et al., 2009; 2010; 2011). Wilder et al. (2010) reported the effect to be stronger in summer time. Reviewing our plots for various months, we found that indeed an increase of velocity with B_t is stronger in summer time although the dependence is still slow with maximum slopes of ~10-20 m/s/nT which is about 2 times slower than those for the negative B_t.

Another clear feature of many plots is a stronger velocity increase with B_t on the dayside in the polar cap as compared to the nightside and the auroral zone. Several publications (e.g., Ridley et al., 1998; Ruohoniemi and Greenwald, 1998; Shepherd et al., 1999; Nishitani et al., 2002; Freeman, 2003; Yu and Ridley, 2009) showed that when IMF B_z suddenly changes to more negative values, the convection velocity intensifies first on the dayside, near noon. Later on, the region of enhanced flows expands to time sectors away from the noon. It might take up to 30 min to establish

equilibrium, balanced flow in all MLT sectors (Nishitani et al, 2002; Fiori et al., 2012). Statistical averaging these kind of events would end up with stronger "response" of the near-noon flows on B_t change than the midnight flows. We think that the effect contributes to B_t "asymmetry" in our plots. A question might be asked what would happen with the convection magnitude when the IMF makes a transition from negative B_z to positive B_z. One would expect just opposite effect, decrease of the convection magnitude and on the dayside first of all. Unfortunately, there is no answer to this question, to the best of our knowledge. Finally we note that the "asymmetry" in the velocity magnitudes for various B_t is less prominent if one compares dawn and dusk data, Figure 4.5c, d.

In addition to previously known results, we reported in this Chapter some new features that, to the best of our knowledge, have never been reported in the past. We would like to start with the velocity variation within the solar cycle. We showed in Figure 4.6 that the plasma velocity in the polar cap increases by 30-40% toward the solar cycle maximum. This is a stronger increase than what we reported in Chapter 3, where all the SuperDARN data were considered without paying attention to the sign and intensity of B_t. The effect exists for both $B_z<0$ and $B_z>0$ although it is stronger for $B_z<0$. We are not aware of publications discussing solar cycle effect for other parameters critical for plasma flows, for example the field-aligned currents. Again, the effect was less obvious for the nightside data. Reasons for these differences require further work.

Our results on the velocity changes versus season are confusing. Only for near noon observations we can state that the velocity increase is faster in summer time (as compared to winter) for $B_z<0$ case. For $B_z>0$, the rates of the velocity increase are about the same during summer and winter and they are smaller than for the $B_z<0$ case. Faster summer response on the B_z increase is not absolutely unexpected. Various SuperDARN publications have shown that the CPCP is about the same in conjugate ionospheres, e.g. Mori et al. (2012). On the hand, as we showed in Chapter 3, the centers of the convection cells are often located closer to each other (CRB boundary is at larger MLATS) in summer time, which could translate to large summer time electric field. This argumentation, however, requires understanding why the CRB shifts closer to the Pole in summer time and we see this as an important task for magnetospheric physicists (this aspect is beyond the scope of the present Thesis).

4.8 Conclusions

In this Chapter, we identified some trends in the high-latitude convection magnitude related to an increase in the magnitude of the IMF transverse magnetic field B_t. Some of the features identified are as follows.

1) Convection velocity increases with B_t, linearly to a first approximation. The rate of increase is much faster for the B_t^- conditions as compared to the B_t^+ conditions for which the effect is very weak.

2) For the B_t^- case, the effect of the velocity increase is stronger at the polar cap latitudes and on the dayside.

3) The effect of the velocity increase with B_t for the case of B_t^- is stronger during high solar activity and on the dayside.

4) For the B_t^- case, typical dayside velocities are ~1.5 times larger during high solar activity as compared to those during low solar activity. The contrast is not significant on the nightside and for all MLT sectors for the case of B_t^+.

CHAPTER 5

MERIDIONAL POLAR CAP PLASMA FLOWS. RKN AND INV RADAR OBSERVATIONS

In this Chapter we investigate the response of the high-latitude convection to changes in the rate of the IMF merging (with the Earth's magnetic field) that we characterize by the coupling functions such as the reconnection electric fields, E_{KL} and E_{RC} for $B_z<0$ and $B_z>0$, respectively (see Chapter 1). We will refer to these functions as the "drivers" of the high-latitude convection keeping in mind the fact that they reflect the cross polar cap potential applied to the Earth's ionosphere and thus characterize the strength of the plasma flows in the polar cap (e.g., Shepherd et al., 2003; Newell et al., 2007; Koustov et al., 2009; Wilder et al. 2008, 2010). The approach in this Chapter is completely different from that undertaken in Chapters 3 and 4. We consider here data from only two SuperDARN radars, at Rankin Inlet (RKN) and Inuvik (INV), Figure 5.1. The radars monitor plasma flows at very high latitudes, predominantly in the polar cap. These radars are traditionally referred to as the PolarDARN radars. We compare measured velocities with the parameters of the solar wind and IMF on a point-by-point basis. The work in this Chapter is an extension of the study by Fiori et al. (2009) where the PCN magnetic index (Troshichev et al., 2006) was selected as a parameter characterizing external drivers of the ionospheric circulation. There are two reasons for changing the driving parameter in the present work. One of these is a concern about the quality of the PCN index for characterizing the ionospheric convection intensity (Fiori et al., 2009; Lukianova et al., 2002; Troshichev et al., 2006). In addition, this index has been designed for handling $B_z<0$ situations which does not allow us to investigate the interesting case of $B_z>0$. The other reason is that several recent publications (e.g., Shepherd et al., 2003; Wilder et al., 2010) used E_{KL} and E_{RC} as driving factors.

5.1 Geometry of observations

Figure 5.1 shows the field of views (FoVs) of the RKN and INV radars in the Canadian Sector of the Arctic. The radars are located at high geographic and geomagnetic latitudes and capable of monitoring the plasma flow in the polar cap at magnetic latitudes MLATs > 80°. The central beams of the radars, 6, 7 and 8, are oriented roughly perpendicular to lines of equal geomagnetic latitude, i.e. roughly along geomagnetic meridians. For these beams at near noon and near midnight, when the plasma flow is predominantly along the noon-midnight meridian, the measured LOS velocity would reflect the total flow velocity vector. This is not to say that the near-noon observations are always along the average plasma flow direction as the direction varies, depending on external conditions, and we will give an example of the near-noon velocity variations later on. In other time sectors, the radars would measure, statistically speaking, only a component of the total velocity and this component would become close to zero at dusk and dawn in a case of a two-cell convection pattern. Fiori et al. (2009) investigated this issue specifically for the RKN radar. They compared the RKN radar look direction with the flow direction inferred from all SuperDARN radar data and concluded that around 10-11 MLT, the directions are close to each other.

In this Chapter we limit our presentation to only one set of specific ranges of the radars, namely, range gates 21, 22 and 23. These range gates correspond to MLAT~82°. They are at the far edge of the region with the best echo detection rate for both radars (Ghezelbash et al., 2015). Although at shorter ranges the echo occurrence rates are somewhat better, those locations are less attractive as the plasma flow tends to change direction in the throat region starting from latitudes of ~80° and the alignment of the central beams with the flow direction deteriorates.

We also show in Figure 5.1 the location of the Resolute Bay (RB) observatory. Here two important instruments are located, the CADI ionosonde and incoherent scatter radar AMISR-N. We note that the radars' spots of investigation that we undertake in this Chapter are close the RB location; this makes it possible to compare (in future) RKN-INV results with statistics on convection inferred from the RB ionosonde and with data of existing AMISR-N incoherent scatter radar and future AMISR-C radar that is coming up for operation in the near future.

Finally, we would like to mention that the Polar DARN radars have been mostly operated with 1-min scans. This is fortunate for comparison of the radar and solar wind/IMF data. Information on the solar wind and IMF were downloaded from the NASA website,

http://omniweb.gsfc.nasa.gov/ow_min.html, the so called OMNI data base built mostly on measurements from the ACE spacecraft positioned at the Lagrangian point (~200 R_E sunward from the Earth). The OMNI data are referenced to the bow shock location propagating ACE measurements from the Lagrangian point to 17 R_E upstream of the Earth based on the Weimer technique (Weimer et al., 2003). We allowed an additional 8 min delay for the disturbance to propagate from the bow shock to the ionosphere. We note that certainly there was some time difference between an actual radar measurement and a record of the solar wind parameters as the radars start scans exactly at the beginning of each minute. However, the time differences are less than ~30 seconds and we neglected this timing difference. It also must be taken into account that the actual ACE measurements are done with different time resolution and we are dealing with extrapolated data from the satellite.

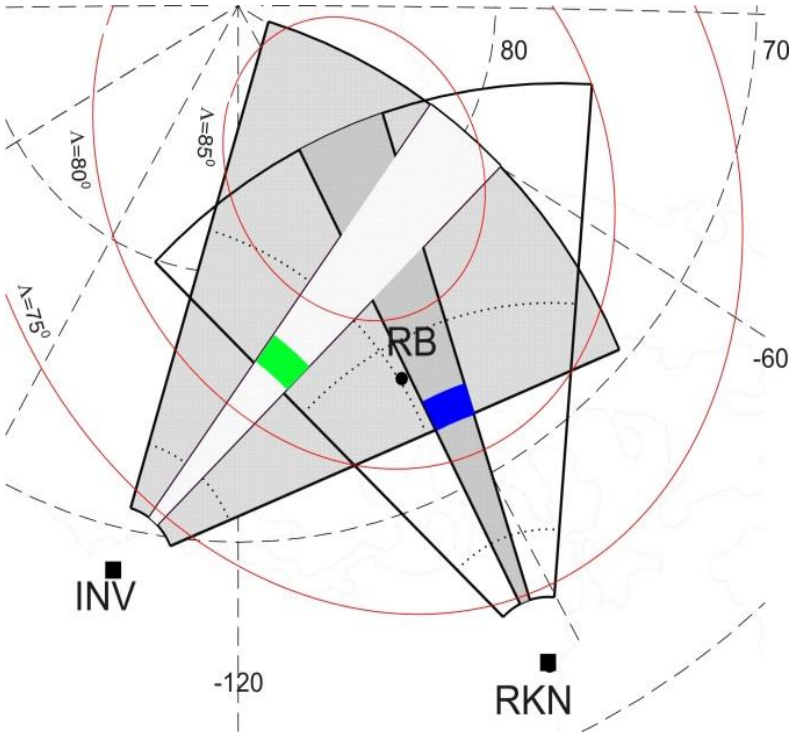

Figure 5.1: Fields of view (FoV) of the Canadian PolarDARN radars at RKN and INV and their central beams (shown by different tone) 6, 7, 8 that were selected for the analysis. The FoV shown is limited to range gate 50. Dotted circles within the FoV are locations of range gates 10 and 30. The blue and green boxes are specific range gates/beams considered - gates 21, 22, 23 within beams 6, 7, 8. The solid dot is the location of the Resolute Bay (RB) observatory.

5.2 Median RKN and INV velocities, their seasonal and diurnal trends

We first give a general assessment of the RKN and INV radar velocities for the selected areas of the polar cap ionosphere by considering one-hour median values. Figure 5.2 explains the approach undertaken. Figure 5.2a presents all the velocities measured by the RKN radar in March 2013 in range gates 21-23. More than 72000 points are available. The reason for the selection of March data (i.e. for the equinox) is that echoes are observed evenly during all hours of the day, as opposite to other seasons when echoes occur predominantly during near solar noon hours (12 MLT).

Figure 5.2c shows that the number of echoes is somewhat larger from 00 to 12 UT, i.e. for dusk-midnight-dawn sectors. The magnetic noon (midnight) for the RKN radar spot location is around 18:30 (06:30) UT. The velocity changes smoothly over the day, Figure 5.2c. There is more significant spread at near midnight and near noon hours. The velocities become more and more negative after 12:00 UT (dawn) but around noon the positive velocities seem to occur as frequent as the negative velocities. The positive near-noon velocities are unexpected if the plasma circulation pattern is two-cell like. The initial hypothesis for the occurrence of the positive near noon velocities is the onset of sunward (reverse) plasma flows during intervals with positive B_z. This hypothesis will be investigated later.

The other feature recognizable in Figure 5.2a is the frequent occurrence of low-velocity data with velocity magnitudes of <50-100 m/s. These are seen as horizontal blobs or stripes around the zero velocity line between ~12:00 and 24:00 UT.

To infer velocity trends in a quantitative way, we binned the data over 1-hour periods and selected the median value for each bin, Figure 5.2b. Two kinds of medians can be used, one for all data in a bin (shown by dashed blue line in Figure 5.2b) and for all velocities with magnitudes above 50 m/s in a bin (shown by red line with large red dots in Figure 5.2b). In Figure 5.2b the trends are similar for both types of binned velocities. The differences are slightly larger in the dawn-noon-dusk sector. Both types of medians show maximum values of ~300 m/s near midnight and small positive values around noon. In the following analysis, data with velocity magnitude below 50 m/s will not be considered. The reason for this is that these data may affect the median velocity values significantly. The reason for low-velocity echo occurrence is not clear. One hypothesis is that these are mixed ground-scatter/ionospheric echoes or misidentified ground scatter echoes. These hypotheses require further investigation. We note that the monthly velocity

medians were inferred from a significant data set for each hour, very often in access of 1000 points, Figure 5.2c.

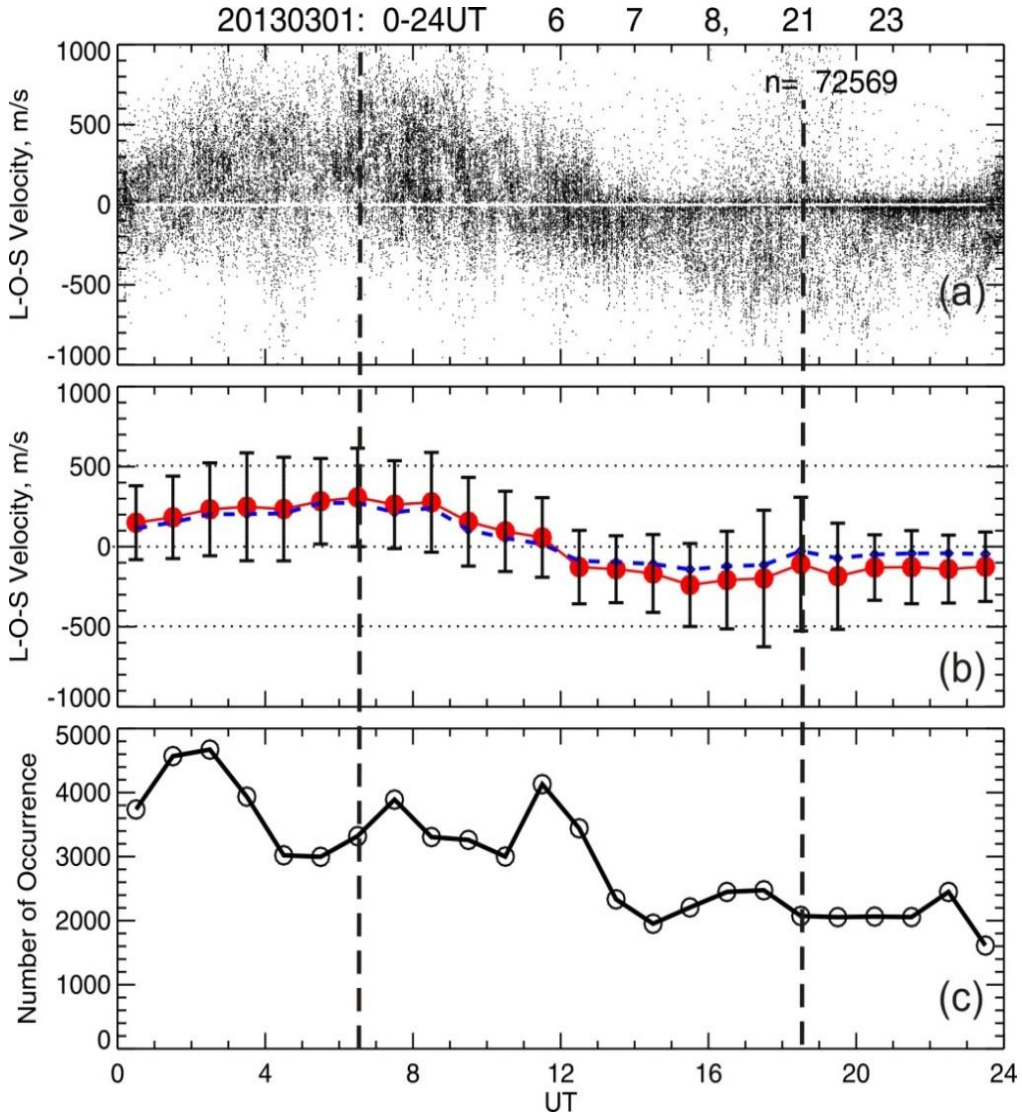

Figure 5.2: (a) Scatter plot of the RKN velocity versus UT time observed in March 2013. Measurements in beams 6, 7 and 8 and range gates 21, 22 and 23 were considered (as listed in the title). Total number of available points (n) is indicated. (b) Median values of the RKN velocity for 1-hour UT time intervals. Dashed line corresponds to medians for all velocities available in each bin while red dots connected by red line correspond to velocity medians with the magnitudes above 50 m/s. Vertical bar represents the standard deviation of the velocity in various bins. Vertical dashed lines are approximate time for the magnetic midnight (06:30 UT) and noon (18:30 UT). For the beams considered, the magnetic local time is close to the local solar time. (c) Number of echo occurrence in each one hour interval for the data presented in panel (a).

RKN and INV velocity medians have been derived for a number of radar gates and a number of radar beams for all years of the PolarDARN radar operation. This allowed us to build diagrams like the one shown in Figure 3.8. We also undertook a more sophisticated analysis by combining RKN and INV data with estimates of the IMF and solar wind parameters. This approach allowed us to split available data onto subsets with specified IMF bins. In this Chapter, a very coarse binning was adopted. This was to have analogy with the even coarser binning adopted in Chapter 4. We limit our presentation here to observations in 2007-2010. One reason for such a limitation is that the diagrams obtained reflect most of the features that can be inferred from data for all observations. The other reason is that data processing for joint PolarDARN-solar wind set is time consuming and some parts of the work require significant time allocation.

Figure 5.3a,b shows the RKN velocity medians for observations in 2007-2010. Panel (a) considers only measurements with B_z^- while panel (b) considers only measurements with B_z^+. Figure 5.3c,d shows INV radar data in a format similar to that of Figure 5.3a,b.

Starting the discussion with the plots for the RKN radar (panels (a) and (b)), for B_z^- conditions, strongest positive velocities seen by the radar are ~400 m/s and occur between ~04 and 06 UT, i.e. during pre-midnight hours. One cannot say anything definite about seasonal variation, except perhaps that in winter time flows are enhanced for shorter periods near midnight as compared to other seasons (this is seen as a more "narrow" width of the red stripe reflecting high positive velocities). Negative RKN velocities are largest in magnitude between 16 and 18 UT, i.e. during pre-noon hours. Seasonally, magnitudes are larger in the summer time but there is a tendency for the flows to be intense for shorter periods around noon during summer (blue stripe is more narrow at these times). So, winter flows are less intense but continue for a longer period of time. Maximum velocity magnitudes for the near noon data are also about 400 m/s, consistent with the maximum for the near midnight data. Since the near-midnight data do not show a clear seasonal trend, there is no season-by-season correspondence in the maxima of the positive and negative velocity.

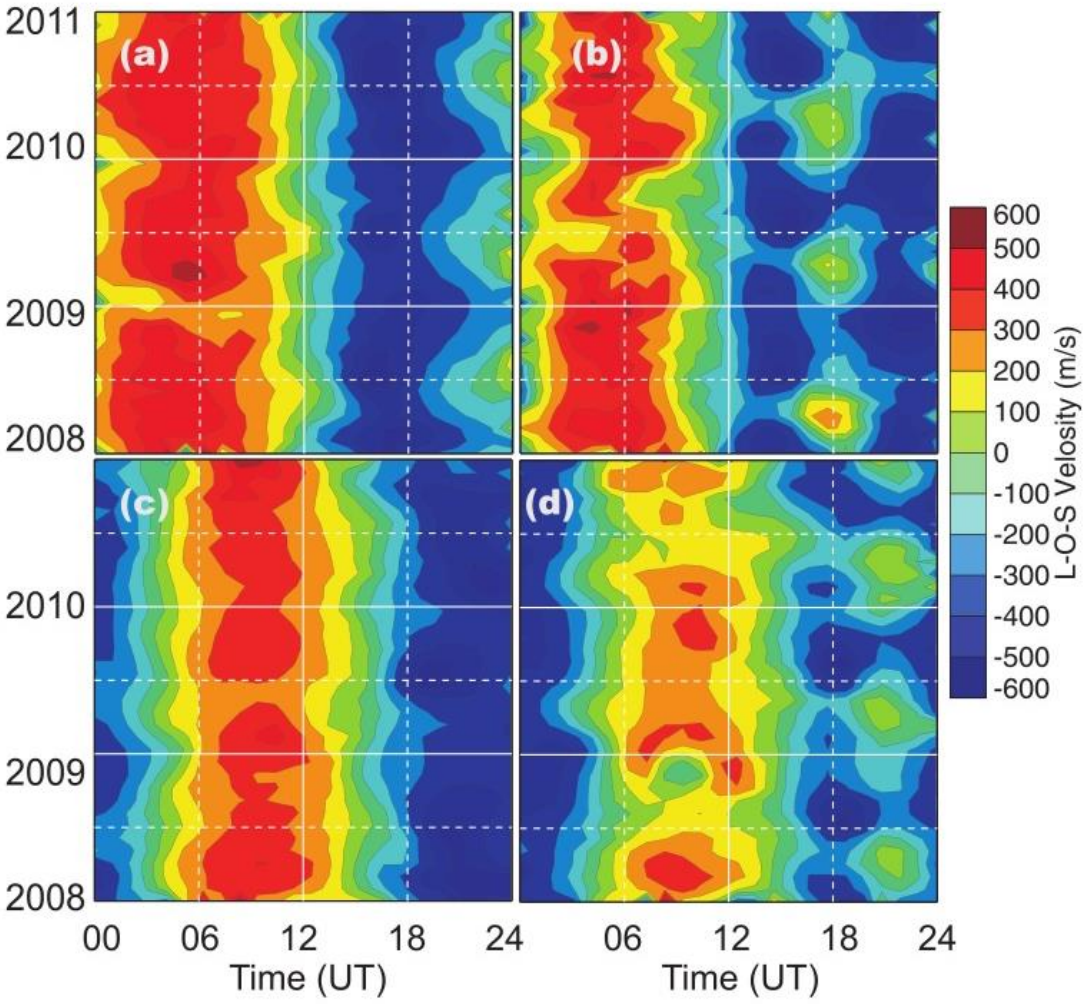

Figure 5.3: Contour plots of the RKN (upper raw) and INV (bottom raw) velocity (hourly medians) versus UT for observations in 2008-2010: (a) and (c) are radar data for IMF B_z^- condtions, (b) and (d) are radar data for IMF B_z^+ condtions. All data were collected in beams 6,7, and 8 and range gates 21, 22, and 23. Contours are 100 m/s apart.

For B_z>0 and during midnight hours, Figure 5.3b, the contours for the positive velocity are about the same as in the previous case except they are more narrow. Here the "red" stripe maximum values are about the same, ~400 m/s. The velocity contours at near noon hours are quite different here from those of the B_z < 0 case. We see that although the negative velocities of ~ -400 m/s do still occur during pre-noon hours of ~16 UT during summer, at near noon (~ 18 UT), "islands" of positive velocity appear. These are the highly anticipated sunward flows. The islands are "centered" at spring equinoxes and consistently at ~ 18 UT (i.e., always very close to the magnetic noon, 12 MLT). The other effect, seen in the B_z^+ data is occurrence of negative velocities during

dusk hours of ~ 22-24 UT. For this period and B_z<0, the velocity becomes near zero or even positive, compare with Figure 5.3a.

INV data presented in Figure 5.3c, d show a great deal of similarity with the RKN data of Figure 5.3a,b except of a ~3-hour shift toward later hours in the location of the maxima of the red and blue stripes. The 3-hour RKN-INV time difference in occurrence of the velocity maxima is expected because the radars are separated by about 3 hours of magnetic local time so that the Harang discontinuity and the dayside throat occur first within the RKN radar FoV and later on within the INV FoV. For INV B_z^+ data, the summer maximum is only evident for 2009. Another difference is generally smaller INV positive (nighttime) velocities so that the maximum velocity is 300 m/s.

INV data for the B_z^+ case also show ~3-hour shifted pattern as compared to that of RKN data. The positive velocity magnitudes are also ~100 m/s smaller here. We note that positive velocities during spring equinoxes are seen at these radar ranges only for B_z^+ conditions. This is contrary to observations at larger RKN radar ranges, presented in Figure 3.8, where islands of positive velocity can be seen if all the data, irrespective on IMF conditions, are considered. This implies that reverse plasma flows are somewhat stronger at latitudes deeper in the polar cap. We also note that, overall, data of Figure 5.3 indicate somewhat stronger velocity magnitudes for B_z^- as compared to those for B_z^+, but not drastically different. This is not quite consistent with our analysis undertaken in Chapter 4.

5.3 Response of the polar cap meridional flows to changes of an external driver: A case of 8 February 2013

So far we have looked at velocity medians averaged over month-long data sets. Now we consider data with better time resolution. Our first goal is to give a general sense of how the LOS velocity responds to changes in the external conditions, or the "convection drivers". We will consider RKN radar data for the 8 February 2013 as an example. We note that this event was selected for a simple reason that data coverage was reasonable for several hours around noon on the dayside, where the response of the plasma flow velocity to quick changes in the solar wind

conditions is highly expected (e.g., Fiori et al., 2012). The other reason is that during this event, the IMF showed quick variations from negative to positive IMF B_z values and backward, from positive to negative values. The IMF transition magnitudes were of the order of 4 nT, which is not particularly strong but sufficient enough to easily identify effects in the flow. Finally, the event has a reasonable amount of data for both IMF B_z<0 and IMF B_z>0, which does not happen too often. For a statistical type of analysis later on, we will consider radar data for one hour-long periods near magnetic noon (17-18 UT) and we will consider events with smooth, if any significant, variations of the IMF.

Figure 5.4 compiles all the data we would like to explain. Figure 5.4a shows measured velocities in beams 6, 7 and 8 and range gates 21, 22 and 23 over 3-hour period of 16:30-19:30 UT, small dots. One can notice that several dots exist for some moments. This is because echoes have been detected in several beams/gates and the velocities were somewhat different. For some periods no echoes are seen. To show a general trend in the LOS velocity, we binned the velocity data over 10-min intervals; the binned velocity values are shown by black circles of much larger size.

We see in Figure 5.4a that the binned velocity was negative at the beginning of the event, but it changed to positive values at about 16:55 UT. The transition to positive values was smooth, and the velocity was increasing for almost an hour. The binned velocity was positive for ~1.5 hours until about 18:30 UT when it suddenly returned back to negative values and stayed negative until the end of the event. We note that although positive velocities at near noon hours of ~18:00 UT are expected for large positive IMF B_z, such a prolonged existence of the sunward flows, as in the considered event, is unusual. We also note that, according to our analysis, having positive IMF B_z does not imply automatic onset of sunward flows; for some periods positive velocities are seen only for very short time if at all.

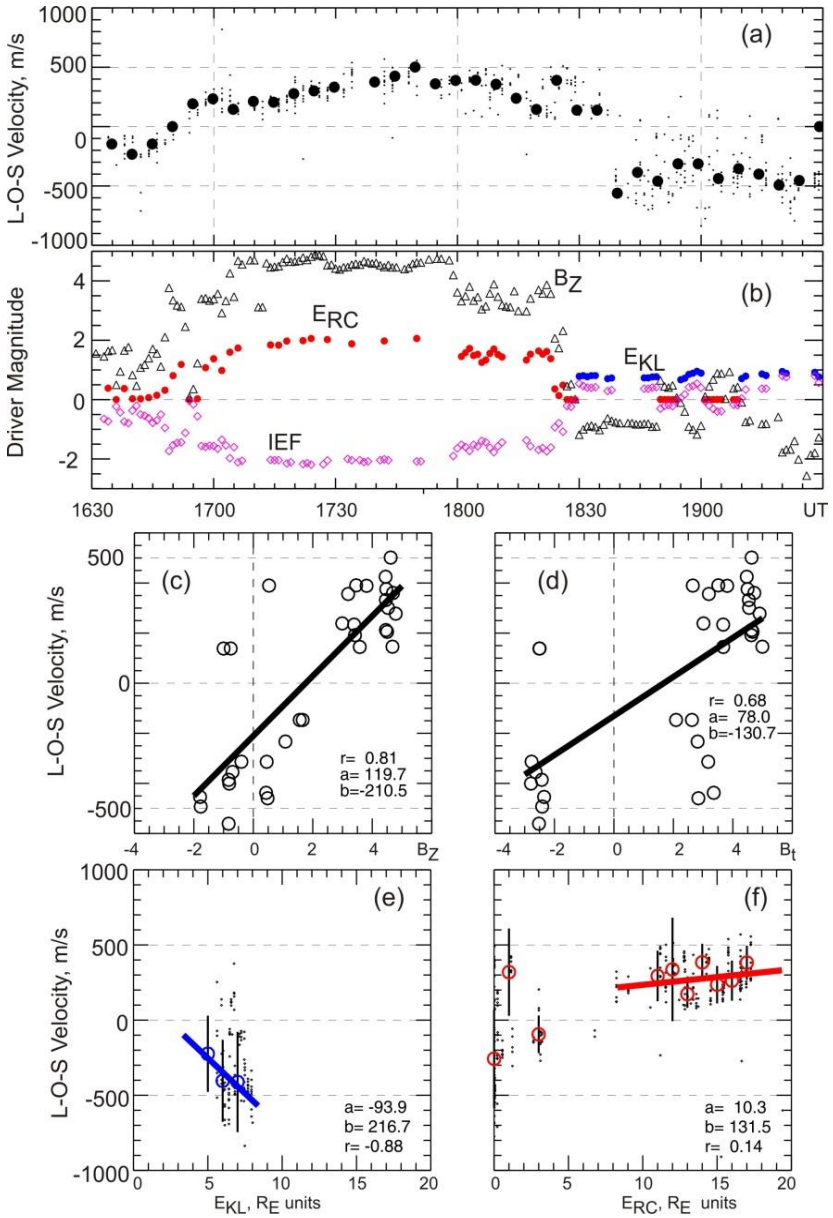

Figure 5.4: RKN LOS velocity (recorded in beams 6, 7, and 8 and gates 21, 22 and 23) and IMF/solar wind data for the event of 08 February 2013 between 16:30 and 19:30 UT. (a) Scatter plot of the LOS velocity (small dots) and velocity medians over 10-min intervals (black circles) (b) Temporal variations of the potential drivers of the convection. The units of the y-scale depend on the parameter considered: the scale is nT for IMF B_z, mV/m for interplanetary electric field (IEF), units R_E for Kan-Lee reconnection electric field (E_{KL}) and reverse convection electric field (E_{RC}) as explained in the text. Plots (c) and (d) are scatter plots of LOS velocity versus IMF B_z and B_t, respectively (10-min medians for both parameters), plots (e) and (f) are scatter plots of LOS velocity versus E_{KL} and E_{RC} binned (open circles) and characterized by the linear fit lines with the parameters "a" and "b and correlation coefficient "r" as explained in the text.

Figure 5.4b gives information on the solar wind and IMF in the form of several potential drivers of the convection, Chapter 1. The triangles represent the IMF B_z component. It was positive during most of the event but it suddenly changed the polarity at ~18:22 UT. Clearly, period of positive and enhanced B_z correlates well with the long-lasting period of positive RKN LOS velocity. Toward the end of the event, during negative IMF B_z, the RKN LOS velocity is negative. Such a correlation of positive (negative) velocity and positive (negative) IMF B_z is highly expected.

Of special interest are data around the quick change of the IMF polarity (transition) to negative values at ~ 18:22-18:25 UT. The first "reaction" on the IMF change is a sudden "jump" of the RKN velocity ~ 200 m/s, in contrast to general trend toward velocity decrease prior to this moment. This is unexpected as a decrease of the B_z^+ would imply weakening of the sunward flow driver. Only about 10 min later, the velocity changed its polarity, thus "delaying" by ~ 10 min from the change of the IMF B_z polarity.

Figure 5.4b also shows the interplanetary electric field (IEF), pink diamonds. For B_z^+ conditions, it is negative. The IEF polarity changed at ~18:25UT, and this change is surely driven by the abrupt change of the IMF B_z magnitude. The IEF decrease started just prior to the RKN velocity increase. This is consistent with no significant variations of the solar wind velocity around this IMF transition and the solar wind velocity cannot be responsible for the RKN velocity jump at the transition time.

Red and blue dots in Figure 5.4b are the Kan-Lee reconnection electric field E_{KL} and reconnection electric field E_{RC} for positive B_z and negative B_z, respectively. The E_{KL} and E_{RC} values are often expressed not in mV/m (as the IEF) but normalized to the "radius of the Earth", as explained in Section 1.5, so that units are often kV/Re. What is shown in Figure 5.4b are these parameters in mV/m without considering the normalization coefficient, namely

$$E'_{KL} = IEF \cdot \sin^2\left(\frac{\theta}{2}\right), \tag{5.1}$$

$$E'_{RC} = IEF \cdot cos^4(\theta). \tag{5.2}$$

Equations (5.1) and (5.2) imply that units for E'_{KL} prime and E'_{RC} are mV/m. One clear conclusion regarding E_{KL} and E_{RC} can be made from Figure 5.4b, namely that the smooth enhancement in E_{RC} correlates with the smooth enhancement of the positive RKN LOS velocity. To quantify the relationship between the RKN median velocity and the IMF B_z and B_t we made a

scatter plot of the velocity versus these parameters (Figure 5.4c,d) and fit the data by a linear dependence of the form

$$y = a \cdot x + b. \quad (5.3)$$

Correlation coefficients between the velocity and B_z, B_t variations have also been computed. All relevant data are shown in Figure 5.4c,d. The Correlation coefficient is better for the B_z<0 plot. This plot also shows a larger coefficient a (~120 versus 78) implying that changes of the velocity are more sensitive to variations of B_z. We note that the linear fitting has been done without paying attention to the fact that the data show minor inconsistency with general expectation: namely, for negative (positive) B_z there are several points with "unwanted" positive (negative) velocity. These points occurred during periods of changing IMF polarity, and such dynamic situations require more detailed consideration. One factor is that the time delays between IMF changes and their effect arrival to the ionosphere cannot be estimated very precisely. It is a general opinion that an error can be as large as 10 min.

Figures 5.4e and 5.4f assess the relationship of the RKN velocity with E_{KL} and E_{RC}. Here we use original RKN measurements and show the LOS velocities as small dots, similar to the presentation in Figure 5.4a. Here we use the reconnection electric fields in units of kV per Earth radius Re (=6370 km) so that we can compare our data with those of Wilder et al. (2010).

In our analysis, we assess the scatter clouds by binning the velocity according E_{KL} and E_{RC} bins. The binned velocity is represented by open circles; there are only three points for B_z<0 while at least 10 for B_z>0. For the B_z<0 case, a clear increase of the velocity magnitude with E_{KL} is seen. We also characterized this increase by fitting the dots with linear dependence equation (5.3) and by computing the correlation coefficient. The correlation coefficient is high for B_z<0 case (minus sign is because an increase in E_{KL} gives a larger magnitude of negative velocities). For the B_z>0 case, increase of the velocity with E_{RC} is also seen but it is not as strong, the slope of the line is ~ 9 times smaller. The correlation coefficient here is small.

The data presented are consistent with the results presented in Chapter 4 in several ways. First of all, they support the notion that the meridional component of the polar cap plasma flow is sensitive to IMF B_z (B_t). Increase of the velocity magnitude is faster for B_z<0 as compared to the IMF B_z>0 case. The data, however, show that the velocity increase with B_z (B_t) for a case of B_z>0 is noticeable so that velocities as large as 200-300 m/s can happen even for moderate values of IMF B_z ~ 4 nT. The case presented gives us confidence that the data shows expected responses of

the flow velocity on changes of the magnetospheric driver's intensity, while hinting on the necessity to avoid periods with fast changing IMF.

5.4 RKN velocity and external drivers of the convection: Statistical analysis

We are now considering on extended RKN data set to assess the relationship of the near-noon meridional flows and two "drivers" of the high-latitude convection, E_{KL} and E_{RC}. We will then compare obtained results with the work by Wilder et al. (2010) in which similar dependence was sought by considering gridded SuperDARN velocity from multiple radar measurements. The data base considered here includes RKN observations in radar beams 6, 7, 8 and range gates 24, 25, 26 in 2007-2010. The beams/range gates selected corresponds roughly to the Resolute Bay observatory location (MLAT ~83^o) (Ghezelbash et al., 2013). Selection of this spot for the analysis is justified by future possibility to perform detailed analysis of the diurnal and seasonal variations of the convection velocity according to the RB ionosonde and compare with the SuperDARN data. We first built the data set for observations at near noon time (18-19 UT) for 2007-2010, i.e. all RKN velocities in the above beams and range gates along with information on the solar wind and IMF (with 1-min resolution) were placed into one data file that was then analyzed by applying appropriate conditions. First of all, we split the data available onto three seasons. Winter was represented by the data in November, December and January, equinox is represented by the data in February, March and April, August, September, and October, and summer is represented by the data in May, June and July. One would expect, on a basis of the number of months available for each season, that the data base for equinoxes would be the largest one but this is not the case. The RKN radar sees much more echoes during winter time (Ghezelbash et al., 2015) with the smallest amounts in summer time. We also note that the RKN radar is particularly good for winter observations at near noon hours (Ghezelbash et al., 2015); a similar type of analysis for the midnight sector would be interesting to perform but it would contain much fewer data points. Consistent with the goals of the study, the data sets built were split according to the IMF B_z, either $B_z<0$ or $B_z>0$.

Since the RKN velocity varies significantly, as we have shown in Section 5.3, some sort of averaging was needed. In our analysis, we binned the data according to the bins of either E_{KL} or E_{RC}. The bins were selected to match those of Wilder et al. (2010) so that our conclusions can

be compared with that study directly, i.e., the units for both E_{KL} and E_{RC} bins were kV per Earth radius. We note that because of variability in the observed velocities, the conclusions on the slopes of the fitted lines (to be discussed below) vary, depending on the binning criteria, but not very strongly to alter our conclusions in significant way.

5.5.1 Velocity versus E_{KL}, B_z<0 case

We first consider data for B_z<0. For this condition, especially for larger B_z magnitudes, the 2-D SuperDARN patterns consistently show antisunward flow (reflecting negative RKN velocities) and the effect of the velocity magnitude increase with $|B_z|$ is often easily recognizable by simply watching the SuperDARN convection map development over a day with strongly varying IMF B_z. Without going into detailed analysis, changes are seen as drastic variation in the color of the velocity vectors at near noon hours. Here we give a quantitative assessment of the effect.

Figure 5.5 shows RKN velocity medians (black circles) as a function of E_{KL}. Vertical bars by every circle are the standard deviations (plus/minus one) of the measured velocities within each bin (vertical bars), and the number of points available is also indicated. Panels (a), (b) and (c) represent data for winter, summer and equinox, respectively. The black circles in Figure 5.5a show a clear increase between E_{KL} of 0 and 17.5 kV/R_E. For larger E_{KL}, the median velocity first decreases but eventually increases to ~ 600 m/s, the same value as it was at E_{KL}=17.5 kV/ R_E. One way of assessing the trends in this plot is to say that there is a saturation of the dependence at large E_{KL} values.

To characterize the increasing part of the trends in Figure 5.5a we fit data for that part with linear dependence, according to equation (5.3). Parameters of this fit are shown in the top-left corner of Figure 5.5a. We note that the slope of the linear fit line is ~ 30 (m/s)/kV/R_E. This is the largest slope in all dependencies that we will infer in this Chapter.

Shown by diamonds in Figure 5.5a are the velocities reported by Wilder et al. (2010) for their data set and their method of analysis. We simply scaled the values from their paper. We can see that their velocities also show an increasing trend but the slope of the fit line, if it were derived, is much smaller than that of ours. On the other hand, if we made a linear fit to all available points in Figure 5.5a then this line would be much closer to the Wilder et al.'s (2010) data. We note that

the number of points for E_{KL}> 20 kV/ R_E drops significantly, and this was one of the reasons that we chose to linear fit the RKN data between 0 and 17.5 kV/ R_E. The other reason was that plots for other seasons (Figure 5.5b,c) did not have points at larger E_{KL}.

Comparing the plots of Figure 5.5a for winter data with the similar plots for summer and equinox data (Figure 5.5b,c), we can conclude that the effect of the velocity "saturation" at large E_{KL} is seen for all seasons but it is more difficult to recognize because the increasing parts of the trends are not as strong as for the winter data. The trend for the equinoctial data are closer to those of the winter data. The slope of the linear fit line is smallest for equinox, ~ 6 kV/R_E, i.e. 5 times smaller than for winter. We note that if the linear fitting is done only for E_{KL} in between 0 and 10 kV/R_E, the smallest slope would be for summer. We do not discuss these minor differences; one major seasonal difference is that the slope of the linear fit line, that we can term as "response of the velocity of E_{KL} change" is largest during winter time. We also note that our data for equinox and summer are much more consistent with the data of Wilder et al. (2010).

5.5.2 Velocity versus E_{RC}, B_z>0 case

We now consider data for B_z>0. For this condition, one cannot detect the expected effect of the velocity increase with B_z by simply watching the convection maps, as the 2-D convection maps are often very patchy. For quantitative assessment of the dependence, plots similar to those of the previous section have been produced, Figure 5.6. We note that the amount of data is comparable to what we had for B_z<0 case, which gives us confidence that the trends derived cannot be related to significantly larger or smaller data base. Seasonally, again winter has more measurements than the other two seasons.

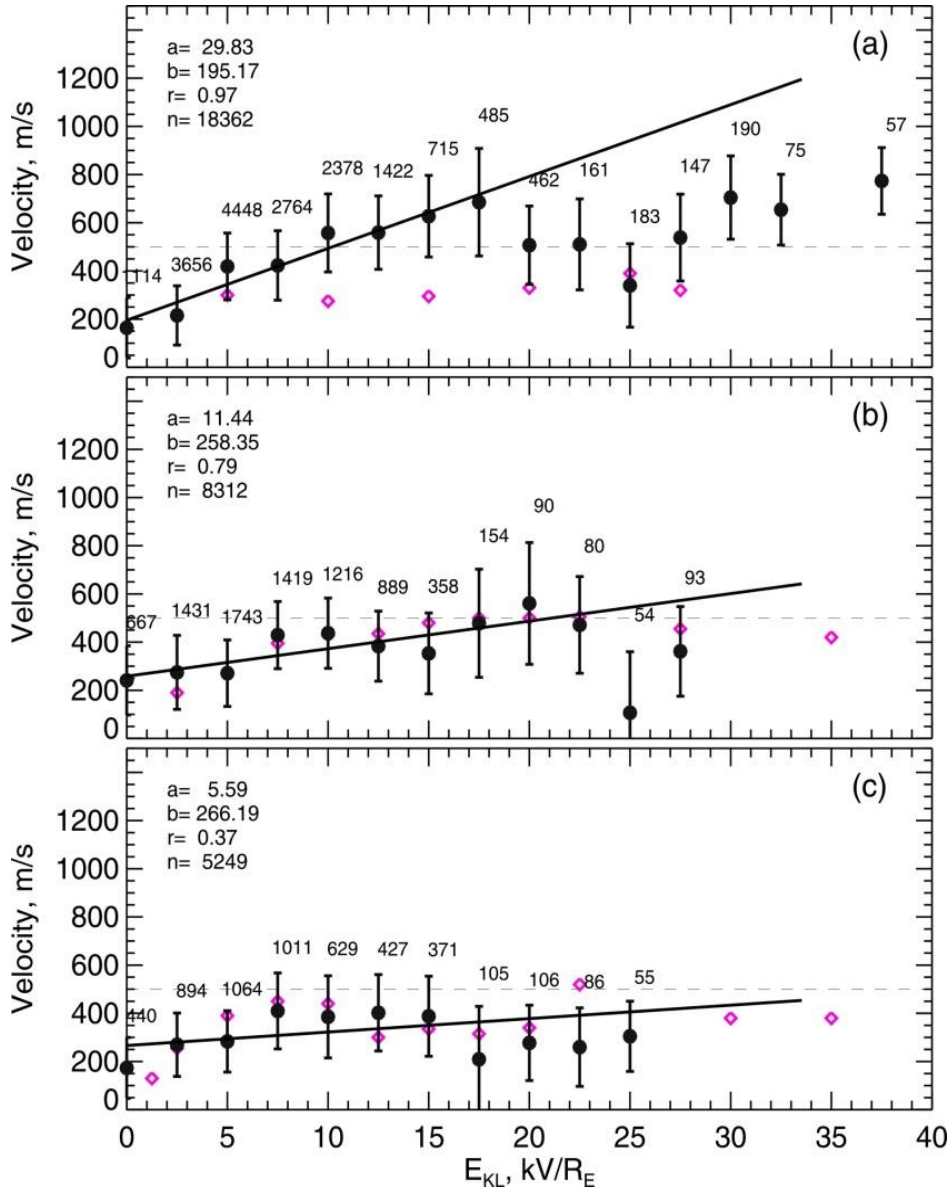

Figure 5.5: RKN median velocity (measured in beams 6, 7, 8 and gates 24, 25, 26, MLAT~83°) at near noon hour (18-19 UT) binned according to the reconnection electric field E_{KL}, black circles. Vertical bars around each circle are standard deviation of the velocity in each bin of E_{KL}. Data for B_z<0 were only considered. Numbers by each bin denote total number of points available in the bin. The velocity data were fit with a linear dependence (equation 5.3, line) in the E_{KL} range of 0-17.5 kV/R_E (range of the velocity increase) and the parameters of the fit and correlation coefficient are given in the top-left corner. Panels (a), (b) and (c) correspond to winter, summer and equinoctial periods, respectively. Diamonds are the data scaled from Wilder et al. (2010).

In terms of data trends, one difference with the B_z<0 data is that the "saturation" part of the dependence is not very obvious here. Again, the difference in our data and those of Wilder et al.

(2010) is only significant winter time where our data show smaller velocities. The linear fitting of the RKN medians has been done by considering E_{RC} range of 0 – 20 kV/ R_E. One obvious difference with the data of the B_z<0 case is that the slopes are not as strong and summer has the largest slope while winter has the smallest slope.

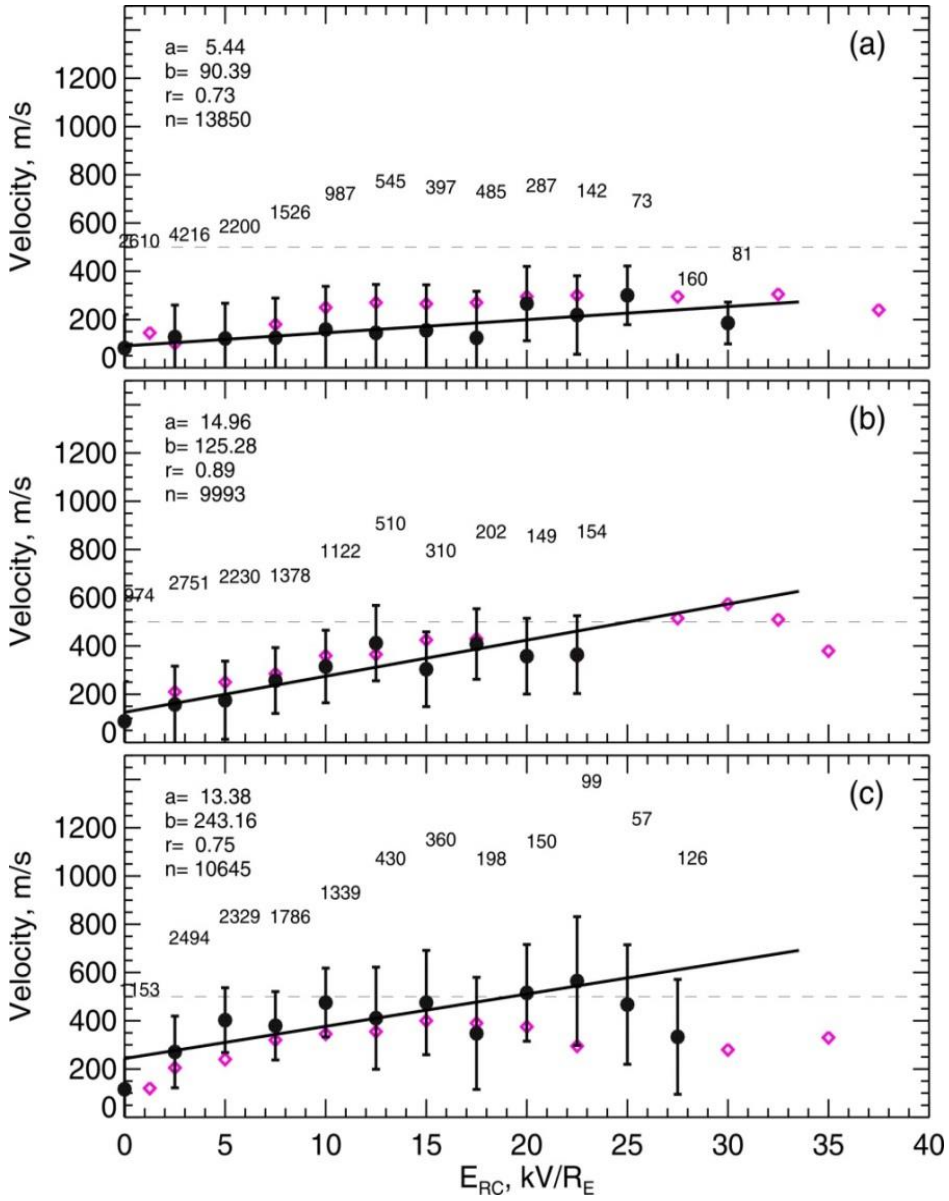

Figure 5.6: The same as Figure 5.5 but for B_z>0.

5.6 Discussion

The question on the response of the high-latitude convection to variations in the solar wind drivers is important for understanding how coupling between the solar wind and the Earth's magnetosphere works. Despite the significant SuperDARN data set accumulated so far and attempts to understand the relationship for individual events, the character of the relationship is still not well established.

In this Chapter, we investigated the dependence of the near-noon meridional flow velocity in the polar cap (at MLAT=82° -83°) upon the potential external drivers, the electrics field E_{KL} and E_{RC} characterizing for the flows for B_z<0 and B_z>0, respectively. Several obtained results are in agreement with the earlier work by Wilder et al. (2010). Here we first discuss these similarities.

We showed that the sunward flow at positive B_z, especially at large values, is a typical phenomenon as antisunward flows for negative B_z. This was shown by considering one specific event and by looking at velocity medians for the RKN and INV radars. Despite the general perception that for a B_z<0 situation more energy is supplied from the solar wind to the high-latitude ionosphere through front-side reconnection leading to higher activity, for example enhanced auroral electrojet, in terms of the convection velocity magnitude the difference with the B_z>0 situation is rather minor. Indeed, typical velocities in the polar cap are just ~ 100 m/s slower for B_z>0 as compared to B_z<0 cases (Figures 5.3, 5.4). For both cases there is an increase in the velocity magnitude with the intensification of either E_{KL} or E_{RC}, respective drivers of the convection for B_z<0 and B_z>0. We also noticed that the monthly distributions of all velocities for B_z>0 are very similar to the monthly distributions of the velocity for B_z<0.

Although the rate of the velocity increase depends on the B_z polarity and season, for summer and to a lesser extent for equinox, the rates were found to be comparable. Only winter data showed a large difference, of ~ 5 times, with faster rate of the velocity increase for B_z <0.

For B_z <0, the rate of the velocity increase is largest in winter time. This is in contrast with the largest rate of the velocity increase summer time for B_z >0. These results imply that typical polar cap velocities, when all possible IMFs are considered, should be somewhat smaller in summer time. The effect has been observed for many spring-equinox/summer months of RKN observations (Figure 3.8 of Chapter 3 and Koustov et al. (2013)). Wilder et al. (2010) suggested that weaker winter velocity increase is because of not efficient lobe reconnection during winter time when the lobs are tilted away from the direction toward the Sun. During winter, thus, not

much flow of sunward polarity is added to a regular antisunward flow due to front side reconnection. This seems to be a plausible explanation.

Our analysis of RKN and INV velocities revealed some differences with the results of Wilder et al. (2010). They are not so much in terms of the trends inferred, but mostly in terms of the velocity magnitudes for the winter data sets, for both B_z<0 and B_z>0 cases. In our data base the velocities were larger for B_z<0 but smaller for B_z>0.

The differences can originate from the fact that the data bases used were quite different. Wilder et al. (2010) considered data for 1998-2007, including the period of the solar cycle 23 maximum (2001-2002), a fairly active period. Our data are for 2007-2010, mostly for the solar cycle minimum period. We have shown (Figure 4.1) that IMF can assume much larger values for the solar cycle maximum period so that the Welder et al.'s (2010) data set had high velocities that we simply did not have because of weaker external drivers. For this reason, overall larger velocities for their data set in the case of B_z>0 (Figure 5.6) is not a surprise. Larger velocities for our data set for winter B_z<0 cases, Figure 5.5, seems to be inconsistent with the expectation, especially in view that B_z<0 flows can be very fast and large B_z^- values are more typical for the solar cycle maximum period.

Below we discuss some factors that could be involved in making this inconsistency. Before we proceed, however, we would like to mention one important circumstance: contrary to Wilder et al. (2010) we considered all the data available instead of attempting to isolate events with "stable" IMF. Our data of Figure 5.4 showed that for varying IMF, polarity of the flow velocity is not 100% consistent with polarity of the IMF. This affects our statistics and clearly more sophisticated analysis has to be performed. Since this work requires significant effort and is time consuming, we left this task for future work. We also would like to mention that in both approaches, median velocities have been considered although in our case, no "time filtering" has been applied (this is an important step in the gridding procedure, Section 2.5). This might be a factor for strongly varying IMF conditions, but the hope is always that these differences will be smoothed out in the statistics. Perhaps, this does not happen during winter time.

The fundamental difference between our velocity data set and the Wilder et al.'s (2010) data sets is that their velocities are for echoes detected through the 1½-hop propagation mode (far ranges of ~2000-3000 km) while most of the RKN data are collected through the ½-hop propagation mode. Although in a case of echo detection from the F region this should not bring

much of a statistical difference between the measurements, the fact of the matter is that some 1½-hop echoes can be detected from the E region as originally suggested by Milan et al. (1997). E region velocities can be much smaller than the F region velocities and the $\vec{E} \times \vec{B}$ drift (e.g., Koustov et al. 2005). If this effect of occasional echo detection from the E region affects significantly the radar velocities measured at far ranges, then larger RKN velocities for our data base (winter B_z<0) are understandable. Then only what needs to be explained is why the effect does not work for B_z>0 cases. We are unable to give reasonable explain at this time.

We see another possibility of interpreting the established differences. For B_z<0, generally strong precipitation in the auroral zone is expected, and only minor polar cap precipitations related to the cusp-cleft activity are possible. This creates more favorable propagation conditions for the polar cap radars and affects the auroral zone radars in a way that their beams might experience stronger lateral refraction (while propagating through irregular regions of enhanced electron density) and thus detect only a component of meridional flows. For B_z<0 one then can expect statistically smaller velocities for the Wilder et al.'s (2010) data base (stronger deviations effects) and this is exactly what was observed. In this explanation, for B_z>0 cases one would expect very little particle precipitation in the polar cap and decreased precipitation rates in the auroral zone. This makes radio wave propagation conditions less critical for measurements of the meridional flows with the auroral zone radars. In this case, the velocities should be about the same for the auroral zone and polar cap radars and the only difference can be expected for stronger drivers at the solar cycle maximum as discussed above.

5.7 Summary

Finally, summarizing the interesting results obtained in this Chapter, where showed that:

1) The plasma flow velocity measured by the polar cap radars, such as the RKN radar, at near noon hours is sensitive to quick changes in the IMF B_z component; for the IMF transition from a positive to a negative value by ~ 4 nT, the velocity (which is the meridional component of the transpolar flow) changed from sunward to antisunward within ~15 min from the time of the perturbation arrival to the ionosphere. In agreement with previous publications, there was a ~1-2 min delay in

the “immediate” velocity response time but the velocity change was not as expected - instead of a positive velocity decrease, the velocity suddenly increased by ~ 100 m/s and only ~5 min later started to decrease and eventually became negative.

2) By averaging data over about 3 years of observations, the meridional component of the transpolar velocity, monitored by the RKN radar at near noon hours, increases with intensification of the external drivers, E_{KL} for $B_z<0$ and E_{RC} for $B_z>0$. For E_{KL} and E_{RC} > 15-20 kV/ R_E (2.5-3 mV/m), the rates of the increase slow down and eventually the increase stops (saturation effect). The velocity increase on the growing part of the dependence can be approximated by a linear line. Obtained slopes of the regression line were found to be comparable to those given by Wilder et al. (2010) who considered gridded velocity of all SuperDARN radars. The increase was fastest winter time for $B_z<0$ and summer time for $B_z>0$.

CHAPTER 6

SUMMARY AND PLANS FOR FUTURE RESEARCH

This thesis was focused on assessing convection patterns in the high-latitude ionosphere and their dependence upon external factors related to the solar wind and IMF. First of all, we inferred typical shapes of the patterns for positive and negative IMF B_z by considering highly-averaged (monthly) data from all SuperDARN HF radar measurements (in the northern hemisphere). The data base consisted of 11 consecutive years of observations. We selected several parameters characterizing the patterns and investigated variations of these parameters with time of the day, season and with an increase of the solar activity. We then attempted to understand how the patterns (and their parameters) change with an increase of the IMF B_z and B_t. Finally, we investigated the response of the high-latitude dayside plasma flows to changes in the rate of the IMF merging. For this task, we considered data from just one radar, at Rankin Inlet, monitoring ionospheric flows in the polar cap. Here, the analysis has been done on a time scale of one minute, the resolution of the radar and solar wind/IMF data. Below we summarize our major findings.

6.1 Monthly-averaged convection patterns without considering IMF

The inferred patterns consisted, on average, of two cells symmetric with respect to the noon-midnight meridian except that the dayside throat of the patterns was consistently shifted to 10-11 MLT (prior to the magnetic noon) at the auroral oval latitudes. At higher latitudes, in the polar cap, the throat was located close to the magnetic noon. This last result has been anticipated because the throat location is controlled by the IMF B_y component, and averaging over long periods should lead to the noon location. Contrary to de la Beujardiere et al. (1991), who reported seasonal trend in the throat location, our data did not show it, independent on the phase of the solar cycle.

We investigated the magnetic latitude location of the convection reversal boundary (CRB). We showed that the MLAT of the CRB location depends on MLT, season and solar cycle. Typically, it is at ~77^o. The CRB on the dusk side showed seasonal variation, especially during

high solar activity when it reached highest MLATs during summer time. We also confirmed that the CRB shifts to higher magnetic latitudes (by ~1^o) during the solar minimum. An important conclusion of our analysis is that many features of the CRB location are in agreement with the ones reported by Bristow and Spaleta (2013) who used SuperDARN data but used completely different approach.

Finally, we studied the magnitude of the flows. The typical speeds were found to be ~400 m/s. We demonstrated that in the midnight and noon sectors, the flows are faster in summer during high solar activity. For low solar activity, no clear seasonal trend was found. Over a solar cycle, the velocity of plasma flow in the noon and dusk sectors is faster during high solar activity. In an alternative approach to the solar cycle effect in the speed of the plasma flow, we considered LOS velocity data of just one radar, the RKN radar. We demonstrated that the nighttime plasma velocity increases toward the solar cycle maximum for observations at MLAT ~ 80°-82°.

6.2 Monthly average convection patterns considering IMF

By considering monthly-averaged SuperDARN data for 1995-2011, binned according to the IMF B_z and B_t, we confirmed that the patterns become four-celled or distorted two-celled for the IMF B_z>0. All the data showed that the plasma flow velocity increases roughly linearly with B_t. Typical rates of the increase were found to be 30-40 m/s/nT for B_z<0 and only 1-10 m/s/nT for B_z>0. For B_z<0, the effect of the velocity increase was found to be stronger summer time, on the dayside and for high solar activity. This is in contrast with very weak tendencies for a case of B_z>0.

6.3 Meridional dayside flows and external drivers E_{KL} and E_{RC}

By considering dayside meridional flow magnitude (LOS velocity measured by the RKN radar) as a function of two drivers, E_{KL} for B_z<0 and E_{RC} for B_z>0, we demonstrated that the velocity increases with intensification of these parameters characterizing the rate of merging processes at the magnetosphere front edge and its lobes, respectively. The rate of the increase was found to slow down for strong magnitudes of the drivers (demonstrating the “saturation” effect). The rate of the velocity increase was described by a linear function. The slope of the fit was largest

during winter for $B_z<0$ (E_{KL}) and during summer for $B_z>0$ (E_{RC}).Our findings are in good agreement with the observations reported by Wilder et al. (2010) who considered highly averaged (gridded) SuperDARN velocities.

6.4 Suggestions for future research

Now a focus on some interesting and new, to the best of our knowledge, results reported in this Thesis and suggestions possible ways to expand the work to improve our knowledge on the plasma flows at high latitudes and their magnetospheric drivers.

6.4.1 Averaged convection patterns

One interesting result reported in this Thesis is an increase in the typical velocity of plasma flow along the noon-midnight meridian toward solar cycle maximum. The effect was demonstrated in two ways: by looking at the velocity magnitudes inferred from all SuperDARN data (SCHA analysis of grid velocities, Figure 3.7) and by looking at the LOS velocity data of just one (RKN) radar monitoring echoes from the polar cap, Figure 3.8. The plasma velocity increase is expected because magnetospheric drivers of the ionospheric convection are generally stronger during the years of high solar activity. Further investigation of this effect would be interesting because other phenomena in the near-Earth space also show solar cycle variations, for example the geomagnetic activity increases toward the solar cycle maximum (e.g., Richardson et al., 2002). Magnetometers are sensitive to the ionospheric current intensity (at the E region height) controlled by the electric field and conductance in the ionosphere. There is no doubt that the magnetic activity increases during years of the solar activity maximum and is related to strong enhancement in the ionospheric conductance (due to stronger particle precipitations), but the electric field increase might also contribute to the phenomenon, and it is interesting to know to what extent. One of the ways to obtain more information on the issue is to investigate data of the Saskatoon SuperDARN radar which has been collected data since 1994. It would be interesting to consider separately latitudes of the auroral oval (½-hop echo detection) and polar cap (1½-hop echo detection). This is because our plots show some preferential latitudes for largest velocities, Figure 3.7a,b.

The other, rather surprising, effect in inferred convection patterns is the strong asymmetry of the velocity magnitude along the dawn-dusk meridian, Figure 3.7. Flows at the auroral zone latitudes were found to be faster during dusk (and afternoon) hours while flows in the polar cap faster during morning (and pre-noon) hours. In this respect, it would be interesting to consider two radars monitoring echoes roughly along the geomagnetic parallels because in the dusk/dawn sectors the flows are predominantly zonal. Two radars that are good candidates for such a study are the Stokkseyri radar in the auroral zone and the Clyde River radar in the polar cap.

Although not stressed in the text, the diurnal variations of the plasma velocity at latitudes of the RB is inconsist with the diurnal variations of the plasma velocity inferred from CADI ionosonde data reported by Ghezelbash et al. (2015). Although both instruments are believed to be reliable for convection monitoring, further work is needed to understand why there are some discrepancies. With the recent introduction of the CLY radar, achieving more significant data base of full SuperDARN vectors over RB (through merging RKN, INV and CLY data), as compared to the study by Mori et al. (2012) is very realistic. This large data base would allow investigating separately winter and summer data as well. Independently, a more systematic study of the trends in the RB CADI ionosonde data would be useful. One of the issues with the CADI velocity data is their strong variability, from one measurement to another.

6.4.2 Averaged convection patterns with IMF consideration

We showed in both Chapters 3 and 4 that the velocity of the polar cap flow is larger during summer time. The effect is mostly due to a summer increase in the zonal component of the flow, Figure 4.2. As we already mentioned, the effect contradicts to the conclusions of the computer models. It is highly desirable to understand whether the discovered effect is real. The reason for some skepticism is that the SuperDARN data base is lacking measurements for the flows along magnetic parallels because FoVs of almost all the radars are oriented toward the magnetic Pole, see Figure 2.2. Only recently, the CLY radar started collection of the velocity data along geomagnetic parallels. In this view, work needs to be done in correlating velocity measurements of the CLY radar and the IMF conditions. Such an effort has been started, the author has participated in it, but the results have not been finalized.

The other interesting result of the convection maps sorted out according to the B_t conditions is that the rate of plasma velocity increase with B_t is larger at near noon hours and during years of high solar activity. It is important to understand why this happens. In cooperation with US scientists, possibility exists to run large-scale MHD models to simulate various conditions in the IMF and magnetosphere and to investigate the role of the conductance and dipole tilt and then assess reasons for preferential conditions in terms of physics involved as the code allows one to look at variations of the field-aligned current intensity, electric field, plasma density, etc. Currently, we are not aware of any computer modeling work that would address response of the convection on external drivers at various latitudes during different phases of a solar cycle.

6.4.3 Polar cap flow velocity and magnetospheric drivers, point-by-point comparison

One clear weakness of the performed analysis is that all the RKN measurements at near noon hours were considered, including periods of the IMF transitions. It is highly desirable to isolate events with relatively stable IMF. Additional work that can be done in this analysis is regular checking the direction of the near noon flows by looking at the 2-min SuperDARN convection maps. This is a tedious work but the good quality analysis, even with a limited data set (contrary to our multi-year analysis), would allow making well substantiated conclusions. In the past, producing standard SuperDARN convection maps on a 2-min basis has been problematic but there are plans to produce all of them and store at the University of Saskatchewan in near future.

With the point-by-point comparison approach, an interesting activity could be work with CLY radar data. As we have already mentioned, this radar measures the velocity of the zonal plasma motions at the polar cap latitudes. Because of this, role of the IMF B_y component in establishing plasma flows (Svalgaard-Mansurov effect) can be investigated in detail while considering true zonal velocities of plasma drift and not the magnetic effect of the electrojet.

References

Axford, W. I., and C. O. Hines (1961), A unifying theory of high-latitude geophysical phenomena and geomagnetic storms, *Can. J. Phys., 39*, 1433-1464, 1961.

Benkevich, L. V. (2005), Effects of ionospheric conductance in high latitude phenomena, Ph.D. Thesis, Univ. of Saskatchewan, Saskatoon, Canada.

Blanchard, G. T., S. Sundeen, and K. B. Baker (2009), Probabilistic identification of high-frequency radar backscatter from the ground and ionosphere based on spectral characteristics, *Radio Sci*., *44*, RS5012, doi:10.1029/2009RS004141.

Bristow, W. A., and J. Spaleta (2013), An investigation of the characteristics of the convection reversal boundary under southward interplanetary magnetic field, *J. Geophys. Res., 118*, 6338-6351.

Buchau, J., B. W. Reinisch, D. N. Anderson, E. D. Weber, and C. Dozois (1988), Polar cap plasma convection measurements and their relevance to the modeling of the high-latitude ionosphere, *Radio Science, 23*, 521-536.

Burch, J. L. (1972), Precipitation of low-energy electrons at high latitudes: Effect of interplanetary magnetic field and dipole tilt angle, *J. Geophys. Res.,* 77, 6696-6707.

Campbell, W. H. (1982), Annual semiannual changes of the quiet daily variations (Sq) in the geomagnetic filed at North American locations, *J. Geophys. Res., 87*, 785-796.

Chisham, G., M. Lester, S. E. Milan, et al. (2007), A decade of the Super Dual Auroral Radar Network (SuperDARN): Scientific achievements, new techniques and future directions, *Surv. Geophys., 28*, 33–109, doi:10.1007/s10712-007-9017-8.

Cnossen, I., M. Wiltberger, and J. E. Ouellette (2012), The effects of seasonal and diurnal variations in the Earth's magnetic dipole orientation on solar wind–magnetosphere-ionosphere coupling, *J. Geophys. Res., 117*, A11211, doi:10.1029/2012JA017825.

Cousins, E. D. P., and S. G. Shepherd (2010), A dynamical model of high-latitude convection derived from SuperDARN plasma drift measurements, *J. Geophys. Res., 115*, doi:10.1029/2010JA016017.

Crooker, N. U. and F. J. Rich (1993), Lobe cell convection as a summer phenomenon, *J. Geophys. Res., 98*, 13,403–13,407.

de la Beaujardiere, O., D. Alcayde, J. Fontanari, and C. Leger (1991), Seasonal dependence of high-latitude electric fields, *J. Geophys. Res., 96*, 5723-5735.

Dungey, J. W. (1961), Interplanetary magnetic field and auroral zones, *Phys. Res. Lett., 6*, 47–48.

Drayton, R., 2006, Study of SAPS-like flows withy the King Salmon SuperDARN radar, MSc Thesis, U of Saskatchewan, Saskatoon, Canada.

Fejer, B. G., and M. C. Kelley, Ionospheric irregularities, Review of Geophysics, 18, 401-454, 1980.

Fiori, R. A. D., A. V. Koustov, D. Boteler, and R. A. Makarevich (2009), PCN magnetic index and average convection velocity in the polar cap inferred from SuperDARN radar measurements, *J. Geophys. Res.*, *114*, A07225, doi:10.1029/2008JA013964.

Fiori, R. A. D., D. H. Boteler, A. V. Koustov, G. V. Haines, and J. M. Ruohoniemi (2010), Spherical cap harmonic analysis of Super Dual Auroral Radar Network (SuperDARN) observations for generating maps of ionospheric convection, *J. Geophys. Res.*, *115*, A07307, doi:10.1029/2009JA015055.

Fiori, R. A. D., D. H. Boteler, and A. V. Koustov (2012), Response of ionospheric convection to sharp southward IMF turnings inferred from magnetometer and radar data, *J. Geophys. Res.*, *117*, A09302, doi:10.1029/2012JA017755.

Fiori, R. A. D., D. H. Boteler, A. V. Koustov, D. Knudsen, and J. K. Burchill (2014), Investigation of localized 2D convection mapping based on artificially generated Swarm ion drift data, *J. Atmos. Solar-Terr. Phys.*, *114*, 30–41.

Freeman, M. P. (2003), A unified model of the response of ionospheric convection to changes in the interplanetary magnetic field, *J. Geophys. Res.*, *108* (A1), doi:10.1029/2002JA009385.

Friis-Christensen, E., Y. Kamide, A. D. Richmond, and S. Matsushita (1985), Interplanetary magnetic field control of high-latitude electric field and currents determined from Greenland magnetometer data, *J. Geophys. Res., 90*, 1325-1338.

Förster, M., G. Paschmann, S. E. Haaland, J. M. Quinn, R. B. Torbert, H. Vaith, and C. A. Kletzing (2007), High-latitude plasma convection from Cluster EDI: variances and solar wind correlations, *Ann. Geophys., 25*, 1691–1707.

Ghezelbash, M. (2013), Occurrence and causes of *F*-region echoes for the Canadian PolarDARN/SuperDARN radars, M.Sc. thesis, University of Saskatchewan, Saskatoon, Canada, available at: http://hdl.handle.net/10388/ETD-2013-03-949.

Ghezelbash, M., A. V. Koustov, D. R. Themens, and P. T. Jayachandran (2014), Seasonal and diurnal variations of PolarDARN F region echo occurrence in the polar cap and their causes, *J. Geophys. Res. Space Physics, 119*, doi:10.1002/2014JA020726.

Ghezelbash, M., R. A. D. Fiori, and A. V. Koustov (2014), Variations in the occurrence of SuperDARN *F* region echoes, *Ann. Geophys.*, *32*, 147–156, 2014, www.ann-geophys.net/32/147/2014/, doi:10.5194/angeo-32-147-2014.

Greenwald, R. A., K. B. Baker, J. R. Dudeney, M. Pinnock, T. B. Jones, E. C. Thomas, J.-P. Villain, J.-C. Cerisier, C. Senior, C. Hanuise, R. D. Hunsuker, G. Sofko, J. Koehler, E. Nielsen, R. Pellinen, A. D. M. Walker, N. Sato, and H. Yamagishi (1995), DARN/SuperDARN: A global view of the dynamics of high-latitude convection, *Space Sci. Rev., 71*, 761-796.

Haaland, S., G. Paschmann, M. Förster, J. M. Quinn, R. B. Torbert, C. E. McIlwain, H. Vaith, P. A. Puhl-Quinn, and C. A. Kletzing (2007), High-latitude plasma convection from Cluster EDI measurements: method and IMF-dependence, *Ann. Geophys., 25*, 239–253.

Haines. G. (1985), Spherical cap harmonic analysis, *J. Geophys. Res.*, *90* (B3), 2583–2591.

Hairston, M. R., and R. A. Heelis (1990), Model of the high-latitude ionospheric convection pattern during southward interplanetary magnetic field using DE 2 data, *J. Geophys. Res.*, *95*, 2333–2343.

Hairston, M. R., and R. A. Heelis (1995), Response time of the polar ionospheric convection pattern to changes in the north-south direction of the IMF, *Geophys. Res. Lett.*, *22* (5), 631–634.

Hargreaves, J. K., The Solar-Terrestrial Environment, Cambridge University Press, Cambridge UK, 1992.

Heelis, R. A., P. H. Reiff, J. D. Winningham, and W. B. Hanson (1986), Ionospheric convection signatures observed by De 2 during northward interplanetary magnetic field, *J. Geophys. Res.*, *91*, 5817-5930.

Heppner, J. P., and N. C. Maynard (1987), Empirical high-latitude electric field models, *J. Geophys. Res.*, 92, (A5), 4467-4489.

Huber, M. (1999), HF radar echo statistics and spectral studies using SuperDARN, M.Sc. Thesis, Univ. of Saskatchewan, Saskatoon, Canada.

Iijima, T., and T. A. Potemra (1976), The amplitude distribution of field-aligned currents at northern high latitudes observed by Triad, *J. Geophys. Res., 81*, 2165-2174.

Juusola, L., et al. (2014), Statistical comparison of seasonal variations in the GUMICS-4 global MHD model ionosphere and measurements, *Space Weather*, *12*, 582–600, doi:10.1002/2014SW001082.

Kan, J. R., and L. C. Lee (1979), Energy coupling function and solar wind magnetosphere dynamo, *Geophys. Res. Lett., 6*(7), 577–580.

Kelley, M. C. (1989), The Earth's ionosphere, Academic Press, San Diego, CA, 1989.

Kivelson, M., and C.T. Russel, Editors (1995), Introduction to space physics, Cambridge University Press,

Koustov, A. V., D. W. Danskin, R. A. Makarevitch, and J. D. Gorin (2005), On the relationship between the velocity of E-region HF echoes and E×B plasma drift, *Ann. Geophys.*, *23* (2), 1–9.

Koustov, A. V., J. W. MacDougall, and G. E. Kadochnikov (2007), A comparison of CADI-inferred F region plasma convection and DMSP ion drift above Resolute Bay, *Radio Sci.*, *42*, RS6012, doi:10.1029/2007RS003706.

Koustov, A. V., J.-P. St-Maurice, G. J. Sofko, D. Andre, J. W. MacDougall, M. R. Hairston, R. A. Fiori, and G. E. Kadochnikov (2009a), Three-way validation of the Rankin Inlet PolarDARN radar velocity measurements, *Radio Sci.*, *44*, RS4003, doi:10.1029/2008RS004045.

Koustov, A. V., G. Y. Khachikjan, R. A. Makarevich, and C. Bryant (2009b), On the SuperDARN cross polar cap potential saturation effect, *Ann. Geophys.*, *27*, 3755–3764.

Koustov, A. V., K. Colville, R. A. D. Fiori, M. Ghezelbash (2013), Assessing Doppler velocities of Rankin inlet F-region echoes, *J. Adv. Polar Science*, 24, 50-59.

Koustov, A. V., R.A.D. Fiori, and Z. Abooali zadeh (2013), Averaged plasma flows in the polar cap inferred from SuperDARN data, Program and Abstracts of SuperDARN-2013 workshop, 26-31 May 2013, Moose Jaw, Saskatchewan, Canada, p.22-23.

Lu, G., T. E. Holzer, D. Lummerzheim, J. M. Ruohoniemi, P. Stauning, O. Troshichev, P. T. Newell, M. Britnacher, and G. Parks (2002), Ionospheric response to the interplanetary magnetic field southward turning: Fast onset and slow reconfiguration, *J. Geophys. Res.*, *107* (A8), doi:10.1029/2001JA000324.

Lukianova, R., O. Troshichev, and G. Lu (2002), The polar cap magnetic activity indices in the southern (PCS) and northern (PCN) polar caps: Consistency and discrepancy, *Geophys. Res. Lett.*, *29*, 1879, doi:10.1029/2002GL015179.

Maezawa, K. (1976), magnetospheric convection induced by the positive and negative Z component of the IMF: Quantitative analysis using polar cap magnetic records, *J. Geophys. Res.*, *81*, 2289-2303.

Milan, S. E., T. K. Yeoman, M. Lester, E. C. Thomas, and T. B. Jones (1997), Initial backscatter occurrence statistics from the CUTLASS radars, *Ann. Geophys.*, *15*, 703–718.

Mori, D., A. V. Koustov, P. T. Jayachandran, and N. Nishitani (2012), Resolute Bay CADI ionosonde drifts, PolarDARN HF velocities, and cross polar cap potential, *Radio Sci.*, *47*, RS3003, doi:10.1029/2011RS004947.

Mori, D. and A. V. Koustov (2013), SuperDARN cross polar cap potential dependence on the solar wind conditions and comparisons with models, *Adv. Space Res.*, 52, 1155-1167.

Newell, P. T., and C. I. Meng (1989), Dipole tilt angle effects on the latitude of the cusp and cleft/LLBL, *J. Geophys. Res.*, *94*, 6949-6953.

Newell, P. T., T. Sotirelis, K. Liou, C.-I. Meng, and F. J. Rich (2007), A nearly universal solar wind-magnetosphere coupling function inferred from 10 magnetospheric state variables, *J. Geophys. Res., 112,* A01206, doi:10.1029/2006JA012015.

Nishitani, N., T. Ogawa, N. Sato, H. Yamagishi, M. Pinnock, J.-P. Villain, G. Sofko, and O. Troshichev (2002), A study of the dusk convection cell's response to an IMF southward turning, *J. Geophys. Res.*, *107* (A3), doi:10.1029/2001JA900095.

Papitashvili, V., and F. J. Rich (2002), High-latitude ionospheric convection models derived from Defense Meteorological Satellite Program ion drift observations and parameterized by the interplanetary magnetic field strength and direction, *J. Geophys. Res., 107*, 1198, doi:10.1029/2001JA000264.

Pettigrew, E. D., S. G. Shepherd, and J. M. Ruohoniemi (2010), Climatological patterns of high-latitude convection in the northern and southern hemispheres: Dipole tilt dependencies and interhemispheric comparisons, *J. Geophys. Res., 115*, A07305, doi:10.1029/2009JA014956.

Prikryl, P., P. T. Jayachandran, S. C. Mushini, D. Pokhotelov, J. W. MacDougall, E. Donovan, E. Spanswick, and J.-P. St.-Maurice (2005), GPS TEC, scintillation and cycle slips observed at high latitudes during solar minimum, *Ann. Geophys., 23*, 3451–3455.

Prikryl, P., P. T. Jayachandran, S. C. Mushini, and R. Chadwick (2011), Climatology of GPS phase scintillation and HF radar backscatter for the high-latitude ionosphere under solar minimum conditions, *Ann. Geophys., 29*, 377-392.

Rash, J. P. S., A. S. Rodger, and M. Pinnock (1999), HF radar observations of the high-latitude ionospheric convection pattern in the morning sector for northward IMF and motion of the convection reversal boundary, *J. Geophys. Res., 104*, 14857-14866.

Ribeiro, A. J., J. M. Ruohoniemi, J. B. H. Baker, L. B. N. Clausen, S. de Larquier, and R. A. Greenwald (2011), A new approach for identifying ionospheric backscatter in midlatitude SuperDARN HF radar observations, *Radio Sci., 46*, RS4011, doi:10.1029/2011RS004676.

Ribeiro, A. J., J. M. Ruohoniemi, P. V. Ponomarenko, L. B. N. Clausen, J. B. H. Baker, R. A. Greenwald, K. Oksavik, and S. de Larquier (2013), A comparison of SuperDARN ACF fitting methods, *Radio Sci., 48*, doi:10.1002/rds.20031.

Reiff, P. H., and J. L. Burch (1985), IMF By-dependent plasma flow and Birkeland currents in the dayside magnetosphere, 2, A global model for northward and southward IMF, *J. Geophys. Res., 90*, 1595-1609.

Reiff, P. H., and J. G. Luhmann (1986), Solar wind control of the polar-cap voltage, in *Solar wind-magnetosphere coupling*, edited by Y. Kamide and J. Slavin, pp. 453–476, Terra Sci., Tokyo.

Rich, F. J., and M. Hairston (1994), Large-scale convection pattern observed by DMSP, *J. Geophys. Res.*, 99, (A3), 3827-3844.

Richardson, I. G., H. V. Cane, E. W. Cliver (2002), Sources of geomagnetic activity during nearly three solar cycles (1972–2000), *J. Geophys. Res., 107*, 1187, doi:10.1029/2001JA000504.

Ridley, A. J., and C. R. Clauer (1996), Characterization of the dynamic variations of the dayside high-latitude ionospheric convection reversal boundary and relationship to interplanetary magnetic field orientation, *J. Geophys. Res., 101*, 10919-10938.

Ridley, A. J., G. Lu, C. R. Clauer, and V. O. Papitashvili (1998), A statistical study of the ionospheric convection response to changing interplanetary magnetic field conditions using the assimilative mapping of ionospheric electrodynamics technique, *J. Geophys. Res.*, *103* (A3), 4023–4039.

Ruohoniemi, J. M., and K. B. Baker (1998), Large-scale imaging of high-latitude convection with SuperDual Auroral Radar network HF radar observation, *J. Geophys. Res.*, 103, (A9), 20797-20811.

Ruohoniemi, J. M., and R. A. Greenwald (1996), Statistical patterns of high-latitude convection obtained from Goose Bay HF radar observations, *J. Geophys. Res., 101* (A10), 22,743–21,763.

Ruohoniemi, J. M., and R. A. Greenwald (2005), Dependencies of high-latitude plasma convection: Consideration of interplanetary magnetic field, seasonal, and universal time factors in statistical patterns, *J. Geophys. Res., 110*, A09204, doi:10.1029/2004JA010815.

Ruohoniemi, J. M., and R. A. Greenwald (1998), The response of high-latitude convection to a sudden southward IMF turning, *Geophys. Res. Lett.*, *25*, 2913–2916.

Scherliess, L., B. G. Fejer, J. Holt, L. Goncharenko, C. Amory-Mazaudiear, and M. J. Buonsanto (2001), Radar studies of midlatitude ionospheric plasma drifts, *J. Geophys. Res.*, *106*, 1771-1783.

Shepherd, S. G., R. A. Greenwald, and J. M. Ruohoniemi (1999), A possible explanation for rapid, large-scale ionospheric responses to southward turnings of the IMF, *Geophys. Res. Lett.*, *26* (20), 3197–3200.

Shepherd, S., R. Greenwald, and J. Ruohoniemi (2002), Cross polar cap potentials measured with super dual auroral radar network during quasi-steady solar wind and interplanetary magnetic field conditions, *J. Geophys. Res., 107*, 1094, doi:10.1029/2001JA000152.

Shepherd, S. G., J. M. Ruohoniemi, and R. A. Greenwald (2003), Testing the Hill model of transpolar potential with Super Dual Auroral Radar Network observations, *Geophys. Res. Lett.*, *30*, 1002, doi:10.1029/2002GL015426.

Smith, P. R., P. L. Dyson, D. P. Monsleesan, and R. Morris (1998), Ionospheric convection at Casey, a southern polar cap station, *J. Geophys. Res.*, *103*, 2209-2218.

Sonnerup, B. U. O. (1979), Magnetopause reconnection rate, *J. Geophys. Res., 79*, 1546-1549.

Troshichev, O. A., R. Y. Lukianova, V. O. Papitashvili, F. J. Rich, and O. Rasmussen (2000), Polar cap index (pc) as a proxy for ionospheric electric field in the near-pole region, *Geophys. Res. Lett.*, *27*, 38009-3812.

Troshichev, O., A. Janzhura, and P. Stauning (2006), Unified PCN and PCS indices: Method of calculation, physical sense, and dependence on the IMF azimuthal and northward components, *J. Geophys. Res.*, *111*, A05208, doi:10.1029/2005JA011402.

Weimer, D. R. (1996), A flexible, IMF dependent model of high-latitude electric potentials having "space weather" applications, *Geophys. Res. Lett.*, *23*, 2549-2552.

Weimer, D. R., D. M. Ober, N. C. Maynard, M. R. Collier, D. J. McComas, N. F. Ness, C. W. Smith, and J. Watermann (2003), Predicting interplanetary magnetic field propagation delay times using the minimum variance technique, *J. Geophys. Res.*, *108*, doi:10.1029/2002JA009405.

Wilder, F. D., C. R. Clauer, and J. B. H. Baker (2008), Reverse convection potential saturation during northward IMF, *Geophys. Res. Lett.*, *35*, L12103, doi:10.1029/2008GL034040.

Wilder, F. D., C. R. Clauer, and J. B. H. Baker (2009), Reverse convection potential saturation during northward IMF under various driving conditions, *J. Geophys. Res.*, *114*, A08209, doi:10.1029/2009JA014266.

Wilder, F. D., C. R. Clauer, and J. B. H. Baker (2010), Polar cap electric field saturation during interplanetary magnetic field Bz north and south conditions, *J. Geophys. Res.*, *115*, A10230, doi:10.1029, JA015487.

Yu, Y., and A. J. Ridley (2009), Response of the magnetosphere-ionosphere system to a sudden southward turning of interplanetary magnetic field, *J. Geophys. Res.*, *114*, A03216, 10.1029/2008JA013292.